

UC Santa Cruz

UC Santa Cruz Electronic Theses and Dissertations

Title

Novel Approaches to Soft Robot Actuation and Sensing; A Bioinspired Soft-rigid Hybrid Finger with Variable Stiffness Modules

Permalink

<https://escholarship.org/uc/item/81j4d3tz>

Author

Lin, Keng-Yu

Publication Date

2022

Supplemental Material

<https://escholarship.org/uc/item/81j4d3tz#supplemental>

Peer reviewed|Thesis/dissertation

UNIVERSITY OF CALIFORNIA
SANTA CRUZ

**NOVEL APPROACHES TO SOFT ROBOT ACTUATION AND SENSING;
A BIOINSPIRED SOFT-RIGID HYBRID FINGER WITH VARIABLE
STIFFNESS MODULES**

A dissertation submitted in partial satisfaction
of the requirements for the degree of

DOCTOR OF PHILOSOPHY

in

COMPUTER ENGINEERING

by

Keng-Yu Lin

June 2022

The Dissertation of Keng-Yu Lin is
approved:

Professor Michael Wehner, Chair

Professor Gabriel H. Elkaim

Roy Kornbluh

Peter Biehl
Vice Provost and Dean of Graduate Studies

Copyright © by

Keng-Yu Lin

2022

Table of Contents

List of Figures	vi
List of Tables	xi
List of Notations	xii
Table of Acronyms	xv
Abstract	xvi
Acknowledgments	xix
1. Introduction	1
1.1 Motivation	1
1.2 Theoretical Framework	4
1.3 Thesis Contributions	6
1.4 Thesis Outline	9
2. Background and Literature Review	12
2.1 Soft Robot Drive Method	12
2.2 Soft Robotic Sensor	15
2.3 Variable Stiffness Structure	16
2.3.1 Three Types of Jamming	18
3. Soft Robotic Sensing, Proprioception via Cable and Microfluidic Transmission	21
3.1 Introduction	21
3.2 Method	29
3.2.1 Design and Fabrication	37
3.2.2 Vision Algorithms	40
3.2.3 Sensor Characterization	41
3.3 Results	42
3.3.1 Fiber-Based Deformation Sensor	44
3.3.2 Source of Hysteresis	45
3.3.3 Microfluidic Pressure Sensors	46

3.4	Discussion	47
4.	Bioinspired Soft Finger with Multi-Curvature Locking Modules	52
4.1	Introduction	52
4.2	Method	61
4.2.1	Locking Mechanism Design	65
4.2.2	Locking Mechanism Force Analysis	68
4.2.3	Pneumatic Actuator and Tendon-driven Actuator	72
4.2.4	Kinematic Analysis	75
4.2.5	Fingers in Multiple Grasp Modes	80
4.2.5.1	Pure Soft Mode	81
4.2.5.2	Soft-rigid Hybrid Modes	82
4.2.5.3	Rigid Mode	84
4.2.6	Programmability Setting	84
4.2.7	Design & Fabrication	86
4.3	Results	92
4.3.1	Fiber-reinforced Pneumatic Actuator Expanding Test	92
4.3.2	Fingertip Force Test	93
4.3.3	Locking Mechanism Force Test	96
4.3.4	Multi Curvature Bending Test	98
4.3.5	Grasping Capability	109
4.3.6	Grasping Performance	114
4.3.7	Durability Test	117
4.3.8	Tensile Tests of SLA 3D-printed Material	118
4.4	Discussion and Conclusion	124
5.	A Normally Open Passive Microfluidic Valve	126
5.1	Introduction	126
5.2	Method	130
5.2.1	Design	130
5.2.2	Passive Microfluidic Valve Three States	134
5.2.3	Combustion Chamber Pressure Hypothesis	136
5.2.4	Fabrication	139
5.2.5	Experiment Setup	142
5.3	Results and Discussion	143
5.3.1	Pressure Test for State Switched	143
5.3.2	Pressure Test for Changing the Chamber Heights	146
5.3.3	Flow Rate Test	147
5.3.4	Flow Rate Improving Test	149
5.4	Conclusion	150

6. Concluding Remarks and Future Work	152
Appendix A Chapter 3 Euler-Bernoulli Beam Theory and Mechanics of Materials, Brief Overview	158
Appendix B Chapter 3 Vision Algorithms Detail	161
Appendix C Chapter 3 Fabrication Detail	163
Bibliography	165

List of Figures

2.1	Type of jamming. (A). Zero dimension “points” Granular jamming, able to move freely in all directions. When vacuum is applied, points are compressed in X, Y, and Z, increasing resistance to movement. (B). One dimension “lines” fiber jamming able to bend about X and Z, but not stretch along their length Y. When vacuum is applied, fibers are compressed in X and Z, increasing bending stiffness. (C). Two dimension “planes” layer jamming able to bend about X but not stretch in X or Z. When vacuum is applied, layers are compressed in Z increasing bend stiffness. The x and y axes in (C) denote the plane of the layer jamming. The y axis in (B) denotes the fiber direction in fiber jamming. Below. The ‘+’ indicates high stiffness, the ‘-’ indicates low stiffness, and the ‘N’ indicates neutral stiffness.	20
3.1	Soft sensors. (A). Elastomeric finger containing a microfluidic pressure sensor and nine fiber-based deformation sensors to sense pressure, bending, elongation, and twist. (B). Illustration of the elastomeric finger with fiber and fluidic sensors routed through the finger to a display assembly, where sensor positions are read by a digital camera. (C). Fiber-based deformation sensors, relaxed and bent states. Finger (top) and fiber states (bottom). (Stills from Video S1.) (D). Integrated microfluidic pressure sensor, senses overall pressure. (E). Surface-mount pressure sensor senses contact locally on the finger’s surface. (F). Cephalopod-Chromatophore inspired color cell pressure sensor. External force causes the cell to change shape from spherical to a disk shape, changing disk diameter.	28
3.2	Fiber sensors, underlying concepts. (A). Mechanics of materials in elongation, bending, and twist. (B). Traditional vs. soft sensors. Traditional (top), each sensor requires separate electronics and support. Bottom, multiple fiber sensors all routed back to display assembly. One camera records all sensors. One actuator is indicated in blue. Two additional actuators are indicated in red. (C). CAD of assembly with the first (blue) actuator and two additional (red) actuators. Note, Camera records display assembly, not soft actuators, for reduced complexity motion capture of many sensors at once.	31

3.3	Fabrication. (A). Elastomeric finger containing fiber-based displacement sensor and integrated fluid pressure sensors. (A1–A3). An elastomeric finger is fabricated in three mold steps, containing channels for the nine fiber sensors and an integrated fluid pressure sensor. Molds are shown in gray. (A4). Finished elastomeric finger, transparent representation to illustrate internal vasculature. (A5). A finger is instrumented with fibers and integrated with the display assembly. (B). Surface mount liquid pressure sensor is molded (B1), bonded to a base layer (B2), then bonded to an elastomeric finger, and infilled with colored water (B3). (C). Chromatophore cell is molded into an elastomeric substrate and infilled with colored water (C1), then sealed with elastomer (C2), yielding a final sensor (C3).	38
3.4	Test fixtures. (A–E) fiber-based displacement sensors, (F–I) fluid-based pressure sensors (A). Fiber sensor configuration. (B). Bend test setup. Elastomeric finger mounted horizontally, pulled from neutral to deformed (bent) state. (C). Elongation. Finger mounted vertically, top-end pulled vertically. (D). Fibers in the display assembly. Left neutral state, right when deformed (shown in bend direction 2). (E). Finger mounted horizontally, twisted along its axis (shown in two views). (F). Integrated fluidic pressure sensor undergoing compression. (G). Surface-mount fluidic pressure sensor undergoing compression. (H). Chromatophore inspired pressure sensor undergoing compression. (I). Chromatophore sensor deflecting under pressure.	42
3.5	Results, fiber sensor marker displacement (pixels). Fiber configuration is shown in the upper left of each subfigure. Sample images of marker displacements are shown in the lower left of each subfigure (1 top... 9 bottom). (A). Bending direction 1. (B). Bending direction 2. (C). Elongation. (D). Twisting. Legend for all graphs, Fiber 1–9 shown in the upper right (near subfigure (C)).	43
3.6	Results, microfluidic pressure sensors. (A). Integrated microfluidic sensor. An elastomeric finger is shown under an externally applied load. The graph shows displacement of fluid in display assembly (red line in inset still from Video S2) vs. force applied on an elastomeric finger with an embedded sensor. (B). Surface-mount microfluidic pressure sensor. The graph shows displacement of fluid in display assembly vs. force applied directly to the surface-mount sensor. (C). Chromatophore inspired sensor. The graph shows the diameter of a fluid cell (shown as stills from Video S2) vs. externally applied load.	47
4.1	Illustration of force direction controllability with state corresponding to locking modules. The Blue arrow indicates the targeted force direction; the red dot indicates the joint is locked, and the green dot indicates the joint is unlocked and rotated freely.	57
4.2	Overview of the bioinspired finger system.	60

4.3	Bioinspired soft finger with a soft-rigid hybrid structure. (A). The overall components. (B). Two types of actuators are used for the finger (the yellow frame indicates a pneumatic actuator, and the red line indicates a tendon-driven cable). (C). Bioinspired soft finger with total 7 sets of Bowden cable assemblies, including 5 sets for locking modules, one for nail mechanism, and one is tendon-driven cable.	62
4.4	The finger parameters and index.	64
4.5	(A) Chain shape locking mechanism system. (B) One locking module, blue indicates two side-crown, red indicates as chain core, black indicates the Bowden cable and the tendon force. Leave space above each locking module for the Bowden cables to move freely between the locking modules and the pneumatic actuator (C) Side-crown with different views. There are two contact points on its upper half for connecting belt (D) Chain core with different views. Leave space in the middle for the tendon-driven cable to be embedded.	66
4.6	The yellow line indicates the elastomeric band perpendicular crossing the axes that provide a force to separate the core and the side-crown. . .	67
4.7	A locking module cross-section view. The red part indicates the chain core; the green part indicated the screws pass through the side-crown and secure to the chain core. The yellow line indicates the rubber band that provides the force to separate the chain core and the side-crown. The blue parts indicates the side-crowns, which have one DOF along the axis.	67
4.8	Illustration of when the first locking module is locked, the joints Q_2 and Q_1 will be locked so that the bending angle θ_2 and θ_1 is fixed as shown in red color. By analogy, when the i^{th} locking module is locked, joints Q_{2i} and Q_{2i-1} are locked, bending angle θ_{2i} and θ_{2i-1} are fixed.	68
4.9	Force diagram in the locking module. (A) Rigid mode or lock mode. (B). Soft mode or unlock mode.	69
4.10	Force analysis diagram of the locking module-chain core.	69
4.11	(A) The pneumatic actuator semicircular cavity view. (B) The cross-section view of the assembly finger shows the space under the pneumatic actuator for the Bowden cable sets.	74
4.12	Kinematic model of 10 DOF locking mechanism system in a 2D Cartesian space.	77
4.13	Pneumatic actuator fabrication process. The assembly is fabricated using three molding steps, and molds are shown in gray. (A) Mold A, the pneumatic actuator fingertip fabrication process, (A1-A4). (B) Mold B, the inner layer of the pneumatic actuator for winding reinforced fibers. (C) Mold C, finished pneumatic actuator fabrication.	86
4.14	Pneumatic actuator and nail mechanism bonding process. (A-E) the bonding process of the fabric to nail mechanism by SLA resin. (F-J) The bonding process of the nail mechanism and pneumatic actuator. (K)	

	Install a metal rod, elastic rubber band, and the nail into the nail mechanism.	90
4.15	Bioinspired soft finger assembly process step diagram.	91
4.16	Fiber-reinforced pneumatic actuator expanding test and results: (A) Test setup of the actuator in the elongation experiment. (B) Test result for pressure and elongation configuration with the linear trendline.	93
4.17	Fingertip force test and results: (A) Test setup of the finger on the Instron with all the locking modules in the unlocked state. (B) The pneumatic actuator input pressure and fingertip force output relationship plot.	94
4.18	Fingertip force experiment results with two actuators. The finger is setup on the Instron with all the locking modules in the unlocked state and the red line indicates the tendon-driven cable. The pneumatic actuator inflated to 35 kPa (5.1 Psi) and maintained it all time during the experiment, then activated the tendon-driven actuator at time 17s.	95
4.19	Locking mechanism force test setup. One locking module is set up horizontally on the test platform; the red line indicates the Instron force, and the black line indicates locking tensional force by Bowden cable. . .	97
4.20	Locking mechanism force test and results of the Instron force and locking tensional force relationship.	97
4.21	Multi curvature bending test results with 0-30 index modes.	99-109
4.22	A dozen different objects grasped by the fingers.	110
4.23	Three fingers mounted on Sawyer robots in different view.	110
4.24	Various objects grasped by the fingers. (A) Packaging tape, (B) Spray cleaner, (C) Paper cup, (D) Screwdriver.	111
4.25	Finger in the pre-shaped mode for gripping flat objects and smaller objects. (A) Nut, (B) coin, (C) fork, (D) student id card.	112
4.26	The use of the pre-shaped mode to grip the sponge and then apply the additional tendon-driven actuator to it for more force to the sponge to bend it.	113
4.27	Finger grasping in adaptive power mode with applying the tendon-driven actuator to provide additional force to squash paper cup.	114
4.28	Grasping performance. Gripping force of the finger in pneumatic driven only mode and pneumatic & cable-driven mode.	115
4.29	Grasping performance. Gripping force of the finger with all the locking modules are locked.	116
4.30	Durability test results. The orange line represents the average trajectory for the 1st to 5th cycles, and the blue line represents the average trajectory for the 95th to 100th cycles. The red marked point represents the reference point of Figure A.	117
4.31	The geometry of the tensile test's specimen.	119
4.32	(A) CAD file in PreForm slicer software; (B) SLA 3D printed specimens after post-cured.	120

4.33	Stress-strain diagram for the six tested samples grouped by construction angle in color.	121
4.34	Mean characteristics for each printed angle with error bars \pm Std. Dev.	122
4.35	The Clean V4 resin tensile specimens; (A) Before testing, (B) after testing.	122
4.36	Stress-strain diagram for the Formlabs Clear V4 resin mechanical characteristics comparison.	123
5.1	Schematic of the passive microfluidic valve design.	130
5.2	Passive valve design space.	133
5.3	Passive microfluidic valve three states.	134
5.4	Passive microfluidic valve state transition diagram.	135
5.5	The four-stroke cylinder pressure waveforms.	137
5.6	The state of the valves at different strokes.	138
5.7	Soft lithography fabrication process.	139
5.8	(A) Bonding process of PDMS to PDMS using low-power oxygen plasma. (B) A packaged three passive microfluidic valves prototype device.	141
5.9	Experiment setup (A) is used to test the pressure. (B) is used to test the flow.	142
5.10	Three states transitions and test results.	144
5.11	Test valves, 9 valves in total.	147
5.12	Flow rate test results.	148
5.13	Flow rate improving test results. The red dotted line indicates the desired minimum flow rate (goal) of 1 cc/second.	150
6.1	Concept of the integrated sensorized stiff-soft finger overview system.	156
A1	Mechanics of materials. (A). Beam in tension. (B). Beam in bending. (C). Beam in torsion. (D). length of a helix.	158
A2	Elastomeric finger fabrication process. (A). Mold 1. (B). Connect vasculature to micro-fluidic pressure sensor. (C). Mold 2. (D). Mold 3. (E). Connect fibers. (F). Routing cables through base holder. (G). Integrate finger with Display Assembly.	164

List of Tables

4.1	Comparison of soft–rigid hybrid grippers characteristics.	56
4.2	Parameters of the finger.	65
4.3	Parameters of the locking module.	70
4.4	D-H Parameters for the locking mechanism system.	77
4.5	Pure soft mode grasping procedure.	82
4.6	Adaptive power mode grasping procedure.	83
4.7	Pre-shaped mode grasping procedure.	84
4.8	Pre-program mode grasping procedure.	85
4.9	Compare maximum grasping force in three different modes.	116
4.10	Formlab Clear V4 resin datasheet comparison with our experiment.	123
5.1	Comparison of rigid components and chemical reaction energy densities	128
5.2	Valve parameter for 5.3.1 section and baseline reference.	143
5.3	Valve parameter for 5.3.2 section.	146
5.4	Pressure test for changing the chamber heights results.	146
5.5	Valve parameter for 5.3.3 section.	147
5.6	Valve parameter for 5.3.4 section.	149

List of Notations

δ	Total displacement
P	Applied load
L	Total beam length
L_{helix}	Length of the helix
ΔL	The change in length
A	Beam cross-section area
E	Young's Modulus
σ_x	Tensile or compressive stress
M	Applied bending moment
y	Distance from the neutral surface
I	Second moment of inertia
ϵ_x	Strain in the beam axis
ρ	Radius of curvature of the bent beam
τ	Shear stress
T	Applied torque
J	Polar moment of inertia
ϕ	Total twist of the beam
G	Shear modulus
r	Distance from twist axis
W_{finger}	Finger width

L_{finger}	Finger length
B_{finger}	Finger base pedestal width
H_{finger}	Finger height
θ_t	Fingertip angle
l_{ai}	Pneumatic actuator segment length
h_t	Maximum nail elongation high
l_i	Locking mechanism segment length
Q_i	Rotation joint
θ_i	Bending angle on the i^{th} joint
Q_{tip}	Fingertip endpoint
θ_{end}	Total bending angle of end-effector nail mechanism
LM_i	The i^{th} locking module
τ_q	Torque on the rotating joint
N	Teeth number/ Newton
d_p	Pitch circle diameter
d_{in}	Inner circle diameter
d_{out}	Outer circle diameter
f	Overall force
f_t	Total tangential force
f_{tn}	Tangential force on each tooth
ϕ_p	Pressure angle
ψ	Pitch angle
f_h	Yellow hypotenuse
f_r	Radial force
f_a	Axial force
r_{arm}	Moment arm

a_i	The length of the link about the common normal
α_i	Angle about common normal, from old z_{i-1} to new z_i
d_i	Offset along with previous z_{i-1} to the common normal
c_i	$\cos(\theta_i)$
s_i	$\sin(\theta_i)$
$c_{ijk\dots}$	$\cos(\theta_i + \theta_j + \theta_k + \dots)$
$s_{ijk\dots}$	$\sin(\theta_i + \theta_j + \theta_k + \dots)$
H_{up}	Upper chamber height
H_{low}	Lower chamber height
ϕ_{in}	Inlet diameter
ϕ_v	Valve diameter
W_c	Channel width
W_i	Island width
M	Membrane thickness

Table of Acronyms

ADC	Analog to digital converter
CSV	Comma-separated values
DAC	Digital to Analog converter
DEA	Dielectric elastomer actuator
D-H	Denavit–Hartenberg
DOF	Degrees of Freedom
EAP	Electroactive polymer
EGaIn	Eutectic of Gallium and Indium
MEMS	Micro-electromechanical systems
PDMS	Polydimethylsiloxane
PEB	Post-exposure bake
PMMA	Polymethyl methacrylate
PTFE	Polytetrafluoroethylene
SLA	Stereolithography
SMA	Shape-memory alloys
SMP	Shape memory polymer
TDA	Tendon-driven actuator
TMCS	Trimethylchlorosilane

Abstract

Novel Approaches to Soft Robot Actuation and Sensing; A Bioinspired Soft-rigid
Hybrid Finger with Variable Stiffness Modules

by

Keng-Yu Lin

Soft robots are a new field in robotics that shows an increasing potential to dramatically expand the capabilities of robots. We have analyzed the advantages and disadvantages of traditional rigid robots and soft robots, as well as the timing and occasions for their application. The characteristics of these two types of robots are completely different. However, in real human life, we are faced with a situation that falls between the characteristics of these two types of robots. Sometimes we need to grasp fragile objects, sometimes we need to lift heavy objects, and sometimes we need to press buttons or electrical switches and other daily actions. We need to think more formally about whether soft robots can perform these tasks and what critical areas are still lacking that need to be addressed. Thus, their underlying subsystems (actuation, sensing, control) and their role in robotics must be reconsidered. We first rethink sensing, in which traditional rigid robot sensing is very intuitive, using as many sensors as their degrees of freedom to describe the state of the robot. However, for soft robots, sensing becomes very difficult. Secondly, we rethink actuation; soft actuators are great

for applying a distributed force on fragile objects. But the backdrivability that gives them the advantage also limits their ability to generate high forces.

In this dissertation, we rethought the soft systems and proposed the fundamental novel types of soft sensor and actuator necessary to develop the field of soft robotics from interesting concepts to useful devices. We demonstrate a network of fiber-based displacement sensors to measure robot state (bend, twist, elongation) and two microfluidic pressure sensors to measure overall and local pressures. The fiber-based sensors are fundamentally designed to be used in groups and leverage the concepts from beam theory and mechanics of materials to infer system state from a strategically located system of sensors. Intended to be built into a soft robot at the system level, a properly configured array of these deformation and pressure sensors can give state awareness far beyond that of individual sensors.

We present a bioinspired soft finger with a soft-rigid hybrid structure that can have multiple curves and force direction controllability to provide force in a specific direction. The soft and rigid states of multiple independent locking modules can be controlled independently by connecting them into a chain-like system. We have performed a modeling analysis of this controlled soft-rigid module, which provides an adaptable and scalable design framework for future bioinspired robotic fingers. We propose a new soft-rigid hybrid structure design and a method of interaction between pneumatic and tendon-driven actuators. The two actuation methods can increase the finger's flexibility, allowing it to grasp objects of various shapes, sizes, and weights quickly and stably while providing sufficient force in specific directions. We have also

added a nail mechanism to the tip of the finger, which helps the finger grip flat or small objects.

Lastly, we studied the possible power source of soft robots and found that if we look at the energy density alone, chemical reactions can provide a higher energy source than those energy sources with rigid components such as lithium batteries, compressed air, liquid carbon dioxide, etc. However, the challenge of chemical reactions is to control the fluid efficiently. We develop a normally open passive microfluidic valve with reduced-order control for a micro-combustion chamber. This passive microfluidic valve can be installed on a micro-combustion chamber and is responsible for all fluid control, including intake and exhaust. This novel passive microfluidic valve may also be used in other applications, such as sensors for soft robotics.

Acknowledgments

My doctoral study journey has entered the final countdown at the end of this thesis. This four-year period has brought me too much intellectual improvement and growth in my life. Completing this dissertation would not have been possible without your support and encouragement. This may be the last moment of my campus life. I want to express my most sincere thanks to the professors, friends, classmates, and family who have helped me, cared about me, and accompanied me through this fulfilling doctoral life.

First and foremost, I would like to express my heartfelt thanks to my advisor, Dr. Michael Wehner. Your rich life experience and profound knowledge are my role models. Your rigorous academic attitude keeps pushing me forward. Thank you for your guidance and assistance in my research direction. Whenever I encountered difficulties, you always showed me the way and supported me both in life and academically. Your willingness to provide me with so much time, inspiration, and valuable discussions is a major reason for the completion of this thesis.

I would like to thank my dissertation committee, Dr. Gabriel Elkaim, Roy Kornbluh, and Dr. Ronald Pelrine, for their time and interest in evaluating my work and giving me constructive comments and feedback.

Many thanks to my colleagues and collaborators; your efforts have been critical in getting this work done. To Arturo Gamboa-Gonzalez, thank you for your generosity

of time in helping me with the remaining experiments during this challenging and uncertain time. To Dongshuo Li (Tony), thank you for your encouragement and companionship during my Ph.D. program. I would also like to mention the people who have helped me and all my previous lab members who have graduated or are still in school, Dr. Dejan Milutinovic, Dr. Megan Boivin, Conrad Esch, Natalie King, Zachary Potter, Vaishnavi Dornadula, and Le Luo; all of you have also helped me create a great Ph.D. journey, and I really enjoyed working with all of you.

Thank you to all my friends who have stood by and supported me over the years and others I forgot to mention. You are all amazing, and you have been by my side at different stages of my life.

To my love, Xi Cheng, thank you so much for your support, advice, and encouragement. You have stood by my side during successes and failures, tirelessly encouraging and supporting me every day. Thank you for all your inspiring discussions and all your loving words. I look forward to many more fun times creating things together and taking on new adventures with you.

Finally, I would like to express my sincere gratitude to my family for their moral and financial support during my doctoral studies in the United States. Without your support, this Ph.D. would not have been possible.

This research was partially supported by a 2019 Seed Fund Award from CITRIS and the Banatao Institute at the University of California, UCSC Regents Fellowships

and was partially supported by the Hellman Fellow Program 2020 to Professor Michael Wehner. Their support is gratefully acknowledged.

A Note on Previously Published Material

The text of this dissertation includes reprint of the following previously published material:

- ▶ K.-Y. Lin, A. Gamboa-Gonzalez, and M. Wehner, “Soft Robotic Sensing, Proprioception via Cable and Microfluidic Transmission,” *Electronics*, vol. 10, no. 24, p. 3166, Dec. 2021

With regards to the authors of these reprints, the co-author Arturo Gamboa-Gonzalez (agamboag@ucsc.edu) and Michael Wehner (wehner2@wisc.edu) listed in these publications directed and supervised the research contained within this dissertation.

A Note on Chapter 5: A Normally Open Passive Microfluidic Valve

This material is based upon work supported by the Defense Advanced Research Projects Agency (DARPA) under Contract No. HR0011-19-C-0047.

Any opinions, findings and conclusions or recommendations expressed in this material are those of the author(s) and do not necessarily reflect the views of the Defense Advanced Research Projects Agency (DARPA).

Chapter 1

Introduction

1.1 Motivation

Traditional rigid robots have been very successful in performing highly accurate and repeatable tasks and are made of rigid materials or metal parts with linkages and joints. In highly structured environments, traditional rigid robots have been widely used in industry for many years, such as assembly lines in manufacturing, due to their high load capacity, programmable operating tasks, and high precision motion control. However, they are not very good at handling uncertainty in contact in unstructured environments [1], [2]. In recent years, however, there has been increasing concern about the safety of human-robot collaboration. Such rigid robots in factories are often designed to move quickly and apply high torque, which can be dangerous when in close contact with people or other fragile objects. As production demands continue to increase and new products are being replaced at an accelerated rate, so do the requirements for robotic versatility. One of the common problems is that manufacturers need more robotic arms and more human resources to work in the same open space to increase efficiency. In this case, traditional rigid robots can pose a safety

hazard to humans in open work environments due to their lack of compliance with the environment.

Inspired by the soft flexible manipulation often found in nature [3], [4], soft robots are designed to use flexible joints or composed of soft materials in order to reduce the complexity required for the system to interact safely with humans [2]. The emerging field of soft robotics involves devices made of compliant (low Young's Modulus) materials, often characterized by an ability to adapt to the surrounding environment like a living organism [5]. In the last decade, the soft robotics field study has significantly grown and become a new robotic family member [6]. This emerging field has involved research far beyond traditional robotics. Researcher has involved fields as diverse as material science [7], biology [8], mechanical and electrical engineering [9], [10], and even chemistry [11]. The manufacturing process of soft robotics can be made by mold casting [9]–[12], multi-material 3D printing [13], [14], injection molding, soft lithography [15], [16], or multiple fabrication techniques to embed multi-composite materials [17], [18]. Most of the driving methods for soft robotics are fluid-driven, pneumatic [9], [10], [12], [16], [18], and hydraulic [19] to inflate the soft robot chambers. However, many other actuation techniques have been explored including cables in tension [20], [21] or compression [22], shape memory alloy [23], shape memory polymers (SMPs) [24], dielectric elastomer [25], [26], and piezoelectric polymer films [27]. Soft robots offer almost infinite degrees of freedom, allowing them to perform simplified tasks; for example, soft grippers can fit irregularly shaped objects and reduce the risk of injury caused by conventional rigid robots. Soft

robots may provide alternative solutions for more applications that interact directly with humans. Soft robots also have the advantage of low cost and reduced manufacturing complexity due to their simple structure and the small number of components.

Despite the many advantages of the soft robot's flexibility, the completely low stiffness of the soft structure has its drawbacks. Due to their flexibility, soft robot components have fewer motion constraints that are challenging to sense and model [2], [28]. Their motion becomes even more unpredictable when it is in contact with objects in the operating environment. Because soft robots offer almost infinite degrees of freedom, the number of current sensors required to understand the state of a soft robot greatly exceeds the number required to determine the pose of a traditional rigid linkage robot [29]. It can also be found in the biological field that completely soft animals are mostly small in size, while large animals usually have a rigid skeleton to support their weight [2]. Large soft mollusks, such as squid, and other large soft animals without skeletons, such as jellyfish, generally live in water; other soft animals are generally smaller and live underground, such as earthworms, and cannot survive without the medium that supports their bodies. It is evident that it is necessary to study soft robots with variable stiffness capability and adaptability to natural environments.

Therefore, we believe that an ideal soft robot should have the following structural characteristics: it should be able to show a high degree of flexibility during movement, demonstrate variability stiffness when performing a specific task, and use an efficient sensing system to know its state or posture.

In our vision, we believe soft robotics will act as a bridge between humans and traditional robots. When soft robot technology walks into our home, it helps us do our work in a more efficient way without any safety concerns. To achieve this, we focus on the end-effector, the component most commonly used for contact with the environment and any direct interaction with humans. Here, we propose a low-cost soft-rigid hybrid structure bioinspired finger that can achieve fast response, energy efficiency, multi-segment stiffness control, and high stiffness ratio control. This hybrid structure finger also allows the controlled transitions that will enable the finger to exhibit both soft and rigid robotic finger behaviors. Furthermore, we develop a new sensing system for soft robots to reduce the number of interfaces required between soft robot and controller.

1.2 Theoretical Framework

Soft robotics is a new field in robotics that shows an increasing potential to dramatically expand the capabilities of the field. In the previous section, we briefly discussed the advantages and disadvantages of traditional rigid robots and soft robots, as well as the timing and occasions for their application. Based on fundamentally different operating principles and built materials with vastly different mechanical properties, traditional and soft robots excel in fundamentally different types of tasks. Traditional robots provide high forces and precise positioning in structured environments. Soft robots provide distributed forces and an ability to conform as necessary in unstructured environments and in handling fragile objects. In real human

life, we are faced with a situation that falls between the characteristics of these two types of robots. Sometimes we need to grasp fragile objects, sometimes we need to lift heavy objects, and sometimes we need to press buttons or electrical switches and other daily actions. We need to think more formally about whether soft robots can perform these tasks and what critical areas are still lacking that need to be addressed. Thus, their underlying subsystems (actuation, sensing, control) and their role in robotics must be reconsidered.

We first rethink sensing. Traditional rigid robot sensing is very intuitive, using as many sensors as their degrees of freedom (DOF) to describe the pose of the robot. However, for soft robots, sensing becomes much more difficult. We first have to overcome the problem of how the sensor itself is installed on the robot and then how many sensors are required to provide enough information to the controller to complete the control computation. We know that the more completely we can know the state of the robot, the more accurately we can control it. Therefore, for a soft robot with infinite DOF, it must have enough sensors to ensure good control. In a conventional robot, less than 10 sensors may be needed to determine pose and interaction, but in a soft robot, more than 100 sensors may easily be needed. For current soft sensors, it is difficult to increase the number of sensors without adding additional components. So we need to solve the problem of how to reduce the burden of the rapid growth of multiple soft sensors used. Once we solve this problem, the control of soft robots can be easier and more accurate.

Secondly, we rethink actuation; soft actuators are great for applying a distributed force on fragile objects. Readily deforming when encountering external force, compliant soft actuators conform to the shape of an object they are grasping, distributing force across large surfaces, and minimizing local contact forces. This compliance makes soft robots well suited for interaction with delicate or even living specimens. But the backdrivability that gives soft actuators their primary advantage also limits their use. If one attempts to operate a plastic spray bottle (the type that often contains household cleaners), the gripper will back drive out of the way and guarantee no damage to the bottle. But this compliance will also prevent the actuator from pressing the trigger and operating it as desired. So we need to develop a structure that enables soft robotic fingers to exhibit softness and rigidity as appropriate for the application.

In the work presented here, we rethought the soft systems and proposed the fundamental novel types of soft sensor and actuator to develop the necessary for the soft robots field from interesting concepts to useful devices.

1.3 Thesis Contributions

The research presented in this thesis is based on the underlying theoretical framework of rethinking the fundamental principles behind soft robots. This resulted in novel sensors and dividing actuation into fundamental sub-categories. Based on that conceptual re-thinking, the work presented in this thesis is illustrated via physical demonstrations, which are applied in nature and pursue three main contributions. The

main problem of the study is centered around how to achieve a combination of high stiffness ratio control, fast response, energy efficiency, and multi-segment stiffness control to emulate a human finger and the ways to improve soft robotic sensor systems. We aim to develop new frameworks that apply multiple existing actuation methods for the bioinspired soft finger to perform like a human and develop a novel soft sensing system to improve accuracy and reduce the computation and data acquisition load. The contributions of the research are the following:

1. A novel soft sensing system can provide higher accuracy and expand the number of sensors without increasing the electronic and computational hardware infrastructure.
2. We propose a new soft-rigid hybrid structure design and rethink how to achieve multi-segment stiffness control to emulate a human finger. This hybrid structure combines the benefits of soft robotic and rigid fingers with the ability to provide force in a specific direction.
3. We create a normally open passive microfluidic valve with reduced-order control for a micro-combustion chamber that can be used in future soft robotics applications. In forwarding flow, the valve achieves a flow rate of 1 cc/s at a pressure of 1 psi. It can also be blocked at 1.5 psi in reverse flow and can withstand reverse pressure of 30 psi.

The sensors are primarily intended to be used in groups. A properly configured array of these deformation and pressure sensors, intended to be designed into a soft robot at the system level, can provide state awareness far beyond that of individual sensors. Often, sensors are designed individually. With only a few sensors required for

state (pose plus contact/interaction forces) estimation, these individual sensors have proven sufficient in many traditional robot applications. The resistance or capacitance of most soft robot sensors (and many sensors in general) varies in response to a change in a physical parameter such as length, bend angle, or contact pressure. Before the resulting signal is sent to a computer, each sensor requires wiring, electronic circuitry, and a dedicated input to a data acquisition system. Five sensors necessitate a fivefold increase in infrastructure. With our presented method, a digital camera is used to record the movement of markers on fiber sensors and colored liquid in microfluidic channels. As a result, dozens of markers and fluid channels can be monitored almost as easily as one.

We present, as well, a novel robotic gripping system using pneumatic, cable, and locking techniques (separately and in concert) to achieve novel modes of actuation. We present a new soft-rigid hybrid structure design as well as a method for separate pneumatic and tendon-driven actuators to interact. The newly developed segmented controllable soft-rigid module combines the benefits of a soft robotic finger with the ability to provide force in a specific direction. We conducted a modeling analysis of this controlled soft-rigid module, which provides a flexible and scalable design framework for bioinspired robotic fingers. We compare the mechanical model of a single locking module to the overall kinematic analysis, as well as the combination of each locking module used with the actuator. This includes pure soft mode, soft-rigid hybrid mode, and rigid mode to validate our model using experimental data. In the grasping performance test, we demonstrated that this soft-rigid hybrid structure of the

soft finger could provide a maximum gripping force of 125N with a single finger when all locking modules were locked. In the experiment, we used paper cups and sponges to demonstrate how the finger can quickly adapt to the shape of the gripping object, adjust the gripping arc, and deliver force in a specific direction. We believe that the method of soft-rigid hybrid structural design interacting with multiple actuators provides a scalable and adaptable design framework for future bioinspired fingers, based on the kinematic analysis and experimental results. We focused on a bioinspired soft finger with in-plane motion in this study and established different grasping modes.

Finally, we present a new passive microfluidic valve that can be installed on a micro-combustion chamber and is responsible for intake and exhaust fluid regulation tasks. This novel mode of passive actuation allows for controlling combustion reactions at a small (e.g., millimeter) scale. The valve achieves a flow rate of 1 cc/s at a one psi input pressure in forwarding flow and can also be blocked at 1.5 psi in reverse flow.

1.4 Thesis Outline

The structure of this thesis is organized as follows.

Chapter 2 reviews and summarizes the state of available literature and focuses on the soft robotic actuator, soft robotic sensor, and variable stiffness structure.

Chapter 3 demonstrates a network of fiber-based displacement sensors to measure robot state (bend, twist, elongation) and two microfluidic pressure sensors to measure overall and local pressures. The fiber-based sensors are fundamentally designed to be

used in groups and leverage the concepts from beam theory and mechanics of materials to infer system state from a strategically located system of sensors. Intended to be built into a soft robot at the system level, a properly configured array of these deformation and pressure sensors can give state awareness far beyond that of individual sensors.

Chapter 4 presents a bioinspired soft finger with a soft-rigid hybrid structure that can have multiple curves and force direction controllability to provide force in a specific direction. The soft and rigid states of multiple locking modules can be controlled independently by connecting them into a chain-like system. We have performed a modeling analysis of this controlled soft-rigid module, which provides an adaptable and scalable design framework for future bioinspired robotic fingers. We propose a new soft-rigid hybrid structure design and a method of interaction between two pneumatic and tendon-driven actuators. The two actuation methods can increase the finger's flexibility, allowing it to grasp objects of various shapes, sizes, and weights quickly and stably while providing sufficient force in specific directions. We have also added a nail mechanism to the tip of the finger, which helps the finger grip flat or small objects.

Chapter 5 develops a normally open passive microfluidic valve with reduced-order control for a micro-combustion chamber. This passive microfluidic valve can be installed on a micro-combustion chamber and is responsible for all fluid control, including intake and exhaust. This novel passive microfluidic valve may also be used in other applications in the future, such as sensors for soft robotics.

Chapter 6 concludes all the results and the dissertation with a summary of discussion and directions for future research.

Chapter 2

Background and Literature Review

In this chapter, we identify and describe some previous research work on topics relevant to this thesis. We focus on results related to manipulators and finger-like actuators. This includes a comparison of the current status of different soft robot actuation technologies, soft sensor technologies used with soft actuators, and the structural design of variable steels.

2.1 Soft Robot Drive Method

Fluidic actuation

A fluid actuator means that the power source of the soft gripper is fluid, also known as fluidic elastomer actuators (FEAs) [2], [16], [18], [30]–[34]. The most common fluids in nature are liquid and gas, and the design of the soft gripper mainly uses gas as the power source because, compared with liquid, gas has better circulation, lighter weight, and better safety. At the same time, the pneumatic drive has the advantages of rapid response, easy access to the driving medium, and simple operation. Pneumatic actuation is gradually becoming the mainstream driving power source of the soft gripper. The principle of pneumatics is to change the air pressure inside the drive mechanism; due to the elasticity of the actuator, the change in air pressure deforms the

actuator, causing bending and extension. Most pneumatic soft actuators operate on positive pressure. However, a small number of devices have been designed to actuate based on negative air pressure (pressures between ambient and vacuum) [35]. Compared with negative pressure-driven, the positive pressure-driven is easier to control. This type of drive is commonly used in wearable devices [36]–[38] and pneumatic artificial muscle, also known as McKibben actuators [39], [40].

Tendon-driven actuation

Tendon-driven actuator (TDA) refers to a flexible-inextensible element (rope, fiber, cable, chain) called a tendon, which is attached to a mechanism to cause displacement via tension. The tendon may bend with the mechanism or not, and may be guided by structural elements in the assembly or simply in tension. Generally, the tensile strength of the rope (in the length direction) is large, but it is easy to bend in the radial direction and has high flexibility, which is very suitable for the characteristics of the soft robot. Therefore, embedding or fitting the rope inside the soft robot will not affect the performance of the soft robot itself. Generally, there is a special track or guide slot inside the soft robot for the placement and movement of the rope. There are several fixed points inside the special track and guide slot for the fixation of the rope to prevent the rope from deviating from the established track during the movement, such as the Bowden cable. Under the action of an external motor or other power sources, the rope contracts and pulls the soft substrate of the soft robot through the special track and guide groove, thus enabling the soft robot to bend or twist and grasp the object [21], [41]–[44].

Shape-memory alloy actuation

Shape-memory alloys (SMA) are a special class of materials whose internal structure switches between two forms. Under normal conditions, shape memory alloys are susceptible to deformation, similar to the soft substrate of a soft robot. However, under the action of an elevated temperature, shape memory alloys can return to their initial state and output torque during the return to the initial state. Generally, the structure of the soft gripper made of shape memory alloy is simple, and its deformation process is only affected by the temperature factor, and its performance is relatively stable [45]–[49].

Electroactive polymer actuation

The main body of electroactive polymer (EAP) actuation is usually a new type of material that can be deformed under the action of electricity. Generally divided into Ionic and Dielectric varieties, EAP's either bend (ionic) or contract/expand (dielectric). Under the action of voltage, Ionic EAPs, the mobility and diffusion of ions change the shape. Due to the limitation of material properties, the driving part of such a soft robot is generally made into a thin sheet shape and embedded in the inside of the fingers of the soft gripper [50], [51].

Dielectric elastomer actuation

Dielectric elastomer actuators (DEAs), which belong to the group of (EAP), are a promising soft actuation technology that achieves desirable biomimetic motion [25], [26], [52], [53]. DEAs are actuated by electrical voltage and benefit from its advantages

such as high energy density, large actuation strains, high electromechanical efficiency, and fast response. More detailed insights into DEAs applications and soft robotic systems and challenges associated with creating soft robotics are provided in the references [54]–[56].

Chemical reaction driven

In chemical reaction driven, convert other forms of energy directly into mechanical energy through chemical reactions, thus bypassing the intermediate electrical energy process. This can greatly improve the efficiency of energy conversion and also reduce the use of hard components. For example, researchers have 3D printed combustion-driven soft robots to achieve jumping motion without connecting to external components, and Wehner et al. proposed the Octobot, which uses microfluidic technology and the chemical reaction driven [17], [57], [58].

2.2 Soft Robotic Sensor

It is difficult to attach or install conventional sensors to the soft actuator due to the flexibility, large deformation, and nonlinear characteristics of the soft robotic structure. The large deformation during operation also affects the accurate output of the sensor and may cause damage to the soft robotic actuator or the sensor itself. There are currently some commercial flexible sensors on the market that can withstand relatively large deformations, such as Flexiforce from Tekscan [59] and Flexpoint's bend sensor [60]. The modulus of the materials used in these flexible sensors is still larger than the

materials used for soft robotics, so it is difficult to apply them directly to soft robotics. Therefore, researchers started to study soft robotic sensors.

A very popular soft robotic sensor uses a conductive fluid embedded in a soft actuator or flexible microchannel. When stretched, the geometry of the channel changes, resulting in a change in electrical resistance. By measuring the change in resistance, the strain (or amount of stretching) can be calculated. Two examples of this method are a eutectic of indium gallium alloy (EGaIn) [61]–[65] and an ionically conductive gel [18].

Another very useful method is capacitive and inductance sensors that measure the capacitance or inductance variations caused by geometry changes when the elastic body is deformed [66], [67].

An optical soft robotic sensor detects a change in the phase or intensity of light caused by strain or pressure applied to an optical transmission medium. It typically consists of a light source, a photodetector, and an optical transmission medium tube or fiber. Optical soft robotic sensors are highly deformable and insensitive to electromagnetic interference and environmental contaminants [68]–[71].

2.3 Variable Stiffness Structure

Currently, there are two main categories of stiffening methods for soft robots: phase change materials and jamming structure. The principles of these two methods are:

(1) Material phase change: The principle of this change in stiffness is based on the material properties that constitute the soft robot. The liquid metal is one of the typical cases of material phase transition, and the stiffness of the soft robot is changed by the transformation between the solid and liquid state of the material under specific conditions.

(2) Jamming structure: This method mainly increases the frictional force between the medium inside the soft robot for variable stiffness through some external conditions, such as layer jamming, fiber jamming, and granular jamming. These three variable stiffness methods are based on increasing the internal friction of the structure. These jamming methods will be further explored in the following section.

In a demonstration of Method (1), Material phase change, researchers developed a new thermally adjustable composite material, wax-coated polyurethane foams, to realize the stiffness change [7]. A wax coating composite is applied to the surface of the actuator. After the wax coating is cooled and hardened, the actuator exhibits high stiffness with good stability, and no deformation occurs when an external force is applied to the actuator. When the wax coating is heated and melted, the driver is deformed under the external force and exhibits very low stiffness. The thermally tunable composite material achieves the change in stiffness by taking advantage of its property of being reversible between the glassy and liquid state at different ambient temperatures. When thermally tunable composites are heated, they undergo a glass transition, and their modulus of elasticity decreases sharply, thus achieving a change in the stiffness of the material.

There is also a variable stiffness structure that utilizes shape memory polymer materials (SMP) [72]. The actuator is inflated and pressurized to achieve bending deformation, and the stiffness of the actuator is changed by heating and cooling of the shape memory polymer layer. While the use of thermally activated shape memory polymer materials allows for reversible changes in stiffness, the response is slow, and the reversal process has to wait for the shape memory polymer to cool completely.

The liquid metal stiffening method generally uses the low melting point metal's own properties to achieve the stiffening effect [73]. The low melting point alloy is embedded inside the soft robot, firstly, the low melting point alloy is transformed into the liquid state by external heating, and then the low melting point alloy is cooled when the deformation of the soft robot reaches the specified shape, then the low melting point alloy is transformed into the solid-state so that the soft robot shows the high stiffness characteristics of the metal.

2.3.1 Three Types of Jamming

From the sequence of development, we have three types of jamming structures which are granular jamming, layer jamming, and fiber jamming [74]–[81], [81]–[85]. All of them make up a collection of components that have lower stiffness. To control the variable stiffness, force is applied to the jamming structure, increasing the contact force between the jamming elements. The resulting frictional coupling between the components increases, which causes dramatic changes in mechanical properties. When

applied to soft robots, the three types of jamming structures have their own characteristics.

Granular jamming [76]–[78] is composed of a large number of “granules”, approximating points or zero dimension particles enclosed in an elastomeric membrane. This is the most deformable system, and it can handle relatively large compression forces from any direction. Approximating zero dimension points, granules are free to move in any direction, limited only by interaction with other granules or the elastomeric membrane. This jamming structure requires more volume when applied with soft robotics and it is heavier than the other structures.

Layer jamming [74], [82]–[85], and fiber jamming requires less volume and are relatively more stable than granular jamming. Layer jamming is a kind of variable stiffness method with good effect and is easy to realize. It is generally composed of multi-layer sheets structure in the closed space. Under the action of negative pressure, the multi-layer sheet-like structures in the closed space are squeezed against each other, resulting in a large static friction force, which is equivalent to forming a thick whole with a certain length, thereby increasing the stiffness. The structures of layer jamming and fiber jamming are made of non-fluidic planar sheets or fibers. Under this structure, it's easier to maintain the shape of the structure when switching mode between non-jamming and jamming states than granular jamming. Layer jamming is great for supporting tension force parallel to the jamming layer.

Fiber jamming [75], [79]–[81] is the latest developed method, and its structure is the lightest of the three. The structure consists of long and slender elements, approximating one dimensional elements, able to bend freely but not able to elongate. Thus this structure exhibits good performance in the tension and compression force.

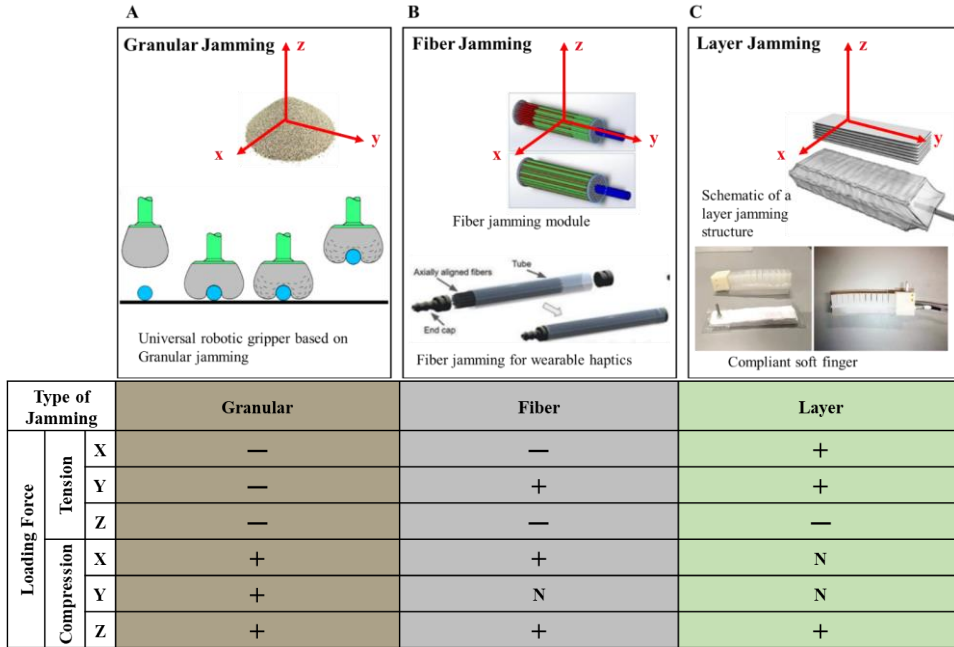


Figure 2.1: Type of jamming. (A). Zero dimension “points” Granular jamming, able to move freely in all directions. When vacuum is applied, points are compressed in X, Y, and Z, increasing resistance to movement. [76] (B). One dimension “lines” fiber jamming able to bend about X and Z, but not stretch along their length Y. When vacuum is applied, fibers are compressed in X and Z, increasing bending stiffness. [75], [81] (C). Two dimension “planes” layer jamming able to bend about X but not stretch in X or Z. When vacuum is applied, layers are compressed in Z increasing bend stiffness. [74], [86] The x and y axes in (C) denote the plane of the layer jamming. The y axis in (B) denotes the fiber direction in fiber jamming. **Below.** The ‘+’ indicates high stiffness, the ‘-’ indicates low stiffness, and the ‘N’ indicates neutral stiffness.

Chapter 3

Soft Robotic Sensing, Proprioception via Cable and Microfluidic Transmission

This chapter is based on the paper

- ▶ K.-Y. Lin, A. Gamboa-Gonzalez, and M. Wehner, “Soft Robotic Sensing, Proprioception via Cable and Microfluidic Transmission,” *Electronics*, vol. 10, no. 24, p. 3166, Dec. 2021

3.1 Introduction

Over the past decade, soft robots have shown an increasing potential to dramatically expand the capabilities of the field of robotics. Currently, however, most demonstrations have been limited to precisely that potential. For soft robots to emerge into human-populated environments and to perform useful real-world tasks, advances are required in sensors able to quickly provide robust state information, both as individual sensors and as integrated sensing systems. Soft robots hold the potential for unprecedented levels of interaction with the surrounding environment, impossible with traditional rigid-linked robots. This innate ability to yield to the environment and to

sense and learn from that interaction is one of the biggest potential advantages of soft robots. By embracing this ability to interact, soft robots can fundamentally change human-robot interaction and allow safe collaboration in the home and workplace. To achieve this leap forward in state awareness and embodied intelligence, a rethinking of soft sensing is necessary.

With this novel approach to robotics and interaction come novel challenges. The number of sensors needed to understand the state of a soft robot dramatically exceed the number needed to determine the pose of a traditional rigid-link robot. Traditional robotic manipulation techniques, including D-H parameters, Quaternions, and Product of Exponentials, assume rigid links connected by single (often rotational or prismatic) degrees of freedom [87]. Thus, one could define the entire range of possible poses of a traditional six-link robot using only six sensors. (Additional sensors would likely be included, but for other applications such as monitoring temperature and voltage.) Arguably, defining the pose of a single soft actuator, capable of yielding to the environment and several modes of self-motion, could require more than six sensors. Traditional robots typically contact the external world via manipulators (often end-effectors), with a limited number of small contact points or contact regions, often modeled using friction cone techniques [88] requiring a single multi-axis strain gauge or even a single axis pressure sensor. Contact with components other than predefined manipulators is unusual, and unplanned contact is avoided at all costs. Some of the main advantages of soft robots are their ability to distribute forces across broad regions of an actuator and that unplanned interactions are often of minor concern. Thus, where

a traditional robot may require fewer than 10 sensors to determine pose and interaction, a soft robot could easily require over a hundred. Several groups have tried machine vision methods to alleviate the rapidly growing burden of so many sensors, using cameras and motion capture to directly measure soft robot pose [33], [89], [90]. While this is effective in some applications, and the work is quite compelling, this technique is ill-suited to applications with a likelihood of obstructed views (such as reaching into boxes to retrieve objects in order fulfillment or laparoscopic surgery). Real-time processing of video to interpret complex 3D motions of an underactuated robot is also an extremely challenging task.

Many technologies have been presented to achieve myriad sensing modes in soft robots. Soft sensors (sensors composed of compliant materials, gels, liquids, or a combination of these housed inside a soft robotics component) have been developed using conductive grease[63], capacitive liquid [91], resistive ionic gels [32], waveguides [70], and many demonstrations with liquid metals [68], [92], [93], primarily focusing on a Eutectic of Gallium and Indium (EGaIn) [94]. These many sensor technologies can measure changes in length [95], bending [18], pressure [96], even temperature in the distal end of a soft fin-ger [97]. There has been work on mixed-mode sensing models [91], including Park et al. [62], able to sense pressure and two modes of stretch, all in one sensor. Other sensing techniques used in soft robotics have involved bonding traditional bend sensors to a soft actuator [98] and embedded magnets and hall effect sensors [99]. There has been work in optical methods, including the SOFTcell project by Bajcsy and Fearing [100], in which tactile response was

determined through optical analysis of a deformed membrane and video tracking of markers adhered to or embedded in soft components [33].

While these studies present compelling sensors, further development is necessary for utilizing a suite of sensors to increase overall state awareness. In both traditional and soft robotics, many have studied proprioceptive sensor systems, robot skin, and bioinspired sensing. Discussion of these broad fields can be found in reviews of various subspecialties [101]–[105]. The value of multi-sensor systems to perceive different proprioceptive or exteroceptive phenomena is widely appreciated. However, as the number of sensors is increased, the computation, data acquisition, and signal processing load drastically increase as well. Each sensor requires electronic circuitry, wiring to each sensor, and a dedicated channel to a data acquisition system or an analog to digital converter (ADC), requiring signal processing and computation. A sensor-skin with a grid of ten-by-ten sensors would be a relatively modest requirement for many perception applications. Using discrete nodes would require 100 dedicated sensors. Multiplexing by separating signals into 10 horizontal and 10 vertical sensors reduces the load to 20 separate sensors (with related disadvantages), which is still a considerable burden for a single sensor-skin device.

So far, soft sensors have primarily been developed as individual, standalone units. To scale the system from one to five sensors, one simply fabricates and integrates five sensors and five sets of required electronics, which interfaced to five ADCs and sent five signals to a microcontroller. The sensors in this work focus instead on passive sensors, which present position and pressure data to a digital camera for real-time or

offline data processing. Digital cameras, able to record multi-megapixel resolution, are readily available at low cost and are already present on many robot platforms. With our method, a single camera can record and interpret data from many deformations and pressure sensors, providing a platform for state perception and embodied intelligence research. This camera does not record the elastomeric finger itself. Rather, it records the remotely located display assembly (Figure 3.1A, B), where it tracks the motion of fiber-based displacement sensors and microfluidic pressure sensors. Recording the sensor states rather than the elastomeric finger itself presents several advantages. Firstly, no clear line of sight is needed. During typical robotic tasks, portions of a finger would often become obstructed when environmental objects or the robot itself come between the finger and the camera. Additionally, by remotely recording the display assembly, all aspects of recording (color, contrast, lighting) can be controlled to values optimum for marker tracking, impossible in real-world robotic applications. Finally, by tracking only monochromatic markers moving in well-defined horizontal or vertical paths in a controlled environment (no unanticipated glare/obstructions), extremely simplified vision algorithms can be used, allowing much faster processing. We present three techniques in which digital cameras record markers from fiber-based deformation sensors and microfluidic pressure sensors inside an elastomeric finger-like structure. We present an elastomeric finger with embedded fiber sensors and two modes of the microfluidic pressure sensor (Figure 3.1A, B). We present this system's ability to quantify elongation along and twist about a longitudinal axis and bending about the two orthogonal axes perpendicular to the longitudinal axis (Figure 3.1C). We also

present the technique's ability to quantify overall pressure via an integrated microfluidic sensor (Figure 3.1D) and local contact pressure via a surface-mounted microfluidic sensor (Figure 3.1E). These sensors (specifically designed to be used in groups) can be designed into soft robotic actuators and leverage the framework provided from beam theory and classical mechanics of materials to sense the state of each actuated unit. In addition, we present a Cephalopod chromatophore-inspired color-cell pressure sensor that detects changes in local pressure through the deformation of colored liquid cells (Figure 3.1F). Chromatophores have been widely studied for decades [106]–[108], and in recent years have become the inspiration for biomimicry and biomimetic work by the soft robotics community [109] using bulk deformation of a matrix to modulate appearance and spell out a word [110] or disrupting part of a surface using dielectric elastomers [111]. In this work, however, we flip the concept, using the color cell as a passive pressure sensor to estimate externally applied force, not as an active device, mechanically distorted to modulate appearance.

While the simple sensor designs presented here have value individually, the key contribution of this work is that the sensors are fundamentally designed to be used in groups and leverage the concepts from beam theory and mechanics of materials to infer system state from a strategically located system of sensors. Intended to be built into a soft robot at the system level, a properly configured array of these deformation and pressure sensors can give state awareness far beyond that of individual sensors. The remainder of this paper is organized as follows: Section 3.2 presents the methods used,

beginning with a conceptual overview and review of beam theory/mechanics of materials on which these techniques are based, followed by design and fabrication, visual algorithms, and characterization methods. Section 3.3 presents results, divided into fiber-based deformation sensors, microfluidic pressure sensors, and color cell pressure sensors. Section 3.4 presents a discussion on the work and how it relates to the field. Where relevant, sections are further subdivided into fiber-based deformation sensor, integrated microfluidic pressure sensor, surface-mount pressure sensor, and color cell pressure sensor sections.

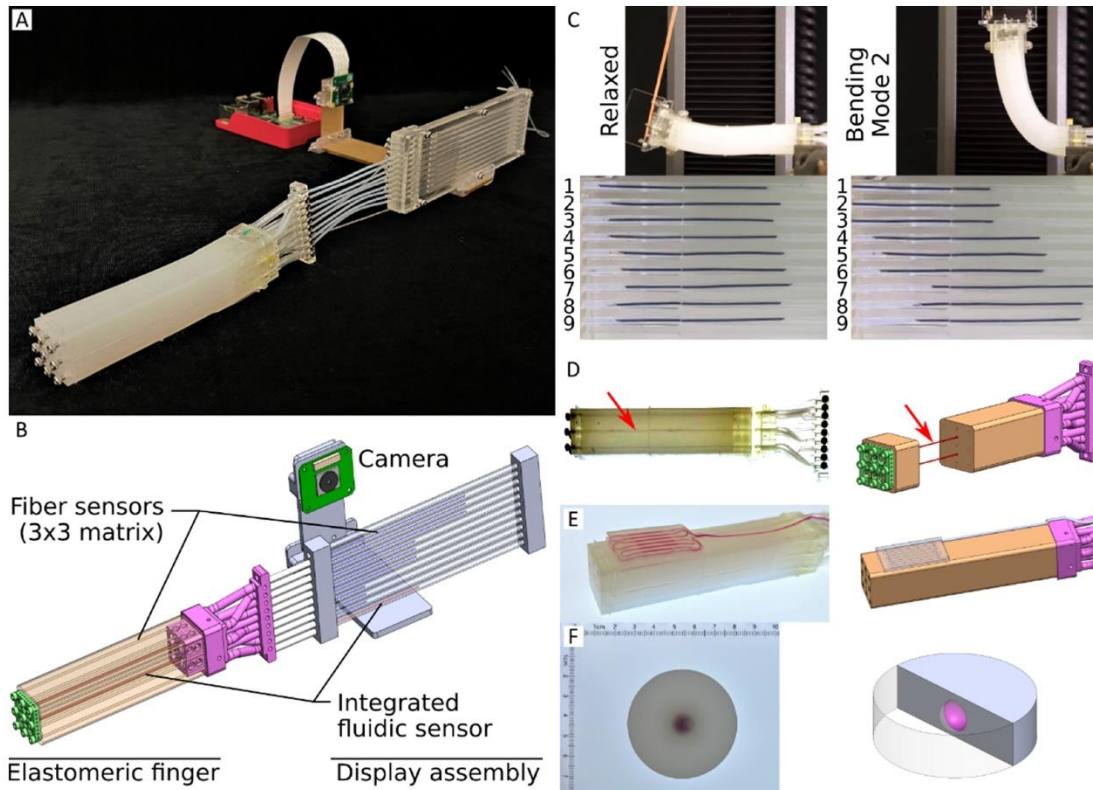


Figure 3.1: Soft sensors. (A). Elastomeric finger containing a microfluidic pressure sensor and nine fiber-based deformation sensors to sense pressure, bending, elongation, and twist. (B). Illustration of the elastomeric finger with fiber and fluidic sensors routed through the finger to a display assembly, where sensor positions are read by a digital camera. (C). Fiber-based deformation sensors, relaxed and bent states. Finger (top) and fiber states (bottom). (Stills from Video S1.) (D). Integrated microfluidic pressure sensor, senses overall pressure. (E). Surface-mount pressure sensor senses contact locally on the finger's surface. (F). Cephalopod-Chromatophore inspired color cell pressure sensor. External force causes the cell to change shape from spherical to a disk shape, changing disk diameter.

3.2 Method

We present an elastomeric finger containing nine fiber-based displacement sensors, one integrated microfluidic pressure sensor, and the ability to be configured with one or more surface-mounted microfluidic pressure sensors. These are all monitored with a single digital camera. Simultaneous analysis of these sensors allows us to determine the state of the finger. In the fiber-based deformation sensor method (Figure 3.1A–C), we embedded a 3×3 matrix of fiber-based displacement sensors into the elastomeric finger. Each displacement sensor is composed of two main parts: fiber and tube. The fiber is a flexible but inextensible/incompressible nylon fiber. The tube is a flexible elastomeric void built into the bulk matrix of the finger. Fibers are fixed at the distal end of the finger and routed through tubes along the length of the finger and out to a display assembly (Figure 3.1B). A short length (marker) of each fiber inside the display assembly is painted black. This contrasts with the white background allowing a digital camera to record the relative motion of the marker. When the elastomeric finger is distorted (bent, twisted, stretched), each tube changes shape and is stretched or compressed based on the overall mechanics of the mode of distortion. The fiber (free to slide along the length of the tube) slides within the display assembly, where the marker position and motion are recorded by a digital camera. This is similar to the Bowden cable assembly, which transmits force in many bicycle handbrakes. In our device, however, the passive sensor is distorted based on external actuation and used to sense displacement, the reverse of Bowden cables. Multiple cable-based sensors are embedded along the dorsal, ventral, and medial surfaces of the soft robotic sensor

(3×3 grid at the end of the finger in Figure 3.1A, B). Comparing relative motion between this grid of sensors allows differentiation between bending, stretching, and twisting.

From Euler-Bernoulli beam theory and classical mechanics of materials, we know that beams experience stress and tension/compression throughout their cross-sections based on the mode of the applied loading (bending, tension/compression, twist, combined loading) [112]. Here we briefly summarize some primary beam deformation modes (Figure 3.2A) with more detail on derivation in Appendix A. For a detailed analysis of beam theory or mechanics of materials, many excellent texts are available [112]–[115].

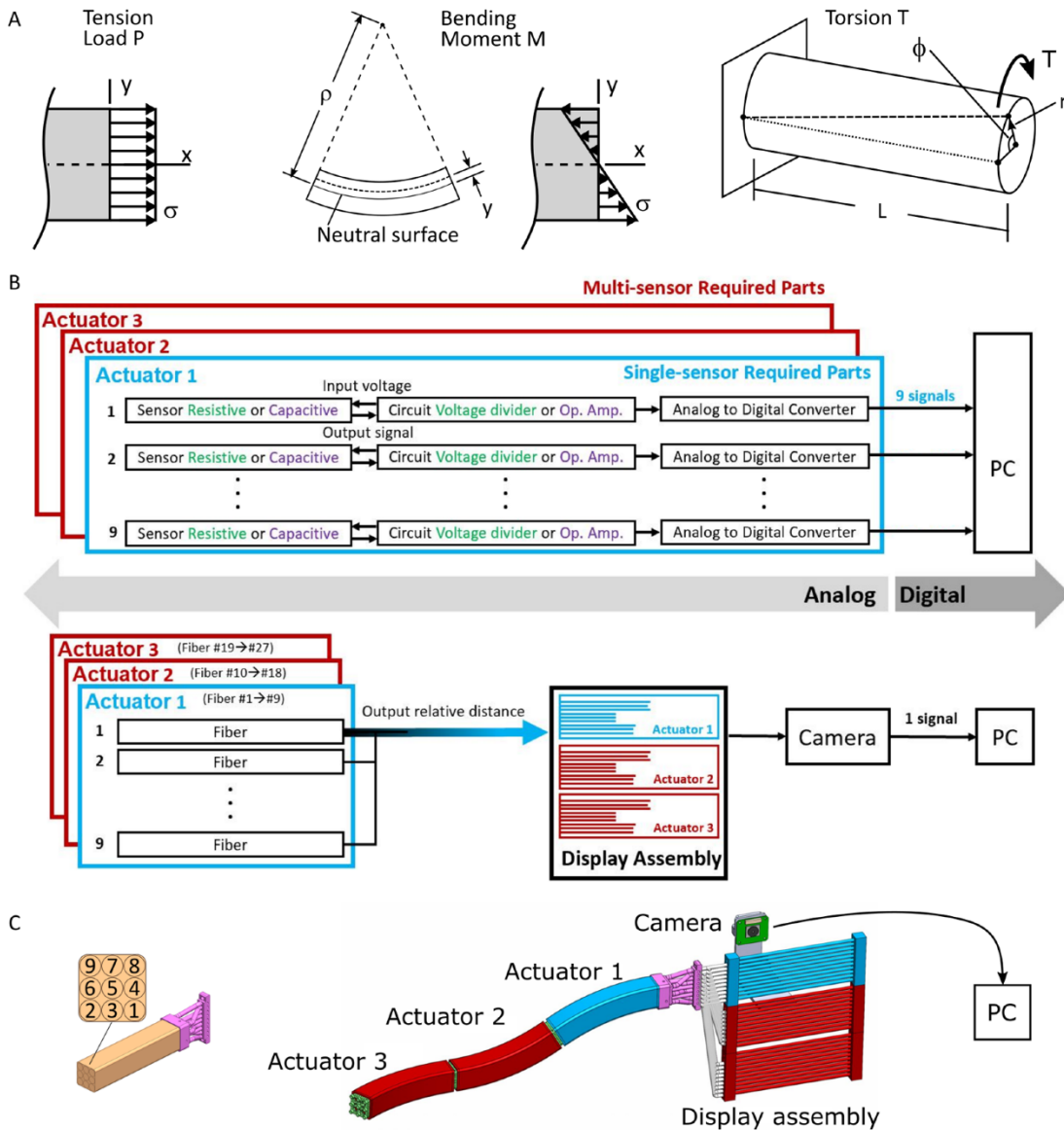


Figure 3.2: Fiber sensors, underlying concepts. (A). Mechanics of materials in elongation, bending, and twist. (B). Traditional vs. soft sensors. Traditional (top), each sensor requires separate electronics and support. Bottom, multiple fiber sensors all routed back to display assembly. One camera records all sensors. One actuator is indicated in blue. Two additional actuators are indicated in red. (C). CAD of assembly with the first (blue) actuator and two additional (red) actuators. Note, Camera records display assembly, not soft actuators, for reduced complexity motion capture of many sensors at once.

First, exploring simple elongation, we find that deformation is uniform across the cross-section and proportional to the load applied (Figure 3.2A). Deformation follows the equation,

$$\delta = \frac{PL}{AE} \quad (3.1)$$

where δ is total displacement, P is applied load, L is total beam length, A is cross-section area, and E is Young's Modulus.

In bending, material closer to the center of curvature (smaller bend radius) experiences compression, material farther from the center of curvature (larger bend radius) experiences tension, and material along with the neutral axis experiences neither tension nor compression. Within the linear elastic range, stress from bending (Figure 3.2A) follows the equation,

$$\sigma_x = -\frac{My}{I} \quad (3.2)$$

where σ_x is tensile or compressive stress, M is applied bending moment, y is the distance from the neutral surface (positive toward the center of curvature), and I is the second moment of inertia. The negative sign indicates compression toward the center of bending. Strain follows the equation,

$$\epsilon_x = -\frac{y}{\rho} \quad (3.3)$$

where ϵ_x is the strain in the beam axis, y is the distance from the neutral surface (positive toward the center of curvature), and ρ is the radius of curvature of the bent beam. The negative indicates shortening toward the center of curvature.

Shearing stress due to torsion (Figure 3.2A) follows the equation,

$$\tau = \frac{T\rho}{J} \quad (3.4)$$

where τ is shear stress, T is applied torque, ρ is the distance from the axis of rotation, and J is the polar moment of inertia. The angle of twist follows the equation,

$$\phi = \frac{TL}{JG} \quad (3.5)$$

where ϕ is the total twist of the beam, L is beam length, J is the polar moment of inertia, and G is the shear modulus. We can find the change in length of a line (linear initially, helical after twist) parallel to the axis of the beam, a distance r from the twist axis. Initially of length L , the line becomes a helix after the beam twists by an angle ϕ , about its central axis. The helix (former line, now helix) length is found from the formula,

$$L_{helix} = \sqrt{L^2 + (\phi r)^2} \quad (3.6)$$

where L_{helix} is the length of the helix, ϕ is the angle of twist found above, L is the beam length, and r is the distance from twist axis (see Appendix A for derivation). Thus, we find the change in length of a fiber parallel to the longitudinal axis as,

$$\Delta L = L_{helix} - L \quad (3.7)$$

Where ΔL is the change in length. With L and ϕ constant for any given beam and loading condition, we see that L_{helix} increases as r increases. Thus, the farther an element is from the axis of rotation, the more it will increase in length when experiencing a twist. Thus, fibers in the corners of a square cross-section will

experience more displacement than fibers at the center of the square faces, and a fiber at the center of the square face will not elongate at all.

While these formulae hold for beams within the linear elastic region, the principles (while not necessarily the magnitudes) remain true in the large deformation regime. See Appendix A for details on the mechanics of materials described here, further figures on bending modes, and sign conventions [112].

While each fiber sensor gives us local deformation information, the true value of these devices comes when used in groups. Thus, they must be readily integrated at scale without undue hardware requirements. Traditional sensors require individual hardware for each sensor (Figure 3.2B top). These fiber sensors, however, require only the passive fiber components and a single camera for all fibers (Figure 3.2B bottom). Then a single signal can be sent to the PC for video processing. Since video data consists of black markers moving horizontally across a white background, processing complexity is greatly reduced. For example, we select fiber sensors in the lower right and upper left corners of the finger (1 and 9 in front-view, Figure 3.2C). When the finger is bent upwards, 9 will indicate compression, but 1 will indicate tension. In elongation or twist, both will indicate tension. However, fibers 6 and 4 will indicate tension equal to 1 and 9 in extension, but less in twist. Expanding this example to the range of extension, bending, and twist scenarios, we configure a 3×3 matrix of fiber sensors, across the cross-section of the finger (as shown in Figure 3.2C). The combination of displacements allows us to interpret the deformation mode of the overall finger. For example, if the top three sensors are in compression, the middle

three show no deformation, and the bottom three show tension, we can infer that the finger is being bent upwards. Only primary deformation modes are presented here. Mixed-mode deformations (combinations such as bend and twist) are a fascinating option, but will require extensive further development. Sensor responses are qualitatively similar to theoretical beam bending results, but in large deformation, it is likely that some deviation from theory will be seen. In mixed mode deformation, it is likely that an assumption of linearity will no longer be possible (thus excluding superposition for state assumption). Thus future work using machine learning methods such as Artificial Neural Networks will be necessary along with the soft robotic developments described here. We present offline marker tracking and characterization of these sensors in the deformation modes discussed above, as well as real-time marker tracking, which we envision as a path toward real-time control of soft robot actuators.

In the integrated microfluidic pressure sensor method (Figure 3.1D), we embed microfluidic channels into the elastomeric finger to sense the overall pressure exerted on the finger. This sensor consists of a sensing part and a transmission part, both filled with colored liquid. The sensing part is compressible and embedded along the length of the square column-shaped elastomeric finger. The transmission part consists of a flexible, incompressible tube routed through the display assembly. When force is applied to the sensing part, the chamber is compressed, reducing the volume of the sensor part. This forces the incompressible colored liquid out of the sensing part, through the transmission part, and across a display tube in the display assembly.

We also present a surface-mount pressure sensor (Figure 3.1E), which can be bonded (singularly or in batches) to the surface of the finger or any similar elastomeric device. This pressure sensor can be installed at any location on a multitude of elastomeric actuators and robotic systems. We present characterization data on one sensor to demonstrate its utility, not an exhaustive study of possible configuration or applications. Both microfluidic methods transmit to the same display assembly used to record fiber position; thus, a single digital camera can capture data from fiber-based deformation sensors as well as microfluidic pressure sensors. The configuration we present records 11 sensors (nine fiber, one integrated microfluidic, and one surface mount microfluidic) captured by one digital camera, as that was sufficient for this proof of concept. An effort to minimize scale could greatly increase the number of discrete sensors possible with one camera.

Lastly, we present a color cell pressure sensor inspired by chromatophores in cephalopods [106]. Rather than mimicking this clever technique, we draw upon it for our inspiration [116] and flip the application from active modulation for camouflage to a passive sensor. Spherical cells of colored liquid are embedded in an elastomeric substrate. When the substrate undergoes external pressure, local deformation causes the spherical cells to deform and become disk-like. Viewed from an axis normal to the disk plane, this causes the disks to appear larger than the original spheres. Thus, the applied force can be determined from the diameter of the disk.

3.2.1 Design and Fabrication

Fiber-based deformation sensor: (Since the elastomeric finger is fabricated as one device, the integrated microfluidic pressure sensor will be described in this section) Similar in concept to many soft robots, we fabricate our square column-shaped soft sensor (elastomeric finger) using multiple molding steps. The fabrication process is summarized in Figure 3.3A, with a detailed description in Appendix C. The assembly is fabricated using three molding steps and a final integration step. Mold 1. We used three plastic bars (diameter 0.9 mm) to create the center cable chamber and two microfluidic chambers. The matrix material of the finger is a readily available elastomer, Ecoflex 00-30 (Smooth-On, Inc. Macungie, PA, USA) in molds printed from a 3D Printer (Form 3, Formlabs, Somerville, MA, USA). Mold 2. Retaining the center plastic bar in the mold, we demolded the two other plastic bars. We used the silicon tube (inner diameter 0.5 mm, outer diameter 1 mm) to connect the microfluidic chambers on the top holes and extend the bottom holes. Then, we attached the top carrier to the center plastic bar and aligned it with the other eight plastic bars into the second mold. The top carrier embedded in the soft sensor provides a surface to fix the cables. Mold 3. We demolded the soft sensor from the second mold, keeping all the plastic bars and two silicon tubes inside the sensor, and then aligned them to the base holder. After alignment, we secured it into the final mold and connected the finger to the solid base holder once it cures. Integration. We inserted the high-strength fiber cables (Monofilament nylon thread, diameter 0.5 mm) into the soft sensor chambers,

fixed them using screws on the top carrier, and injected the colored liquid into the microfluidic chambers.

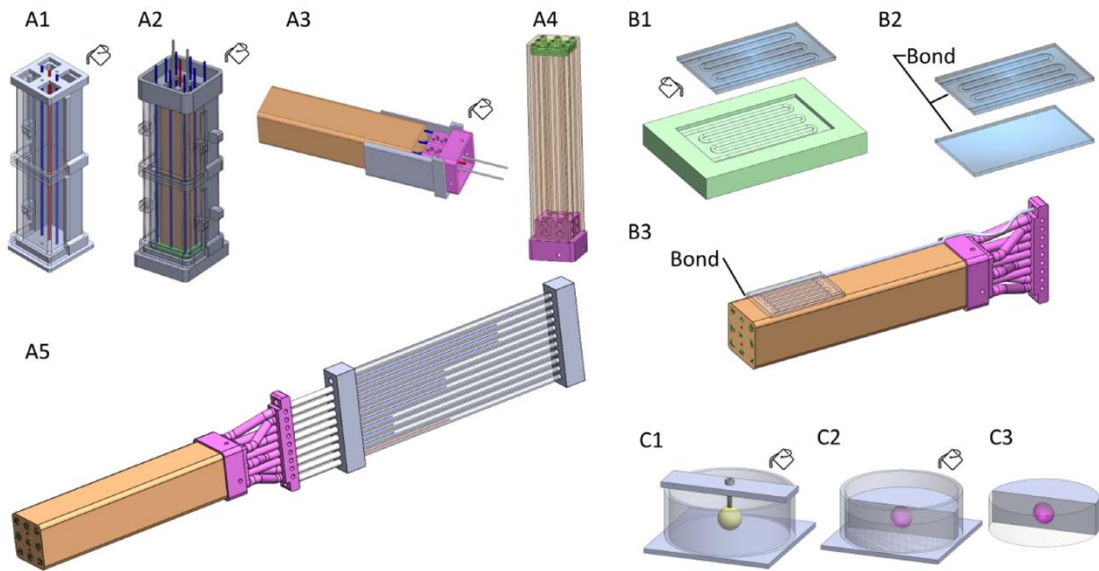


Figure 3.3: Fabrication. (A). Elastomeric finger containing fiber-based displacement sensor and integrated fluid pressure sensors. (A1–A3). An elastomeric finger is fabricated in three mold steps, containing channels for the nine fiber sensors and an integrated fluid pressure sensor. Molds are shown in gray. (A4). Finished elastomeric finger, transparent representation to illustrate internal vasculature. (A5). A finger is instrumented with fibers and integrated with the display assembly. (B). Surface mount liquid pressure sensor is molded (B1), bonded to a base layer (B2), then bonded to an elastomeric finger, and infilled with colored water (B3). (C). Chromatophore cell is molded into an elastomeric substrate and infilled with colored water (C1), then sealed with elastomer (C2), yielding a final sensor (C3).

Microfluidic pressure sensor: The design of the integrated microfluidic pressure sensor is described above, in the Fiber-based pressure sensor section, because it must be fabricated concurrently into one integrated unit. We present the integrated pressure

sensor in the finger motif; it can, however, be designed into most actuator systems that use a matrix of molded elastomer. While this integrated sensor provides useful overall pressure of the soft finger, we developed a surface-mount microfluidic pressure sensor to expand sensing capabilities (Figure 3.3B). Similar in form to several existing surface-mount sensors, our technique uses the displacement of liquid rather than change in resistance in an ionogel [18], [32], or liquid metal [62]. This surface-mount pressure sensor is similar in concept to a microfluidic embodiment of the Skinflow work by Hauser, Rossiter, et al. [117]. This surface mount sensor can be fabricated from elastomers of various durometers in different thicknesses to modulate sensitivity, and it can be mounted (singly or in groups) at various locations along with the elastomeric finger or other actuators. Fluid displacement data can be interpreted in the same camera frame as the fiber-based actuator described above, thus expanding the sensing modes possible with this overall vision-based system.

Color cell pressure sensor: The final sensor technology presented here derives its inspiration from the chromatophores used by many cephalopods and some other animals to change their color and appearance. Chromatophore cells filled with pigment appear as small dark dots. To change perceived color, radial muscle fibers stretch the chromatophore cell from roughly spherical to a wide-thin disk shape of the same volume. Thus, when viewed from an axis normal to the disk-plane, the appearance changes from a small, dark dot in a near-transparent matrix to a larger colored disk. An array of these chromatophores in various colors allows the animal to present a variety of appearances. While cephalopods use their chromatophore cells to actively modulate

their appearance, we invert this technique, using passive cells as sensors. Fabricated into an elastomeric matrix, external pressure causes these spherical cells to deform into disks in a plane normal to the applied force. When viewed from an axis normal to the disk plane, the diameter of the disk increases with applied force.

3.2.2 Vision Algorithms

An algorithm was designed to process two different possible image stream inputs: a real-time camera stream or a previously recorded video. For the real-time processing, we used a video stream from a Raspberry Pi Camera Module 2, with the constraint of the camera being aligned such that the painted filaments are approximately parallel to the horizontal axis. The videos recorded on a separate device were filmed with the same constraint. To address alignment issues across multiple runs, boundaries are digitally positioned around each of the channels with the filaments in the camera frame (current frame for live stream, first frame for recorded videos) before beginning the algorithm.

The OpenCV Python library for image processing is used to facilitate detection in each frame. Each frame is first cropped to include only the boundaries and then converted to be in grayscale to accentuate differences in light and dark colors and to eliminate possible noise from reflection. Every pixel value within the frame is then scaled up to further accentuate the difference between the white background and the black filaments. The Canny edge detector algorithm is then used to determine the edges of the filaments, and the Hough Lines Probability algorithm returns the start and end

point pixel coordinates of each line edge. The algorithm then iterates over each detected line, and the endpoint furthest to the right within each boundary is recorded as a pixel location in a CSV. Further details are presented in Appendix B.

3.2.3 Sensor Characterization

We evaluated the elastomeric finger containing fiber-based displacement sensors and fluid-based pressure sensor in each actuation mode individually, with the understanding that mixed-mode sensing (elongation and twist combined, or bending along a non-primary axis) will be the goal of future development using the real-time vision algorithms described in Section 3.2.2. For the fiber-based sensor, separate characterization fixtures were employed for each mode of evaluation (bending, elongation, twist) as shown in Figure 3.4A, each mounted to an Instron 5943 tensile tester (Instron Co., Norwood, MA, USA). The same apparatus was used for bending 1 and bending 2, offset by 90° as illustrated in Figure 3.4A–E. Integrated microfluidic pressure sensor characterization (Figure 3.4F) and surface mount microfluidic pressure sensor characterization (Figure 3.4G) were performed on the same fixture, and chromatophore-inspired sensor characterization (Figure 3.4H, I) was performed on a separate fixture. Each test was performed four times to monitor repeatability.

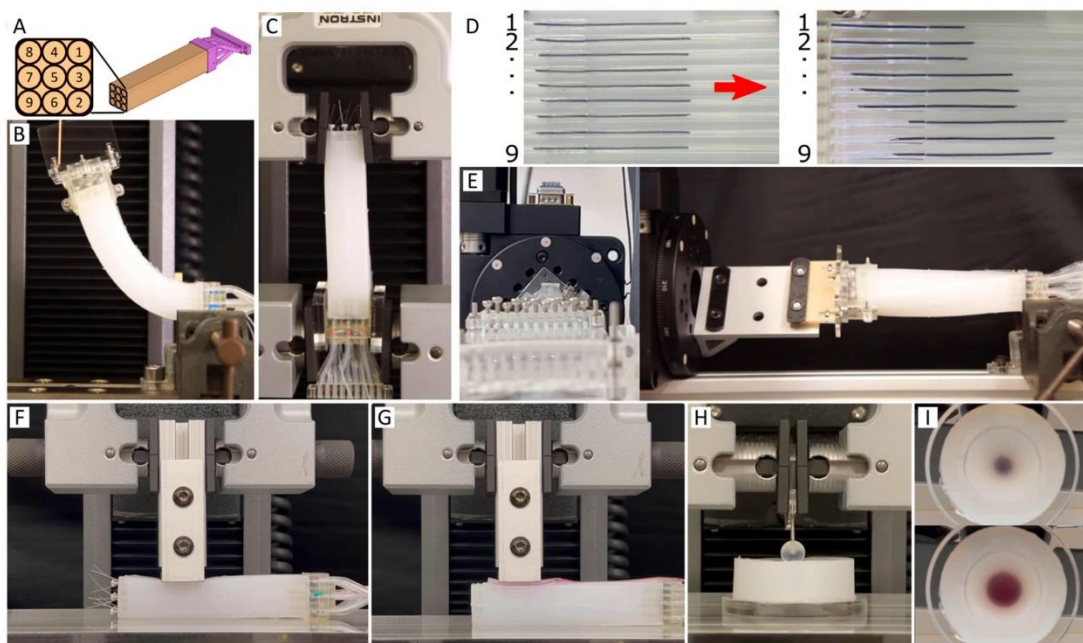


Figure 3.4: Test fixtures. (A–E) fiber-based displacement sensors, (F–I) fluid-based pressure sensors (A). Fiber sensor configuration. (B). Bend test setup. Elastomeric finger mounted horizontally, pulled from neutral to deformed (bent) state. (C). Elongation. Finger mounted vertically, top-end pulled vertically. (D). Fibers in the display assembly. Left neutral state, right when deformed (shown in bend direction 2). (E). Finger mounted horizontally, twisted along its axis (shown in two views). (F). Integrated fluidic pressure sensor undergoing compression. (G). Surface-mount fluidic pressure sensor undergoing compression. (H). Chromatophore inspired pressure sensor undergoing compression. (I). Chromatophore sensor deflecting under pressure.

3.3 Results

Data is divided into fiber-based deformation sensors, (estimating soft finger displacement) and fluid-based pressure sensors (microfluidic and color cells). Fiber-based sensor characterization investigates displacement of a 3×3 grid of fibers as described in the Methods section. Figure 3.5 presents fiber responses to displacement in two modes of bending (offset by 90°), extension, and twist (See also Supplementary

Videos S1 and S2). Finger orientation and resulting fiber locations within the finger are shown in the illustration to the left of each graph. To achieve two modes of bending, the finger is rotated inside the mounting fixture 90° between Bending 1 and Bending 2, yielding a different fiber orientation. Fiber orientation for elongation and twist is also shown, but because these displacements are along the longitudinal axis, orientation does not affect results.

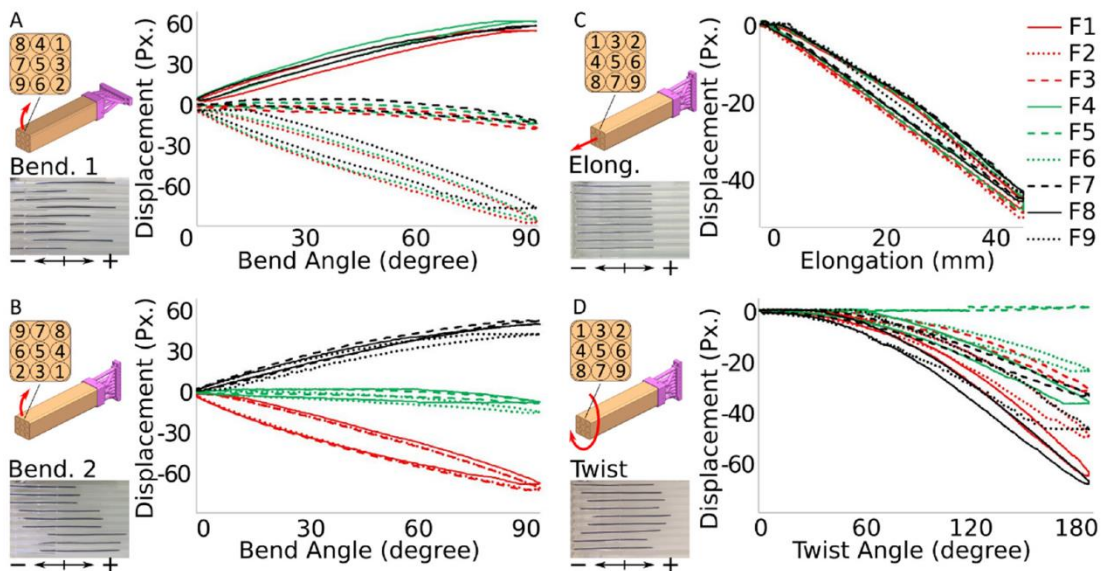


Figure 3.5: Results, fiber sensor marker displacement (pixels). Fiber configuration is shown in the upper left of each subfigure. Sample images of marker displacements are shown in the lower left of each subfigure (1 top... 9 bottom). (A). Bending direction 1. (B). Bending direction 2. (C). Elongation. (D). Twisting. Legend for all graphs, Fiber 1–9 shown in the upper right (near subfigure (C)).

3.3.1 Fiber-Based Deformation Sensor

As the elastomeric finger undergoes displacement in the described mode, material distorts locally, consistent with theory from classical mechanics of materials (Appendix A). Fibers, attached at the distal end of the elastomeric finger are free to move inside their respective tubes (described in Section 3.1, Section 3.2), thus they do not elongate or compress. Rather they move along their tube and back through the display assembly. Thus, when the finger undergoes Bending direction 1 (Figure 3.5A), the top portion of the finger undergoes compression, the bottom undergoes tension, and the midplane sees little tension or compression. With the fiber configuration shown in Figure 3.5A, Bending 1 should cause the uppermost fibers to move farther into the display assembly (positive direction). The lower fibers should move out of the display assembly (negative direction), and fibers in the midplane should move very little at all. The graph in Figure 3.5A verifies this. Solid lines (fiber 1, 4, 8) are positive, dotted lines (fibers 2, 6, 9) are negative, and dashed lines (fiber 3, 5, 7) moved little at all. Due to the test setup (distal end of finger pulled upward and allowed to move laterally), some tension in the finger caused the midplane to stretch slightly, causing slight negative values in dashed lines.

When the finger was rotated 90° and Bending direction 2 was investigated (Figure 3.5B), similar results were seen for fibers based on the new orientation. In this configuration again, black lines (fibers 7, 8, 9) were those along the top edge of the finger, where the finger was in compression. These fibers moved into the display

assembly (positive displacement). Similarly, red lines (fibers 1, 2, 3) were pulled out of the assembly, green lines (fibers 4, 5, 6) were little affected.

Tests in elongation (Figure 3.5C) were also as expected. As the elastomeric finger was elongated, all fibers move out of the display assembly, recorded as negative displacement. Experiments in twist (Figure 3.5D) also showed results consistent with classical mechanics of materials. Fibers at the corners, farthest radially from the central axis (fibers 1, 2, 8, 9) exhibited the most deformation, pulling the fibers out of the display assembly for negative displacement. Fibers along the flat of each surface (fibers 3, 4, 6, 7), closer to the neutral axis, exhibited less deformation, recorded as less-negative displacement. Finally, fiber 5 at the neutral axis exhibited almost no displacement at all.

3.3.2 Source of Hysteresis

One may initially be concerned with the hysteresis loop (actuation path does not overlay with release path, but instead creates a loop in bend angle, elongation, or twist vs. fiber displacement). If this were due to the internal properties of the fiber sensors, it would not negate the value of the sensing system, but it should be addressed. Analyzing still frames from our motion capture videos indicates that the actuation and release paths of the elastomeric finger do not trace out a similar path. In other words, the shape of the elastomeric finger is different at a given angle in the actuation ($0^\circ \rightarrow 90^\circ$) path than in the release ($90^\circ \rightarrow 0^\circ$) path. Thus, it would be expected that the fibers

sense different finger geometry based on the path. See Supplementary Video S4 for dynamic illustration overlaying actuation vs. release geometry.

3.3.3 Microfluidic Pressure Sensors

The elastomeric finger is configured with an integrated microfluidic pressure sensor along its entire length. Consisting of a liquid-filled microfluidic channel, this sensor is intended to sense the overall pressure state in the elastomeric finger. Thus, repeatability and range are highly desirable. Maximizing sensitivity (ability to perceive a light touch) is not required for this sensor. Figure 3.6A shows a very repeatable and linear response to forces up to eight Newton, with no sign of signal saturation (change in geometry precludes perception of increased applied load) over four trials. Figure 3.6B shows the sensor response of a surface-mounted pressure sensor over four trials. Such a sensor would be attached to the surface of the elastomeric finger to sense a desired (or undesired) contact at a particular location on the finger surface. Thus, for such a sensor, linearity and maximum force before saturation are not primary concerns. Rather, for this sensor, the ability to detect contact is of primary interest. While this sensor is shown to saturate with an applied force below four Newton, saturation is of little concern once contact is detected.

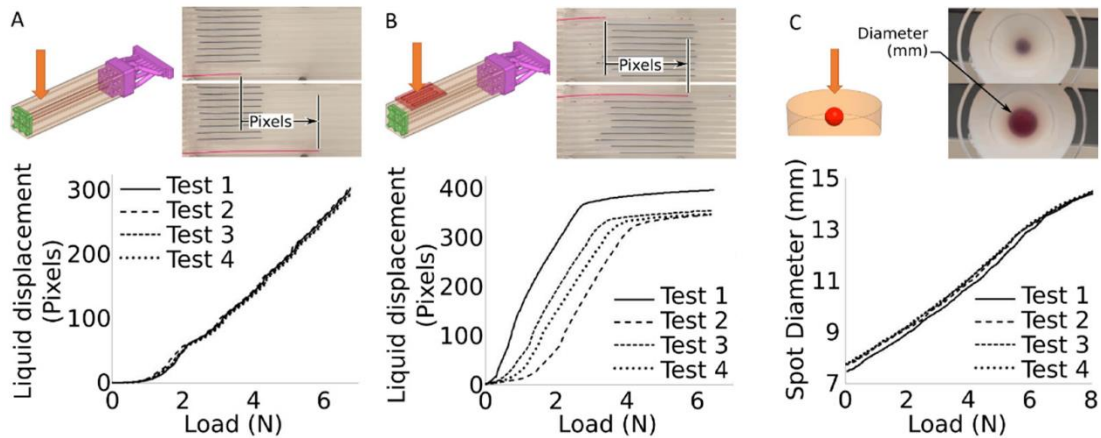


Figure 3.6: Results, microfluidic pressure sensors. (A). Integrated microfluidic sensor. An elastomeric finger is shown under an externally applied load. The graph shows displacement of fluid in display assembly (red line in inset still from Video S2) vs. force applied on an elastomeric finger with an embedded sensor. (B). Surface-mount microfluidic pressure sensor. The graph shows displacement of fluid in display assembly vs. force applied directly to the surface-mount sensor. (C). Chromatophore inspired sensor. The graph shows the diameter of a fluid cell (shown as stills from Video S2) vs. externally applied load.

Finally, Figure 3.6C presents the behavior of the chromatophore-inspired fluidic pressure sensor. At applied loads, up to eight Newton, the radial expansion of the liquid cell is relatively repeatable and very linear. The technique has been demonstrated here using one liquid cell, but the technique could be expanded to any number of cells at varying depths, colors, and volumes to achieve a multitude of responses to pressure.

3.4 Discussion

We presented vision-based methods of sensing deformation and pressure in soft robots, each including only passive components inside the soft robot. First, we

presented a fiber-based deformation sensor wherein local material displacement in a soft robot was transmitted to a remote display assembly and tracked by a digital camera. Next, we presented two fluidic sensors, wherein a pressure in a soft robot displaces liquid inside a microfluidic channel, which was transmitted back to the aforementioned display assembly. We presented an integrated microfluidic pressure sensor, by which the overall pressure state inside the body of a soft robot is tracked. Next, we presented a surface-mount pressure sensor to track contacts locally on the surface of a soft robot. Finally, we presented a color-cell pressure sensor. With this sensor, we flip the idea of a chromatophore (with which cephalopods actively stretch color cells from spheres into disks to modulate appearance for camouflage and other applications). In our application, the passive spherical color cell is embedded in an elastomeric matrix. When an external force is applied to the elastomer, the color cell is compressed in the direction normal to the force, expanding it radially. We characterized the radial expansion vs. applied force for one sample configuration.

We presented an elastomeric finger with nine embedded fiber deformation sensors, one integrated pressure sensor, and one surface-mounted pressure sensor. We characterized the fiber sensors in two orthogonal directions of bending, twist about the finger's primary axis, and extension. All modes of deformation followed the responses expected from by mechanics of materials and beam theory. The integrated microfluidic pressure sensor demonstrated a highly repeatable response to externally applied pressure with no saturation detected at 7N externally applied force. The surface-mounted pressure sensor (to sense contact locally) sensed much smaller applied forces

(0.05–0.3 N) but saturated when as little as 2N force was applied. As a contact sensor, early detection is more useful than high saturation levels. These encouraging results on a single elastomeric finger will provide a foundation upon which sensorized actuators will be developed based on actuator designs from our previous work [18], [86].

While the very simple sensor designs presented here have value individually, the key contribution of this work is that the sensors are fundamentally designed to be used in groups. Intended to be designed into a soft robot at the system level, a properly configured array of these deformation and pressure sensors can give state awareness far beyond that of individual sensors. Most sensors used in soft robots (and many sensors in general) vary in resistance or capacitance in response to a change in a physical parameter such as length, bend angle, or contact pressure. Each sensor requires wiring, electronic circuitry, and a dedicated input to a data acquisition system before the resulting signal is sent to a computer. Five sensors require five times the infrastructure. With our presented method, a digital camera records the movement of markers on fiber sensors and colored liquid in microfluidic channels. Thus, dozens of markers and fluid channels can be monitored almost as easily as one. Other camera-based soft robot state-estimation systems exist, but they primarily record the pose of the robot directly, thus requiring specific lighting conditions, unobstructed line-of-sight access to all parts of the robot.

The elastomeric finger we presented used nine fiber sensors to determine its pose and two fluidic sensors to determine overall and local pressure states. By configuring fibers in a 3×3 matrix, we used the theories put forth in classical

Mechanics of Materials (See Appendix A) to determine pose during states of bending in both primary planes, twist about the primary axis, and elongation along the primary axis. While the presented work was on a finger designed specifically to illustrate adherence to classical mechanics of materials theory, this state estimation could be applied to a range of soft actuators and soft robots in general. As stated above, we plan to use this technique in an actuator design similar to our previous soft finger [18], [86] with a roughly square cross-section. These fiber and fluidic sensors could be used in many soft robots with actuators having rectangular, round, or trapezoidal cross-sections, requiring sensors to be placed at based on beam theory for that cross-section. With their innate under-actuation and deformability, defining the pose of a soft robot with reasonable accuracy requires far more sensors than do traditional robots. One can readily imagine a soft robot requiring nine sensors (3×3 matrix) for EACH actuator to estimate its pose. Thus, a three-fingered gripper would require 27 sensors, a simple quadruped would require 36, and a more complex robot would require many more. The circuitry and wiring required for this many discrete electrical sensors would quickly become burdensome. With our method, passive sensors are all routed back to one central display assembly and recorded by one digital camera. While we present 11 sensors in the display assembly, this number was chosen as it was the number required to characterize the soft finger (nine deformation and two pressure sensors). With our method, any upgrading (to increase sampling frequency or resolution) would be contained to the camera system, while upgrading dozens of electrical sensors would also be a sizeable task. With our method, many fibers could be routed back to one

remote display assembly, where a single digital camera could track the motion of all markers in a controlled environment, optimally lit for contrast and marker tracking.

Chapter 4

Bioinspired Soft Finger with Multi-Curvature

Locking Modules

4.1 Introduction

Over the past decade, typical robotic tasks have expanded away from largely repetitive operations in fixed surroundings and toward tasks in a range of unusual settings. In addition, in many automated tasks, human-robot interaction will become the norm [118], [119]. Therefore, existing traditional robots made of rigid components require more complex controls, and they do not adapt quickly to atypical environments. Furthermore, due to safety concerns, they are challenging to deploy in circumstances when human-robot interaction is essential. Alternative robots built of soft compliant materials are currently being researched as a solution to this challenge.

Soft robotics is constructed of soft materials, having Young's moduli that are lower than those of human muscles [120]; unlike traditional robot motors, the driving method of soft robots depends mainly on the materials used. From the way of actuating, it can be divided into the following categories: air pressure [2], [86], tendon-driven [41], electromagnetic field [53], chemical reaction [17], thermal reaction [121], [122].

Among them, the soft robotic grippers are the most studied and are one of the earliest industrial applications, such as food packaging [123], agricultural product, confectionery, and bakery industries because their products are soft and fragile. Traditional mechanical grippers are made of steel linkages consisting of a limited number of degrees of freedom (DOF), mostly driven by electric motors, with multiple sets of sensors in each degree of freedom. They also require more control modules and must know precisely the shape and position of the object in order to avoid damaging it, so their use is limited to specific types of objects. If various objects need to be manipulated, it would be very difficult to grasp them with the same rigid gripper.

The soft gripper is different from the traditional mechanical gripper; most of them are pneumatic driven and have a fast response time [2], [86]. Flexible materials (low Young's modulus) are often used for the gripper, which makes them lighter and cost-effective [86], and it gives it nearly infinite DOF to adapt to the shape of the object being gripped. It is not necessary to know exactly the shape and position of the object when gripping it; just keep the gripper close enough to the object to grasp it smoothly. The soft gripper is relatively easier to control because it does not have a complex sensor and does not request feedback control to complete the task. Thus, most tasks are completed open-loop or with external visual control only. Robust closed-loop position and force control remain challenges in the field of soft robotics [28], [124], [125].

However, due to the inherent compliance of soft grippers, soft robots are unable to grip heavy objects like conventional grippers [28]. In recent years, researchers have proposed to solve this problem by changing the stiffness of the gripper (variable

stiffness) to improve its gripping ability [86], [126]. One of the methods is the jamming structure, which performs relatively well because of its fast response time and simple structure. The principle behind this is a structural phenomenon in which a laminar structure of compliant strips becomes strongly coupled through friction when a pressure gradient is applied, resulting in a dramatic change in mechanical properties. We can roughly divide the jamming structure into three types: Grains, Fibers, and Layers [74]–[76].

Granular jamming [76] is composed of a large number of "granules," approximating points or zero dimension particles enclosed in an elastomeric membrane. This is the most deformable system, and it can handle relatively large compression forces from any direction. Approximating zero-dimension points, granules are free to move in any direction, limited only by interaction with other granules or the elastomeric membrane. This jamming structure requires more volume when applied with soft robotics, and it is heavier than the other structures. Layer jamming [74] and fiber jamming requires less volume and are relatively stable than granular jamming. The structures of layer jamming and fiber jamming are made of non-fluidic planar sheets or fibers. Under this structure, it's easier to maintain the shape of the structure when switching mode between non-jamming and jamming states than granular jamming. Layer jamming is excellent to support tension force parallel to the jamming layer. Fiber jamming [75] is the latest development method, and its structure is the lightest of the three. The structure consists of long and slender elements, approximating one-

dimensional elements, able to bend freely but not able to elongate. Thus this structure exhibits good performance in the tension and compression force.

The integration of jamming and soft robotic applications has opened up a new field of hybridization, and we can no longer simply classify it as soft or rigid by dichotomy. Thus, we introduce the term **Hybrid Gripper**, which we define as a robotic gripper combining inherently soft components with components which exhibit high stiffness some or all of the time. This stiffness can come from inherently stiff materials such as engineering plastics and metals, or the stiffness can come from jamming, phase change, or other means of stiffness modulation. Table 4.1 compares the capacities of various types of soft–rigid hybrid grippers established to date in terms of actuating method, force direction controllability, multiple curvatures, and gripping force capabilities.

Table 4.1 Comparison of soft–rigid hybrid grippers characteristics.

Author	Actuator	Hybrid Structure	Force direction controllability	Multiple Curvatures	Gripping force capabilities	Operation Time
Yang Yang[83]	Pneumatic	Grains and Layers Jamming	N/A	○	High	Fast
Keng-yu Lin[86]	Pneumatic	Layer Jamming	X	X	High	Fast
Wei Wang[127]	Thermal	Shape Memory Polymer (SMP)	X	○	Low	Slow
Wookeun Park[128]	Pneumatic	Rigid Structure	X	X	High	Fast
Yufei Hao[129]	Pneumatic	Low-Melting-Point Alloy	X	X	High	Fast
Sun Tao[130]	Pneumatic	Self-locking Adjustable Joint	X	X	High	Fast
Zaryab Shahid[126]	Thermal	Stiffness	X	○	Medium	Slow
Raymond R. Ma[21]	Tendon	Soft joints	X	X	High	Fast
This Study	Pneumatic & Tendon	Chain-shape Locking Module	○	○	Very High	Fast

Here, ○ indicates Yes, and X indicates No.

Here we first explain the meaning of **force direction controllability**. We define that the gripper is said to have force direction controllability if it can actively apply force in a given direction like a force vector, as shown in Figure 4.1. When we want to apply force to an object with the finger facing the direction of the blue arrow, we can set the locking module of the finger to the corresponding state so that the finger can move in the direction of our task to apply force to the object. In table 4.1, we can see that most of the soft–rigid hybrid grippers do not have force direction controllability. This is because most of the hybrid structures are continuously connected and embedded in the soft gripper [86], [128]–[130]. There is no segmentation between the structures, so there is no way to achieve segmented control of stiffness. This means that the gripper

curvature can only rely on the soft actuator's bending movement, making it impossible to achieve force direction control.

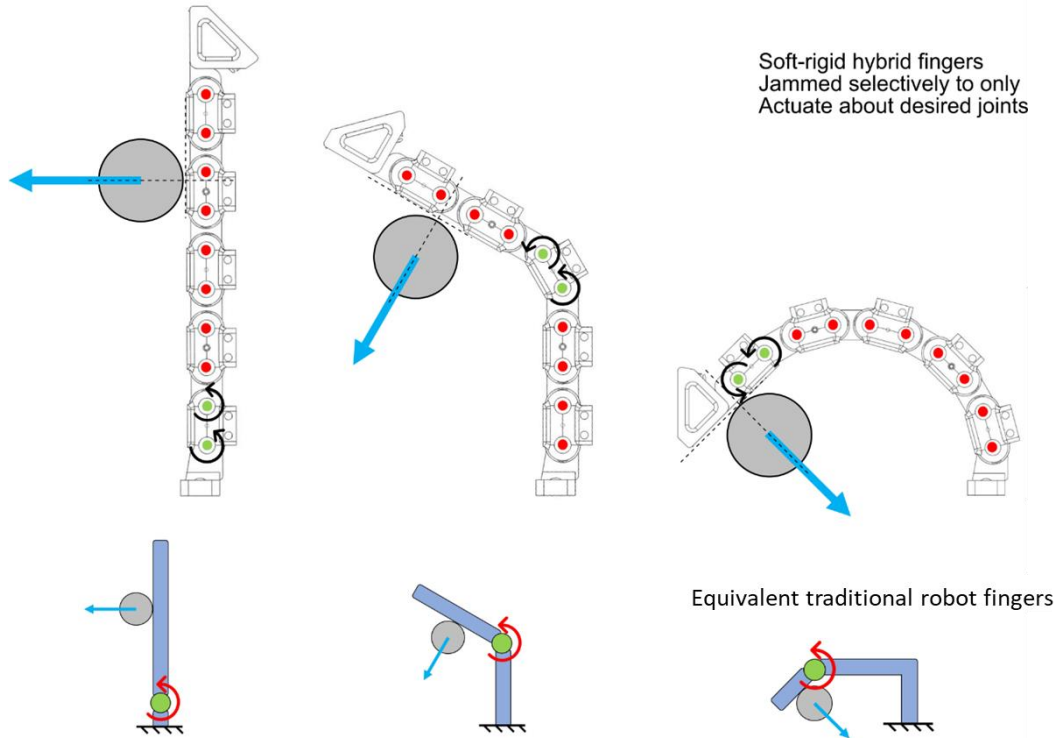


Figure 4.1: Illustration of force direction controllability with state corresponding to locking modules. The Blue arrow indicates the targeted force direction; the red dot indicates the joint is locked, and the green dot indicates the joint is unlocked and rotated freely.

Overall, the difference in actuator directly affects the gripping force capabilities and operation time. The pneumatically driven grippers have the fastest gripping operation time compared to the tendon and thermal driven. The tendon-driven gripping force is the highest, and the pneumatic driven is the second and depends on the air pressure used. At the same time, the design of the hybrid structure will affect the force direction controllability and multiple curvatures. We define **Multiple Curvatures** as

the ability of a robotic finger to bend at multiple locations along its length. Most soft fingers actuate at multiple locations or continually along their length, but to exhibit multiple curvatures, our definition requires an ability to control/select the location of this curving, which basically requires a segmented variable stiffness structure. With the multiple curvatures feature, it is possible to work with the actuator to achieve the active application of force in the specified direction.

Three types of force in our soft robots are pneumatic-driven, tendon-driven, and jamming. The **pneumatic** actuating force is that converts energy typically in the form of compressed air into mechanical motion. It can also apply a distributed force, which is back drivable in case the force gets too high. This is a common mode of actuation seen in soft robots, including our previous work [18], [33], [86]. The use of **jamming** does not directly apply force from the finger to an external object. Instead, it locks the finger in place once it is already in the desired configuration, as described in the jamming section. The benefit of jamming is that once the gripper has cradled the object and before lifting it, we can lock the fingers in place to securely enclose the object (or otherwise provide sufficient support) to securely move it. This will be good for lifting the object that has already been grasped using pneumatic actuation. However, this would not be suitable for applying a directed load like pulling the trigger of a squirt bottle. In our design, when the locking modules are locked, they become a stiff member, but the finger cannot apply a high force using only a pneumatic actuator. And so for that, we add a **tendon-driven** actuator, which can apply high force similar to the Bowden cable in the bicycle, giving our finger greatly increased force capability.

Although the soft–rigid hybrid structure improves the gripping force, this force is a relatively static force. Its principle is to make the gripper, after grabbing the object changes its rigidity to support the weight of the object, or it can passively resist the external force, so the single hybrid structure still has limitations.

In this paper, we present a bioinspired soft finger with a soft-rigid hybrid structure that can have a multi-curvature and force direction controllability to provide force in a specific direction. By connecting multiple independent locking modules into a chain-like system, their soft and rigid states can be controlled independently. To enhance its flexibility, we use two actuation methods to drive the finger, which allows the bioinspired soft finger to grasp objects of various shapes, sizes, and weights quickly and stably while providing sufficient force in specific directions. In addition, we have added a nail mechanism on the tip, which allows the finger to assist in gripping flat or tiny objects.

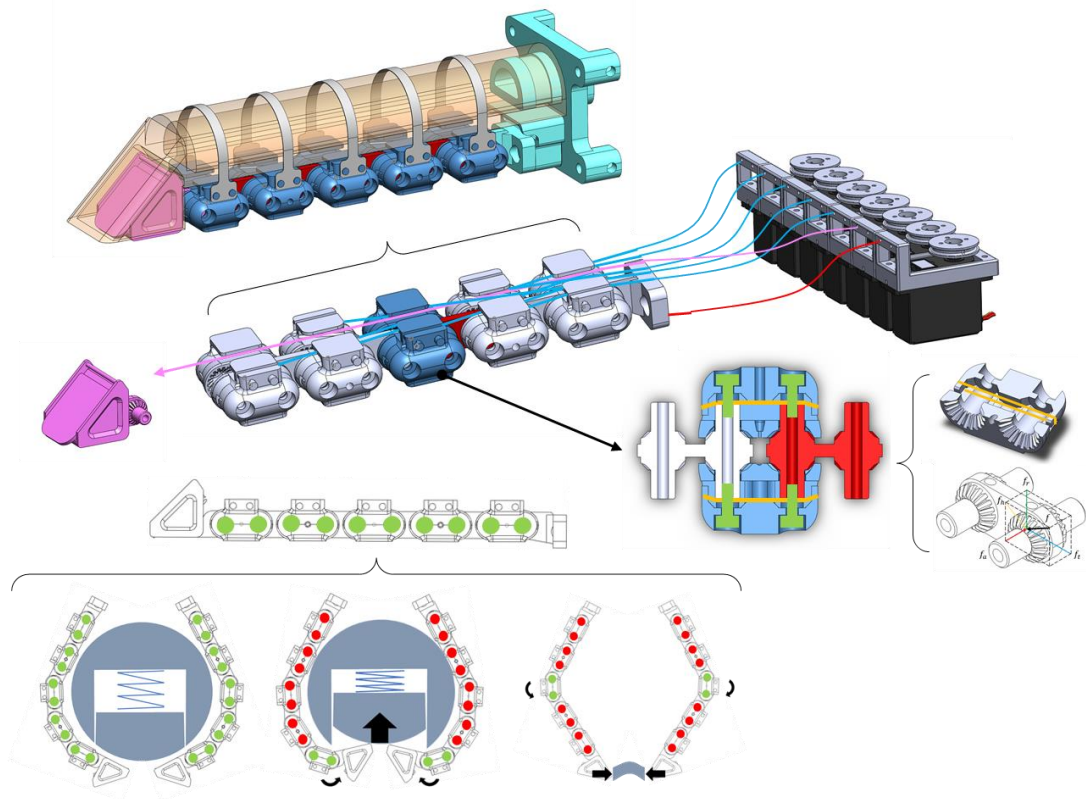


Figure 4.2: Overview of the bioinspired finger system.

The main contribution of this work is to propose a new soft-rigid hybrid structure design and a method of interaction between pneumatic and tendon-driven actuators. The newly developed segmented controllable soft-rigid module combines the advantages of a soft robotic finger and a rigid mechanical finger with the ability to provide force in a specific direction. We have performed a modeling analysis of this controlled soft-rigid module, which provides an adaptable and scalable design framework for future bioinspired robotic fingers. This chapter is organized as follows. Section 4.2 presents the methods used, beginning with a conceptual overview and discussing locking mechanism design and force analysis followed by actuators, finger

kinematic analysis, multiple grasp modes, and fabrication. Section 4.3 presents results, divided into pneumatic actuator expanding test, fingertip force test, locking tendon force test, finger bending test, grasping capability and performance, durability test, and tensile tests of SLA 3D-printed material. Section 4.4 presents a discussion on the work and how it relates to the field, concluding remarks, and suggests the future steps.

4.2 Method

We present a bioinspired soft finger with a soft-rigid hybrid structure, which consists of a locking mechanism system at the bottom and a pneumatic actuator at the top, and use five connecting belts to attach them together (Figure 4.3A). In order to achieve the same fast and powerful movements as human fingers, two types of actuators are used: pneumatic actuator and tendon-driven actuator (Figure 4.3B). A tendon-driven actuator cable is embedded in the locking mechanism. A pneumatic actuator enables fast actuation of the bioinspired soft finger, and it is highly compliant, offers an infinite degree of freedom (DOF), and at low cost. At the same time, the tendon-driven actuator can provide higher payload capability.

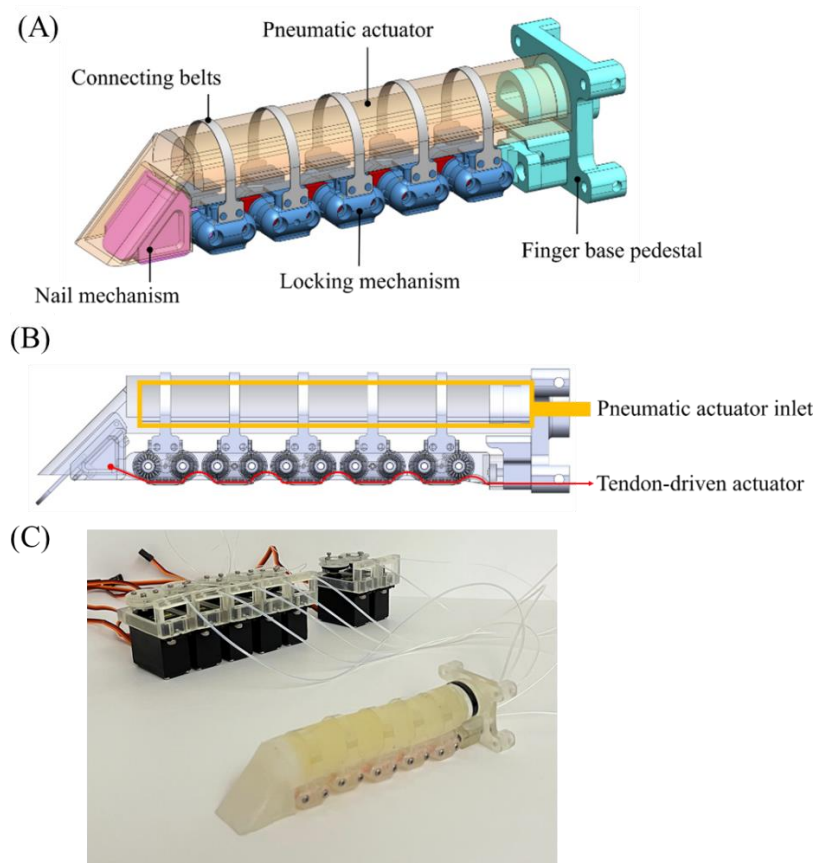


Figure 4.3: Bioinspired soft finger with a soft-rigid hybrid structure. (A). The overall components. (B). Two types of actuators are used for the finger (the yellow frame indicates a pneumatic actuator, and the red line indicates a tendon-driven cable). (C). Bioinspired soft finger with total 7 sets of Bowden cable assemblies, including 5 sets for locking modules, one for nail mechanism, and one is tendon-driven cable.

The chain-like locking mechanism is composed of five independently controllable locking modules and a nail mechanism connected to a fingertip (Figure 4.3A). Here we use 6 Bowden cable assemblies (similar in concept to the mechanism used to transmit force in many bicycle handbrakes) to control the lock and unlock of the 5 sets of locking modules and the extension of the nail mechanism. We use the servo motors (TowerPro MG996R) connected to the Bowden cables to provide tension force. In the locking mechanism, each rotating joint can be freely rotated with the

locking modules in the unlocked position, just like a watch strap can be freely bent with different curvatures. Upon engaging any one of the five locking mechanisms, each rotation joint is restricted to rotate with the locking modules in the locked position, and the locking mechanism is turned into a rigid body so that external forces can be supported by it. Thus, provided that the locking modules do not slip, the support force of the finger can be determined by the material properties of the locking modules. The finger parameters and index are shown in Figure 4.4 and Table 4.2.

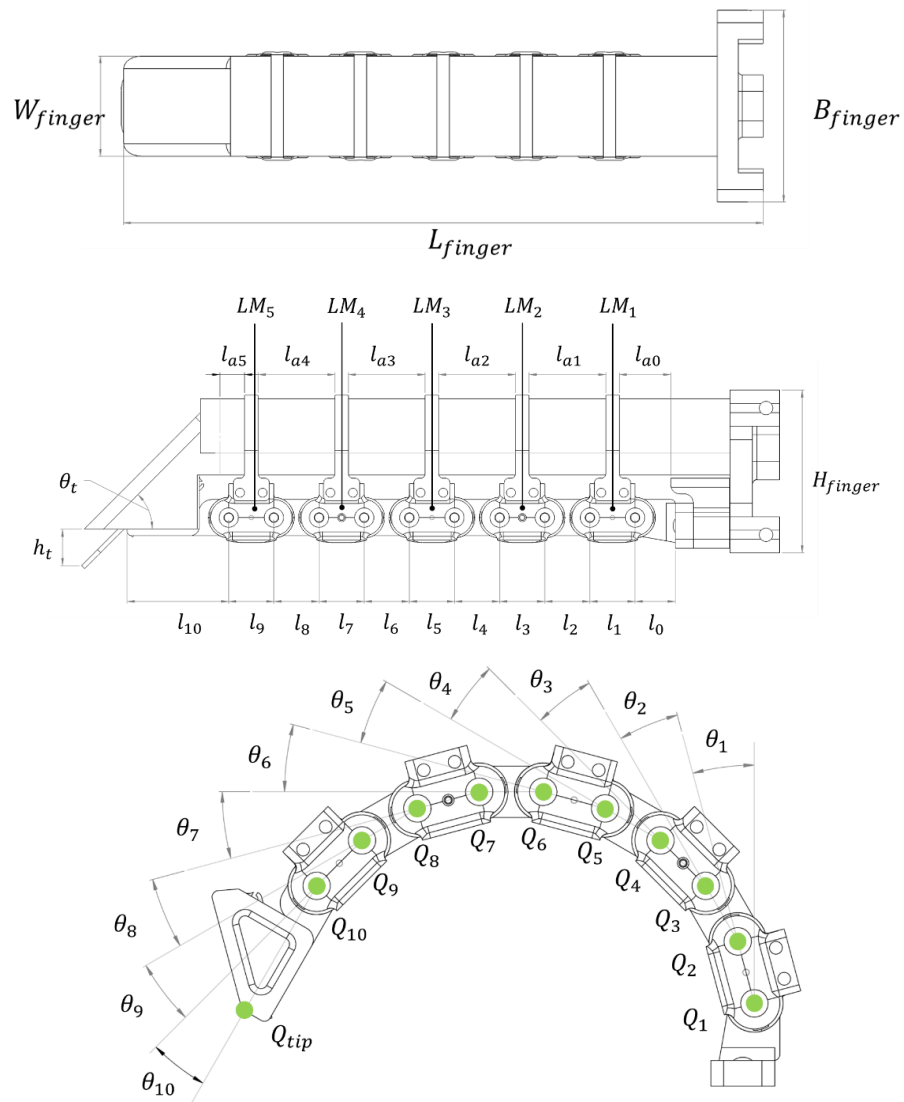


Figure 4.4: The finger parameters and index.

Table 4.2 Parameters of the finger

<i>Parameters</i>		<i>Values</i>	<i>Unit</i>
Finger net weight	-	68.8	gram
Finger width	W_{finger}	24	mm
Finger length	L_{finger}	154	mm
Finger base pedestal width	B_{finger}	46	mm
Finger height	H_{finger}	36	mm
Fingertip angle	θ_t	45	degree
Connecting belt width	-	3	mm
Pneumatic actuator length	-	99.9	mm
Pneumatic actuator segment length	l_{a0}	11.4	mm
Pneumatic actuator segment length	l_{a1-4}	17	mm
Pneumatic actuator segment length	l_{a5}	5.5	mm
Maximum nail elongation high	h_t	8.05	mm
Locking mechanism segment length	l_0	8.9	mm
Locking mechanism segment length	l_{1-9}	10	mm
Locking mechanism segment length	l_{10}	22.5	mm
Rotation joint	Q_i ($i = 1\sim 10$)	-	-
Bending angle on the i^{th} joint	θ_i ($i = 1\sim 10$)	-	degree
Fingertip endpoint (rigid part)	Q_{tip}	-	-
Total bending angle of end-effector nail mechanism	θ_{end}	-	degree
The i^{th} locking module	LM_i ($i = 1\sim 5$)	-	-

4.2.1 Locking Mechanism Design

The mechanical structure of the chain shape locking mechanism system was made by stereolithography (SLA) 3D-printer (Form 3, Formlabs, Somerville, MA) and composed of five locking modules, as shown in Figure 4.5A. Each locking module is composed of one rotation DOF, one Bowden cable (black line), and three rigid parts (one chain core and two side-crown). First, the chain core is a rigid part, which consists of two hollow parallel axes on two ends of the base; and two pairs of coaxial cone gears on two sides of the base. The other rigid part is the side-crown, consisting of two hollow parallel axes with the same distance as the core's axes. One side of the side-crown has

a pair of coaxial cone gears that can tightly mesh with the core's cone gears. This cone design can increase the contact area of the gear and the smoothness of meshing.

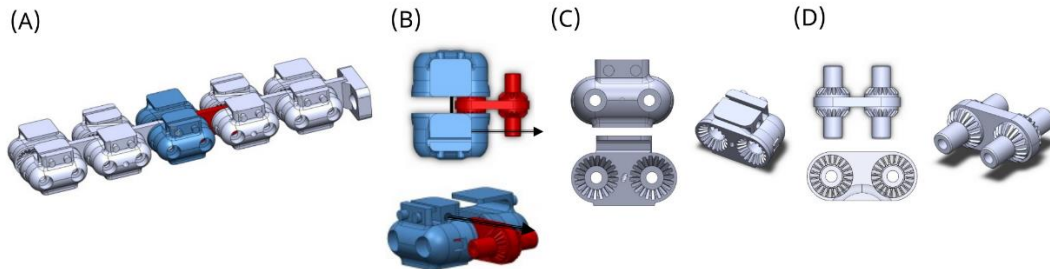


Figure 4.5: (A) Chain shape locking mechanism system. (B) One locking module, blue indicates two side-crown, red indicates as chain core, black arrow indicates the Bowden cable and the tendon force. There is space above each locking module for the Bowden cables to move freely between the locking modules and the pneumatic actuator (C) Side-crown with different views. There are two contact points on its upper half for the connecting belt (D) Chain core with different views. There is space in the middle for the tendon-driven cable to be embedded.

Also, inside the side-crown is an elastomeric band (yellow, 5 mm, 3/16-inch Orthodontic Elastic Rubber Band) perpendicular crossing the axes that provide a force to separate the core and the side-crown shown in Figure 4.6. A screw (green) passes through the side-crown and secures the core in Figure 4.7. It can adjust the gap between the core and the side-crown and allows the two parts can rotate freely. A locking module consisted of two side-crowns (blue) and one chain core (red), as shown in Figure 4.5A. Bowden cable can apply a tendon force to squeeze two side-crowns, and the cone gears can tightly mesh to jam the axis. This also allows the chain cores in the front and back locking modules to be linked together.

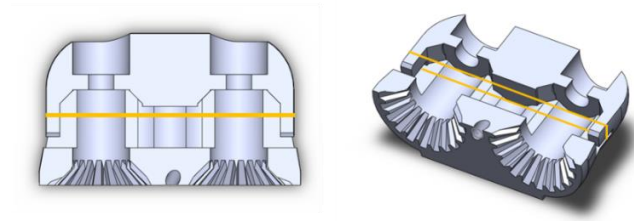


Figure 4.6: The yellow line indicates the elastomeric band perpendicular crossing the axes that provide a force to separate the core and the side-crown.

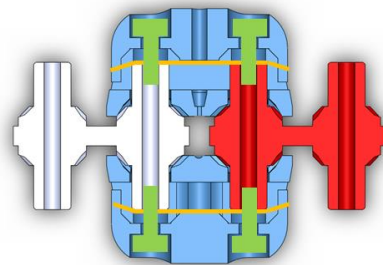


Figure 4.7: A locking module cross-section view. The red part indicates the chain core; the green part indicated the screws pass through the side-crown and secure to the chain core. The yellow line indicates the rubber band that provides the force to separate the chain core and the side-crown. The blue parts indicates the side-crowns, which have one DOF along the axis.

Multiple locking modules can be assembled to form a chain-shape locking mechanism system. Each module can provide two DOF in an in-plane bending direction, and it can approach relatively soft by connecting the multiple locking modules. Different from other robotic fingers, each joint can only control one bending angle; we designed each locking module to control both the front and rear bend angles. The advantage of this design is that for each module, the bending angle can be larger, and more easily control the fingers to apply force in a specific direction. For example, when the 1st locking module is locked, it means that joints Q_2 and Q_1 are locked so that the bending angle θ_2 and θ_1 is fixed. By analogy, when the i^{th} locking module is

locked, joints Q_{2i} and Q_{2i-1} are locked, bending angle θ_{2i} and θ_{2i-1} are fixed, shown in Figure 4.8.

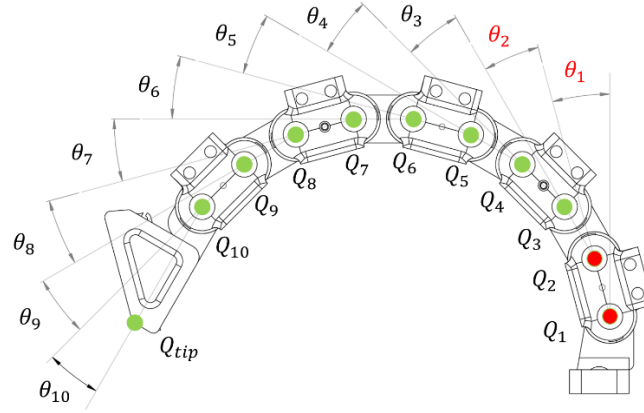


Figure 4.8: Illustration of when the first locking module is locked, the joints Q_2 and Q_1 will be locked so that the bending angle θ_2 and θ_1 is fixed as shown in red color. By analogy, when the i^{th} locking module is locked, joints Q_{2i} and Q_{2i-1} are locked, bending angle θ_{2i} and θ_{2i-1} are fixed.

4.2.2 Locking Mechanism Force Analysis

This section analyzes what forces and magnitudes of forces are present on the locking module and when they occur. We also calculate the torque and the corresponding force required for the locking module to withstand the external force. As shown in Figure 4.9, in soft mode(unlocked), there are two forces in the locking module: Screw support force and elastomeric band force. This allows the locking module to maintain a certain gap and allows the chain core and side-crown to rotate freely. In rigid mode(locked), because of the tension provided by the Bowden cable, the locking module makes the two side-crown engage with the chain core. The servo motor (MG996R) we use connected to the Bowden cable can provide a maximum

torque of 11 kg*cm (at 6 V). When an external force is applied to the locking module, a bending moment is generated, creating torque on the rotating joints. We can use the method of analyzing bevel gear to calculate the lateral force on the locking module.

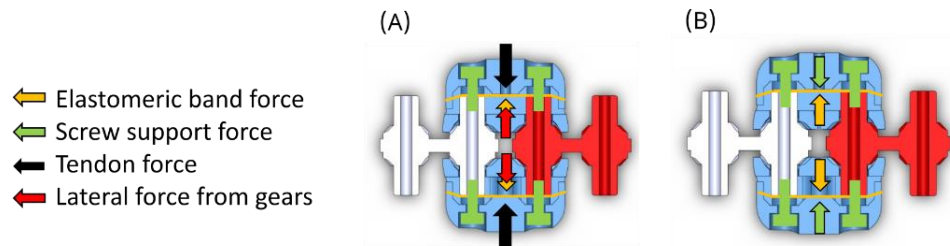


Figure 4.9: Force diagram in the locking module. (A) Rigid mode or lock mode. (B) Soft mode or unlock mode.

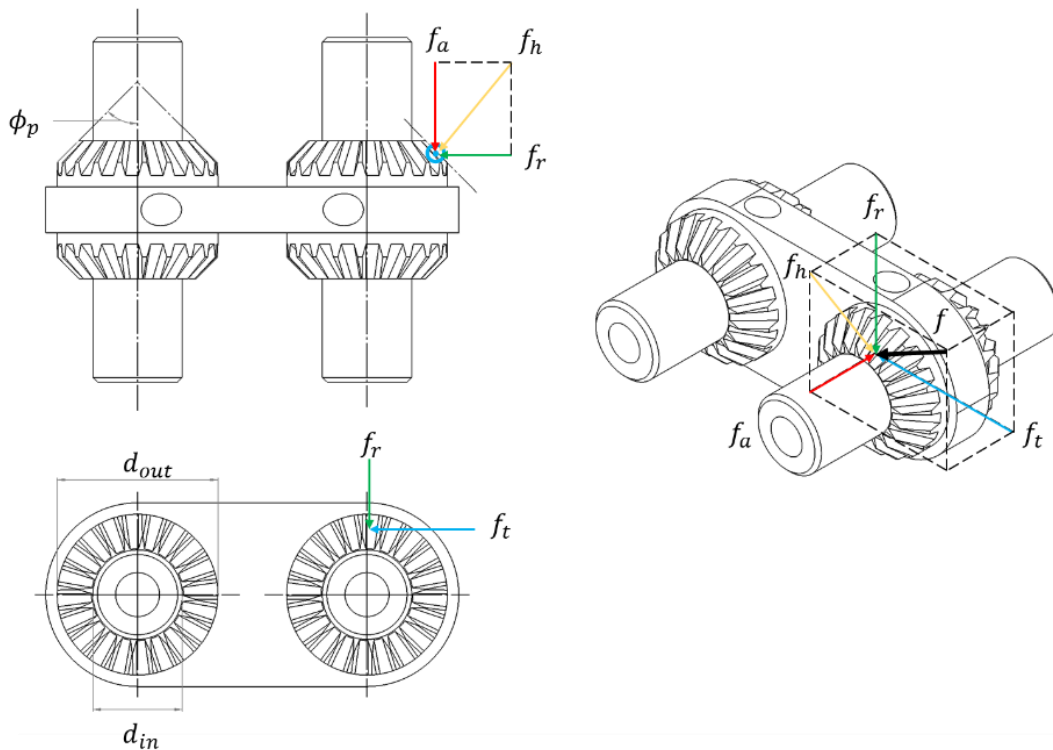


Figure 4.10: Force analysis diagram of the locking module-chain core.

Table 4.3 Parameters of the locking module

<i>Parameters</i>		<i>Values</i>	<i>Unit</i>
Torque on the rotating joint	τ_q	-	N*mm
Teeth number	N	20	-
Pitch circle diameter	d_p	5.5	mm
Inner circle diameter	d_{in}	4	mm
Outer circle diameter	d_{out}	7	mm
Overall force	f	-	N
Total tangential force	f_t	-	N
Tangential force on each tooth	f_{tn}	-	N
Pressure angle	ϕ_p	20	Degree
Pitch angle	ψ	45	Degree
Yellow hypotenuse	f_h	-	-
Radial force	f_r	-	N
Axial force	f_a	-	N
Moment arm	r_{arm}	-	mm

As shown in Figure 4.10 and Table 4.3, we can know our chain core design parameters. When analyzing the contact force, we can regard torque τ_q as tangential components of the force. While this force is in reality is the pressure distributed across the face of the gear tooth, we represent it here as a point load at the pitch circle (d_p) which is the average between the inner circle (d_{in}) and the outer circle (d_{out}). The overall force f would be perpendicular to the surface of the teeth, which is the angle between the tangential component in the blue arrow (f_t) and the overall force in the black arrow (f) would be that of the pressure angle (ϕ_p). The tangential component would be:

$$f_t = f * \cos (\phi_p) \quad (4.1)$$

Now, this vector also has two other components, which are the radial and the axial components. And both will be given by that pitch angle (ψ). The radial component,

which the force going into the center of the gear will be the adjacent side of the triangle with (ψ) in it using a yellow hypotenuse. The axial component that is parallel to the axis of the gear will be the opposite side of that same triangle.

$$f_r = f_h * \cos (\psi) \quad (4.2)$$

$$f_a = f_h * \sin (\psi) \quad (4.3)$$

The yellow hypotenuse is the length from the beginning of the f_t vector to the beginning of the f vector, which can be calculated with the pressure angle.

$$f_h = f * \sin (\phi_p) \quad (4.4)$$

The radial and axial components can be written by substituting f and then f_h .

$$f_r = f * \sin (\phi_p) * \cos (\psi) \quad (4.5)$$

$$f_r = \frac{f_t * \sin (\phi_p) * \cos (\psi)}{\cos (\phi_p)} \quad (4.6)$$

$$f_a = f * \sin (\phi_p) * \sin (\psi) \quad (4.7)$$

$$f_a = \frac{f_t * \sin (\phi_p) * \sin (\psi)}{\cos (\phi_p)} \quad (4.8)$$

Simplifying the trigonometric functions, we can find the three expressions for each one of the components.

$$f_t = f_t \quad (4.9)$$

$$f_r = f_t * \tan (\phi_p) * \cos (\psi) \quad (4.10)$$

$$f_a = f_t * \tan (\phi_p) * \sin (\psi) \quad (4.11)$$

And now we have the expressions for the components of the chain core gear forces in terms of the pressure angle ϕ_p and the pitch angle ψ . The torque τ_q can be written as:

$$\tau_q = f_t * r_{arm} \quad (4.12)$$

$$f_a = \frac{\tau_q}{r_{arm}} * \tan (\phi_p) * \sin (\psi) \quad (4.13)$$

At the same time, we can know that the force on each tooth is

$$f_{tn} = \frac{f_t}{N} \quad (4.14)$$

From the above analysis, we can estimate how much tendon force support is required for the torque generated by the external force acting on the locking module. We can also know the maximum shear force that the teeth on the locking module can withstand.

4.2.3 Pneumatic Actuator and Tendon-driven Actuator

Pneumatic Actuator

To achieve fast actuation and be highly compliant, we have chosen a pneumatic actuator as one of the finger drive methods. The pneumatic actuator itself can be roughly classified according to its motion path: contracting actuators, expanding actuators, twisting actuators, and bending actuators. All these actuators rely on the same basic physical principle: Pascal's principle. When we design the actuator, we can make different positions of the inflatable cavity produce different morphological changes

under the same pressure or restrict the movement of the inflatable cavity in a specific direction to achieve different motion paths. The common methods are using multiple materials and asymmetric geometries. A more comprehensive overview of pneumatic actuators can be found in chapter 2 and the literature [131]–[134].

In the design of the pneumatic actuator in this article, we use fiber-reinforced expanding actuators. The locking mechanism system is a rigid, non-extendable structure that extends from the finger base pedestal to the nail mechanism at the tip of the finger, and the nail mechanism is bonded to the front of the pneumatic actuator. As a whole, it restricts the elongation movement of the finger. After trying various pneumatic actuator designs, we found that the expanding actuators were the most suitable for finger movement in this study. At the same time, the design of fiber-reinforced can keep the walls of the cavity relatively thin, lightweight, and smooth. This is helpful for predicting motion models and finite element analysis [131]. As shown in Figure 4.11, we designed the cavity with a semicircular cross-section, which allows enough space under the pneumatic actuator for the Bowden cable sets. The semicircular shape also allows the plane under the pneumatic actuator to have stable contact with the locking mechanism system. We design 5 connecting belts to connect the locking mechanism system with the pneumatic actuator. The 5 connecting belts are connected to the top of the 5 locking modules respectively, and the pneumatic actuator is divided into 6 segments l_{a0-5} in Figure 4.4.

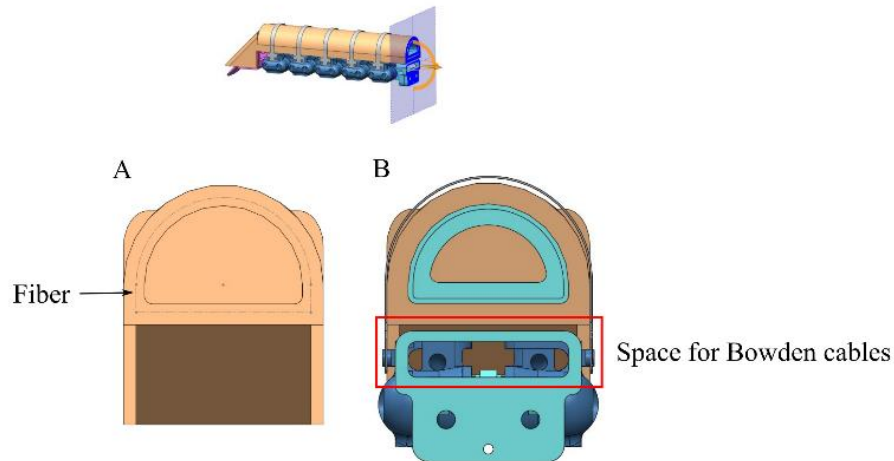


Figure 4.11: (A) The pneumatic actuator semicircular cavity view. (B) The cross-section view of the assembly finger shows the space under the pneumatic actuator for the Bowden cable sets.

Once the pneumatic actuator starts to inflate, the walls of the cavity will first come into contact with the connecting belts. This allows each section of the pneumatic actuator to provide a forward extension movement depending on whether the locking module is locked or unlocked. For example: When only the 3rd locking module is unlocked, only the pneumatic actuators of the two segments l_{a2} and l_{a3} will have extension movement. This design allows the extension control of different segments in the same pneumatic actuator under the same pressure. Make the pneumatic actuator and the locking mechanism system consistent in motion control.

Tendon-driven Actuator

To compensate for the lack of grasping force of the pneumatic actuator, we added a tendon-driven actuator to our finger. The tendon-driven cable is attached to the nail mechanism through a small hole in the middle of each chain core from the tip of

the finger all the way to the finger base pedestal. After the finger has used the pneumatic actuator, if additional force is needed, the tendon-driven cable can provide additional torque on the rotary axis, allowing the finger to deliver more force. The servo we use (MG996R) is connected to the tendon-driven cable and can provide up to 11kg*cm torque.

One thing to note here is that the tendon-driven actuator must be used after the pneumatic actuator has been activated. If the tendon were to be activated while the finger is straight (pneumatic actuator not engaged), the moment arm between the cable and the center of rotation (axis of rotation of the locking mechanism) is too small to generate bending moment. It will also cause misalignment between the pneumatic actuator and the structure of the connecting belt.

4.2.4 Kinematic Analysis

The locking mechanism system consists of 5 rigid modules connected by intermediate rotation joints, including side-crowns and chain cores of equal length. When all the locking modules are unlocked, the locking mechanism system has 10 DOF. The kinematic model of a 10 DOF locking mechanism system in a 2D Cartesian space is shown in Figure 4.12. Using forward kinematics to derive the end-effector is the typical way of deriving the end-effector position of a rigid robotic manipulator. Therefore, here we use a systematic approach based on the Denavit-Hartenberg (D-H) convention to derive the forward kinematic equations for the end-effector nail

mechanism position of the locking mechanism. The following four transformation parameters are known as Denavit-Hartenberg parameters [135]:

- θ_i angle about previous z_{i-1} from old x_{i-1} to new x_i
- a_i is the length of the link about the common normal
- α_i angle about common normal, from old z_{i-1} to new z_i
- d_i offset along with previous z_{i-1} to the common normal

Where i represents the number of links, through concatenation of these individual transformations, the equivalent homogeneous transformation is:

$${}^{i-1}_i T(\theta_i, a_i, \alpha_i, d_i) \quad (4.15)$$

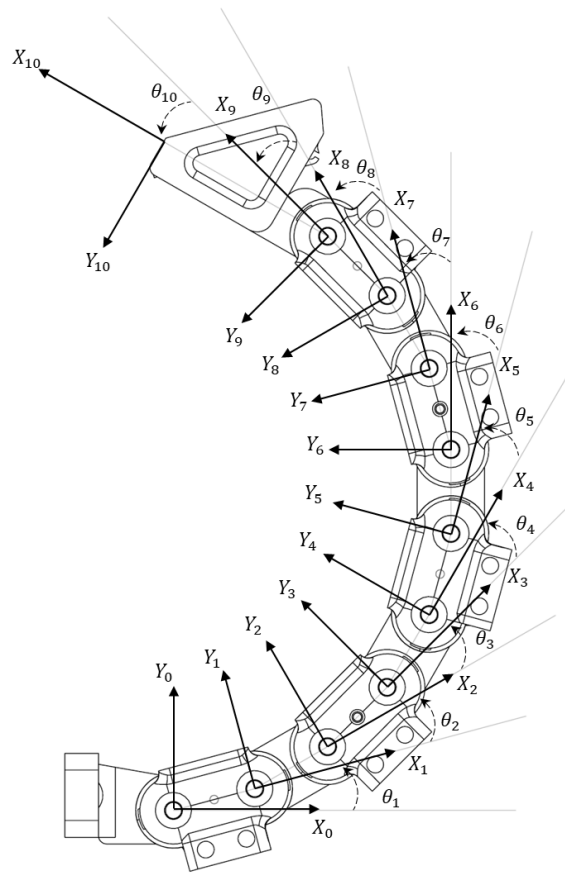


Figure 4.12: Kinematic model of 10 DOF locking mechanism system in a 2D Cartesian space.

Table 4.4 D-H Parameters for the locking mechanism system

Link i	θ_i	a_i	α_i	d_i
1	θ_1	l_1	0	0
2	θ_2	l_2	0	0
3	θ_3	l_3	0	0
4	θ_4	l_4	0	0
5	θ_5	l_5	0	0
6	θ_6	l_6	0	0
7	θ_7	l_7	0	0
8	θ_8	l_8	0	0
9	θ_9	l_9	0	0
10	θ_{10}	l_{10}	0	0

In the coming equations, we make the following notation:

$$c_i = \cos(\theta_i), c_{ijk\dots} = \cos(\theta_i + \theta_j + \theta_k + \dots)$$

$$s_i = \sin(\theta_i), s_{ijk\dots} = \sin(\theta_i + \theta_j + \theta_k + \dots)$$

Substituting the parametric details from the D-H table in Table 4.4 into equation (4.15) provides the 4×4 transformation matrix of the individual joints, which can be expanded as:

$${}^{i-1}T_i = \begin{bmatrix} c\theta_i & -s\theta_i & -s\theta_i & a_{i-1} \\ s\theta_i c\alpha_{i-1} & c\theta_i c\alpha_{i-1} & -s\alpha_{i-1} & -s\alpha_{i-1}d_i \\ s\theta_i c\alpha_{i-1} & c\theta_i c\alpha_{i-1} & c\alpha_{i-1} & c\alpha_{i-1}d_i \\ 0 & 0 & 0 & 1 \end{bmatrix} \quad (4.16)$$

Then the position and orientation of the end-effector in the inertial frame are given by:

$${}^0T_n = \prod_{i=1}^n {}^{i-1}T_i$$

$${}^0T_n = \begin{bmatrix} R_{3 \times 3} & P_{3 \times 1} \\ 0 & 1 \end{bmatrix} \quad (4.17)$$

Where matrix $R_{3 \times 3}$ expresses the orientation, and matrix $P_{3 \times 1}$ is the position vector of the last frame. The coordinate position of the nail mechanism end-effector (x, y) is given as the function of the joint angles θ_i ($i = 1 \sim 10$) and can be determined by having the product of the transformation matrices of the individual links, and it follows the equation

$$\begin{bmatrix} x \\ y \\ z \\ 1 \end{bmatrix} = {}_{10}^0T \begin{bmatrix} 0 \\ 0 \\ 0 \\ 1 \end{bmatrix} \quad (4.18)$$

According to equations (4.16) and (4.17), it is obtained the homogeneous transformation matrix ${}_{10}^0T$, which is used to derive the end-effector position with respect to the global reference frame, and it is the Jacobian matrix that follows the equation

$${}_{10}^0T = {}_1^0T \cdot {}_2^1T \cdot {}_3^2T \cdot {}_4^3T \cdot {}_5^4T \cdot {}_6^5T \cdot {}_7^6T \cdot {}_8^7T \cdot {}_9^8T \cdot {}_{10}^9T \quad (4.19)$$

$${}_{10}^0T = \begin{bmatrix} c_{123456789\ 10} & -s_{123456789\ 10} & 0 & P_x \\ s_{123456789\ 10} & c_{123456789\ 10} & 0 & P_y \\ 0 & 0 & 1 & P_z \\ 0 & 0 & 0 & 1 \end{bmatrix} \quad (4.20)$$

$$P_x = l_{10}c_{123456789\ 10} + l_9c_{123456789} + l_8c_{12345678} + l_7c_{1234567} + l_6c_{123456} + l_5c_{12345} + l_4c_{1234} + l_3c_{123} + l_2c_{12} + l_1c_1 \quad (4.21)$$

$$P_y = l_{10}s_{123456789\ 10} + l_9s_{123456789} + l_8s_{12345678} + l_7s_{1234567} + l_6s_{123456} + l_5s_{12345} + l_4s_{1234} + l_3s_{123} + l_2s_{12} + l_1s_1 \quad (4.22)$$

$$P_z = 0 \quad (4.23)$$

As a result, when all the locking modules are unlocked, the end-effector nail mechanism position and orientation can be determined using the equations below.

$$\begin{aligned}
x = & l_{10} \cos(\sum_{i=1}^{10} \theta_i) + l_9 \cos(\sum_{i=1}^9 \theta_i) + l_8 \cos(\sum_{i=1}^8 \theta_i) + l_7 \cos(\sum_{i=1}^7 \theta_i) + \\
& l_6 \cos(\sum_{i=1}^6 \theta_i) + l_5 \cos(\sum_{i=1}^5 \theta_i) + l_4 \cos(\sum_{i=1}^4 \theta_i) + \\
& + l_3 \cos(\sum_{i=1}^3 \theta_i) + l_2 \cos(\theta_1 + \theta_2) + l_1 \cos(\theta_1)
\end{aligned} \tag{4.24}$$

$$\begin{aligned}
y = & l_{10} \sin(\sum_{i=1}^{10} \theta_i) + l_9 \sin(\sum_{i=1}^9 \theta_i) + l_8 \sin(\sum_{i=1}^8 \theta_i) + l_7 \sin(\sum_{i=1}^7 \theta_i) + \\
& l_6 \sin(\sum_{i=1}^6 \theta_i) + l_5 \sin(\sum_{i=1}^5 \theta_i) + l_4 \sin(\sum_{i=1}^4 \theta_i) + l_3 \sin(\sum_{i=1}^3 \theta_i) + \\
& l_2 \sin(\theta_1 + \theta_2) + l_1 \sin(\theta_1)
\end{aligned} \tag{4.25}$$

$$\theta_{end} = \sum_{i=1}^{10} \theta_i \tag{4.26}$$

4.2.5 Fingers in Multiple Grasp Modes

Our proposed hybrid bioinspired finger consists of 5 independently controllable locking modules, one nail mechanism, and two types of actuators. By implementing adjustable stiffness locking modules, a finger can perform different gripping modes depending on the stiffness of the locking modules. In this section, we can broadly

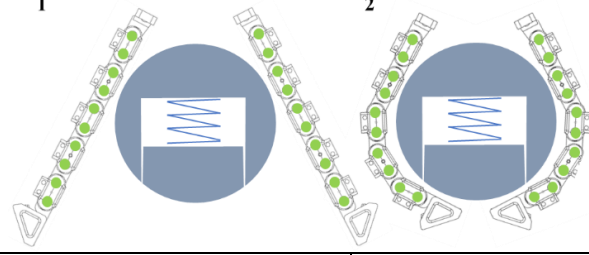
classify the gripping modes into three modes according to the use of locking modules: **(1) Pure soft mode**, when all locking modules are unlocked all the time. **(2) Soft-rigid hybrid modes**, when the locking modules need to be locked or unlocked during finger use. **(3) Rigid mode**, in which the specific locking modules are kept locked all the time during finger use.

Among them, (2) Soft-rigid hybrid mode, according to the order of actuators and locking modules activation, can be subdivided into three capture modes: (A) Adaptive power mode. (B) Pre-shaped mode. (C) Hybrid loop mode. We will explain the movement of each mode in detail below.

4.2.5.1 Pure Soft Mode

In this mode, we keep each locking module in the locking mechanism system in a soft position (unlocked), and each module can rotate freely. Used together with the pneumatic actuator, it can quickly grip irregularly shaped and fragile objects. During the procedure, when the locking module touches the object, it will adjust its clamping curvature according to the shape of the object with its own compliance characteristics. This is shown in Table 4.5.

Table 4.5 Pure soft mode grasping procedure

		Grasping procedure	
		1	2
Pure soft mode	Joint state ● Unlocked ● Locked		
	Module locked	-	-
	Pneumatic	Off	Active
	Tendon	Off	Off

4.2.5.2 Soft-rigid Hybrid Modes

A. Adaptive Power Mode

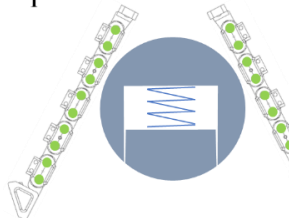
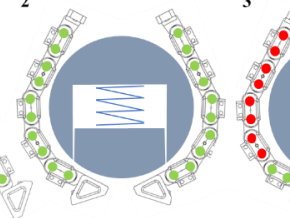
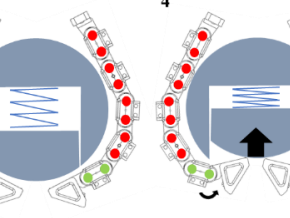

The user first keeps each locking module in the unlocked state and then inflates the pneumatic actuator to grasp the object. At this time, the finger can quickly adapt to the shape of the object and adjust the curvature of grasping. So far, this is the same action as pure soft mode. Then the one (or more) locking modules that need to provide additional force in a specific direction remain in the unlocked state, allowing that module to rotate freely.

The rest of the locking modules are turned into the locked state, making the fingers become two (or more) rigid link motion models. At this time, the rigid links are the same shape as the object. When using the tendon-driven actuator (to provide additional torque) on the locking modules, which remain in the unlocked state to

provide extra torque. This allows the rigid linkage to output force in a specific direction.

This is shown in Table 4.6.

Table 4.6 Adaptive power mode grasping procedure

Adaptive power mode	Grasping procedure			
	1	2	3	4
Joint state ● Unlocked ● Locked				
Module locked	-	-	#1, 2, 3, 4	#1, 2, 3, 4
Pneumatic	Off	Active	Active	Active
Tendon	Off	Off	Off	Active

B. Pre-shaped Mode

The user pre-locks specific locking modules to keep the finger in the interval with a straight rigid link, and then drives the finger to grasp the object by the pneumatic actuator. This allows us to know the bending trajectory of the finger in advance so that we can accurately control the gripping distance and then be more precise in gripping small objects, such as credit cards and tiny screws. If more power is needed, a tendon-driven actuator can be added and used simultaneously. This is shown in Table 4.7.

Table 4.7 Pre-shaped mode grasping procedure

Pre-shaped mode	Grasping procedure					
	Joint state	1	2	3	4	
	● Unlocked					
	● Locked					
	Module locked	-	#1, 2, 4, 5	#1, 2, 4, 5	#1, 2, 4, 5	
Pneumatic	Off	Off	Active	Active		
Tendon	Off	Off	Off	Active		

C. Hybrid Loop Mode

In this mode, the locking modules and the pneumatic actuator are used interchangeably. The user can adjust the sequence of the two actions to meet the target requirements. Basically, it can be regarded as a mix of adaptive power mode and pre-shaped mode.

4.2.5.3 Rigid Mode

The word rigid is used here to refer to the specific locking modules that remain locked all the time. This mode will be discussed in more detail in section 4.2.6, but we list it here to give the article a complete structure.

4.2.6 Programmability Setting

In the previous subsections, we discussed how the fingers are used to control the locking modules to accomplish complex grasping tasks independently. Although many combinations of fingers can be used, they also require multiple servo motors to

work together. This finger is modular in design; it has a potential mode called pre-program mode or rigid mode in the previous subsection (illustrated in Table 4.8).

This mode allows the locking modules to predetermine their respective states: locked or unlocked. In the case of locked, the locking angle of the two modules is also predetermined. When the state is decided, it cannot be switched arbitrarily during the operation. In other words, the bending trajectory of the finger has been predetermined. Because the locking modules do not need to change their state, we can remove the Bowden cables that control them. This reduces the DOF of the fingers but also reduces the complexity of the control, which we also call pre-program mode here.

Table 4.8 Pre-program mode grasping procedure

		Grasping procedure		
		1	2	3
Pre-program mode	Joint state			
	Module locked	#1, 2, 4, 5	#1, 2, 4, 5	#1, 2, 4, 5
	Pneumatic	Off	Active	Active
	Tendon	Off	Off	Active

4.2.7 Design & Fabrication

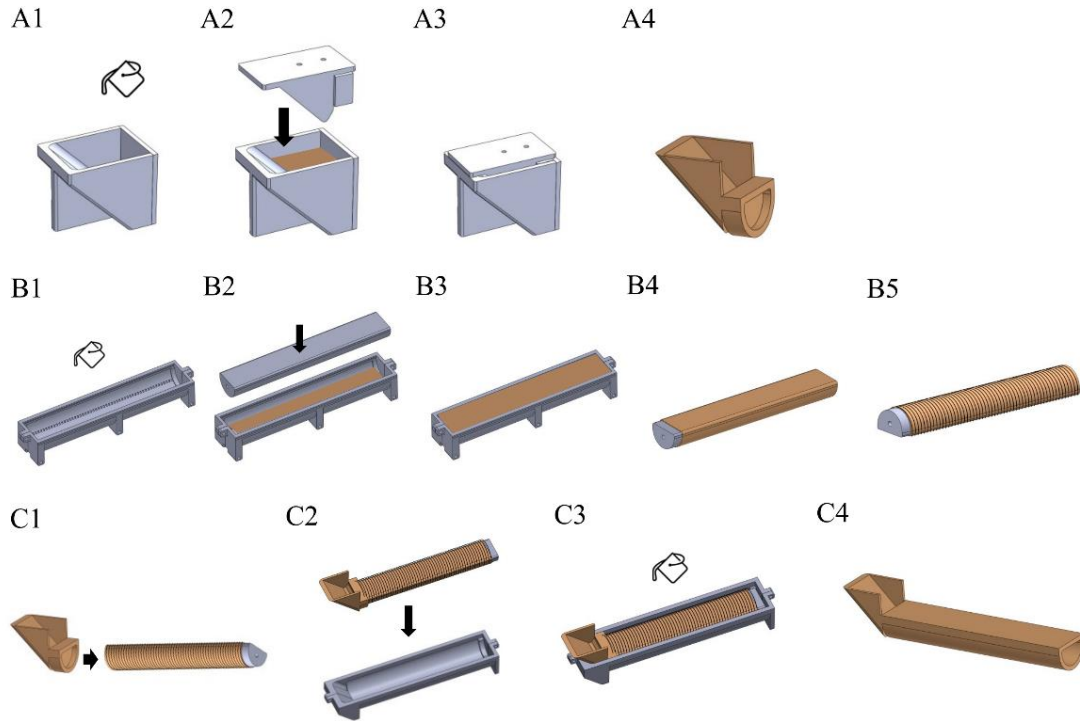


Figure 4.13: Pneumatic actuator fabrication process. The assembly is fabricated using three molding steps, and molds are shown in gray. (A) Mold A, the pneumatic actuator fingertip fabrication process, (A1-A4). (B) Mold B, the inner layer of the pneumatic actuator for winding reinforced fibers. (C) Mold C, finished pneumatic actuator fabrication.

Pneumatic Actuator

Similar in concept to many soft robots, we fabricate our fiber-reinforced pneumatic actuator using multiple molding steps. The fabrication process is summarized in Figure 4.13. We fabricate the assembly using three molding steps. The actuator mold is designed in Solidworks, and 3D printed using a Form 3 SLA printer (Formlabs, Somerville, MA, USA). The mold is assembled and held together firmly with screws.

Mold A:

We fill elastomer Dragon Skin 10 (Smooth-On, Inc. Macungie, PA, USA) into the mold (Figure 4.13A1) and degas it in a vacuum chamber for 5 minutes. We insert the top mold into the bottom mold and squeeze the elastomer so that it fills the entire mold (Figure 4.13A2). We cure the elastomer in an oven at 60 °C for 40 minutes.

Mold B:

We fill elastomer Dragon Skin 10 into the mold, and insert the center rod into the mold to create the core of the actuator. The rod slots into a half-round indentation at two mold ends (Figure 4.13B2). We degas the assembly in a vacuum chamber for 10 minutes and refill the elastomer if necessary. We cure the elastomer in an oven at 60 °C for 40 minutes. We remove the external mold but retain the center rod with elastomer (Figure 4.13B4). We wind the fibers spirally on the outside of the center rod, and at both ends of the actuator, and we knot them (Figure 4.13B5).

Mold C:

We demolded the mold A and inserted the part into the center rod from mold B (Figure 4.13C1). We put the assembled part into mold C and fill with elastomer Dragon skin 10. We degas in a vacuum chamber for 10 minutes and refill the elastomer if necessary. We cure the elastomer in an oven at 60 °C for 40 minutes.

Finger Assembly and Integration

The rigid components, including locking modules, nail mechanism, and finger base pedestal, are designed in Solidworks, and 3D printed using Clean V4 resin with Stereolithography (SLA) 3D printing technology Form 3 (Formlabs, Somerville, MA, USA). In order to understand whether the mechanical properties of SLA 3D printing will vary depending on the printing angle, we have verified the printing angle and mechanical properties of SLA in the next section. The connecting belts are made of plastic sheets with a thickness of 0.1mm, made by laser cut.

When all the above parts are ready, we assemble the finger. We begin by bonding the outer shell of the nail mechanism to the pneumatic actuator, with Ecoflex 00-30 (Smooth-On, Inc. Macungie, PA, USA) as the bonding adhesive. The pneumatic actuator and nail mechanism are bonded as shown in Figure 4.15. **First**, we cut the fabric (monofilament polyester screen, 43 threads per inch) into the same shape as the side of the nail mechanism and lay it on the surface. **Second**, we use a dropper to apply some liquid SLA Clean V4 resin to the edge of the nail mechanism and the fabric, allowing the liquid SLA resin to penetrate into the fabric. After exposing with UV light to cure the SLA resin, we use this method to stick the fabric and the nail mechanism together. We repeat the above action and let the fabric on both sides of the nail mechanism stick to the surface. We can see from the cross-section (Figure 4.14E) a cavity between the fabric and the nail mechanism. **Third**, we glue the upper part of the outer shell of the nail mechanism together with the pneumatic actuator. We fill the front

half of the pneumatic actuator with Ecoflex 00-30, and put the outer shell of the nail mechanism in, then cure it in an oven at 60° C for 25 minutes. We rotate the pneumatic actuator one-quarter turn and flip the sidewall of the fingertip. We use the dropper to fill the cavity on the side of the nail mechanism with Ecoflex 00-30, and cure the assembly at 60° C for 25 minutes. We repeat the above process to fabricate the other side of the pneumatic actuator, and we glue both sides of the nail mechanism with the pneumatic actuator. **Fourth**, we install a metal rod linear slide so that the nail can slide back and forth in the nail mechanism. Finally, we install an elastic rubber band (5 mm, 3/16-inch Orthodontic Elastic Rubber Band) to allow the nail to retract automatically. At this point, we have completed the assembly of the nail mechanism and the pneumatic actuator.

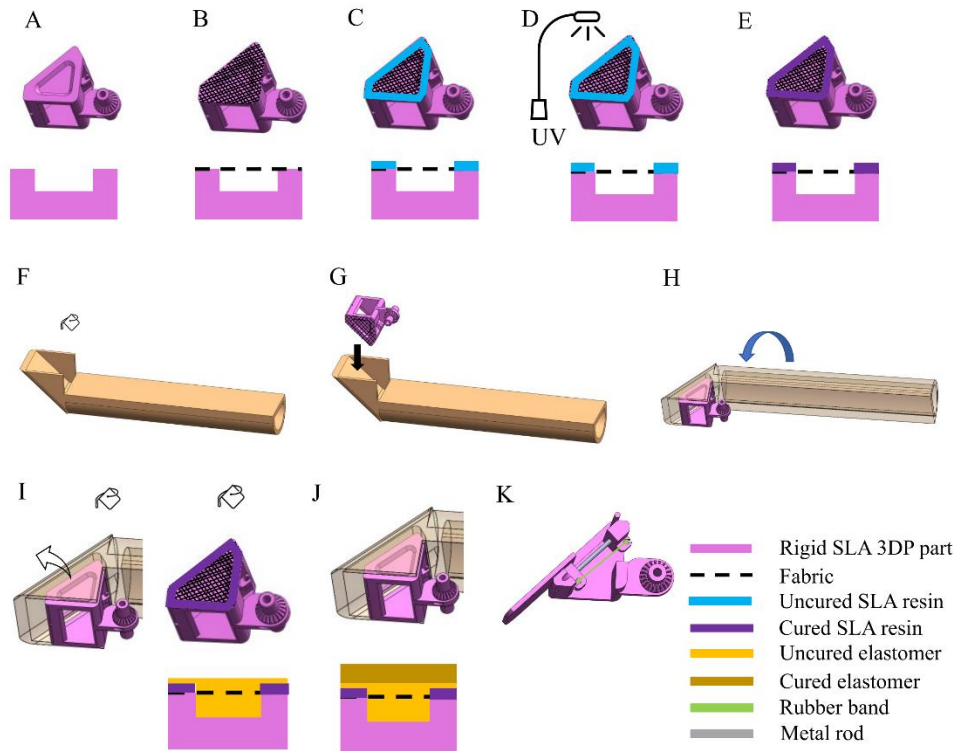


Figure 4.14: Pneumatic actuator and nail mechanism bonding process. (A-E) the bonding process of the fabric to nail mechanism by SLA resin. (F-J) The bonding process of the nail mechanism and pneumatic actuator. (K) Install a metal rod, elastic rubber band, and the nail into the nail mechanism.

Next, we complete the assembly that integrates the whole finger shown in Figure 4.15. First, we install the elastic rubber bands (5 mm, 3/16-inch Orthodontic Elastic Rubber Band) into each side-crown, using M2 screws to connect the chain cores and side-crowns. When connecting, adjust the tightness of the screws to make a proper distance between the two. Then connect the assembled locking mechanism to the finger base pedestal using M2 screws. Then start installing the five Bowden cable assemblies, an inner nylon cable (Monofilament nylon thread, diameter 0.5 mm) relative to a PTFE hollow outer tubing that control the locking modules. Next, fix the tendon-driven cable on the nail mechanism, and install the Bowden cable assembly that controls the nail.

Then we connect the nail mechanism to the locking mechanism and install the tendon-driven cable into the chain cores after the connection is completed. After that, we installed the pneumatic actuator inlet on the finger base pedestal with a zip tie. In order to protect the pneumatic actuator, we wrap Teflon tape around the surface of the contact area so that the zip tie does not directly touch the pneumatic actuator. The last step is to install the connecting belts on the side-crown top and combine the pneumatic actuator with the locking mechanism.

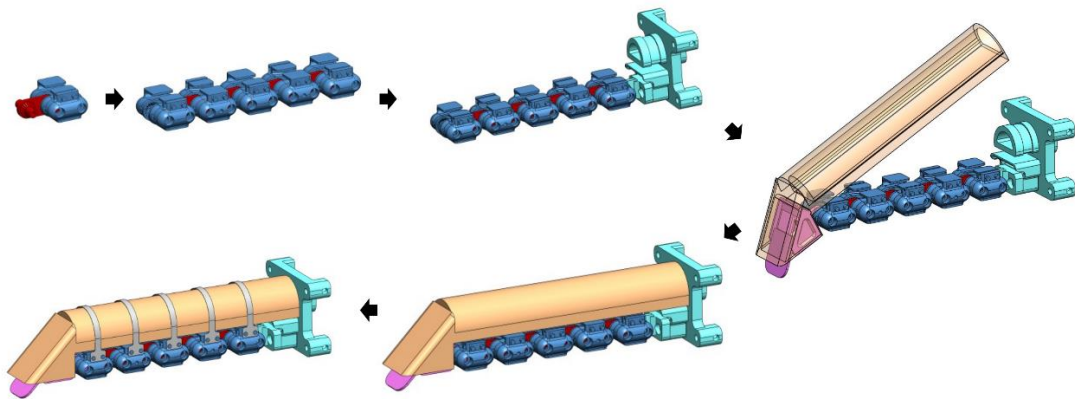


Figure 4.15: Bioinspired soft finger assembly process step diagram.

4.3 Results

4.3.1 Fiber-reinforced Pneumatic Actuator Expanding Test

Fiber-reinforced pneumatic actuator expanding test is shown in Figure 4.16. The pressure was increased approximately by 0.3 kPa (0.05 Psi) per 0.1 seconds, and experimental data for the relationship between input pressure and output elongation were presented. The extension exerted increased with increasing input pressure. An approximately linear relationship was observed, which can be deduced from the hyperelastic model method provided in this paper [131]. The elongation generated reached 75 mm at 25 kPa (3.7 Psi). We can use this approximately linear relationship to predict the surrounding range (< 35 kPa, < 5.1 Psi) pressure-elongation data. More testing has been done to offer a more comprehensive characterization of the soft hybrid finger design and an investigation into the sensitivity of each geometric parameter.

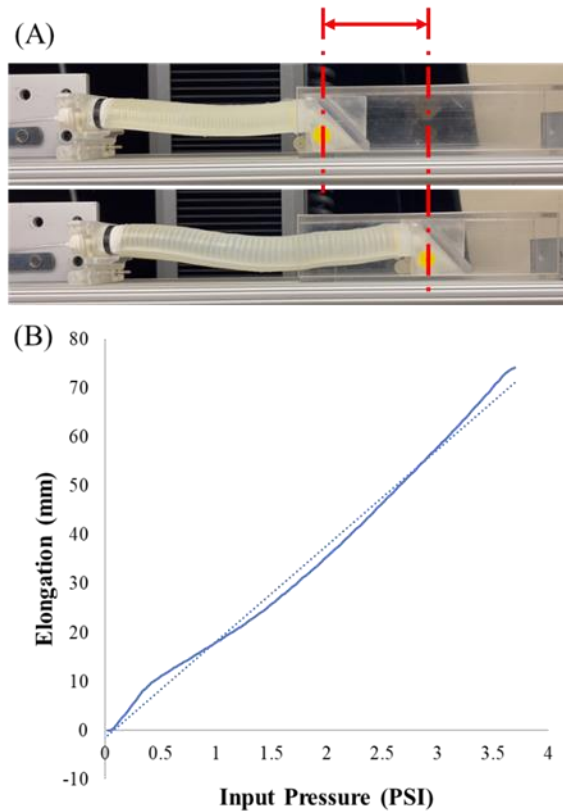


Figure 4.16: Fiber-reinforced pneumatic actuator expanding test and results: (A) Test setup of the actuator in the elongation experiment. (B) Test result for pressure and elongation configuration with the linear trendline.

4.3.2 Fingertip Force Test

In this test, we tested the relationship between the two types of actuators, pneumatic and tendon-driven, for fingertip force output. In the first experiment, we tested the relationship between the input pressure of the pneumatic actuator alone and the output force at the fingertip shown in Figure 4.17. From the experiment plot, the actuator force increases as the input pressure increases, and an approximately linear relationship is observed. The Instron 5943 tensile tester (Instron Co., Norwood, MA,

USA) is the measurement equipment we use for the experiment. The maximum force and actuation pressure tested were 1.7 N for the pneumatic actuator at 35.5 kPa (5.13 PSI). From the results, the efficiency of our pneumatic actuator and force output was relatively high (Mosadegh et al. [136]: pneumatic actuator 1.4 N at 10.4 Psi).

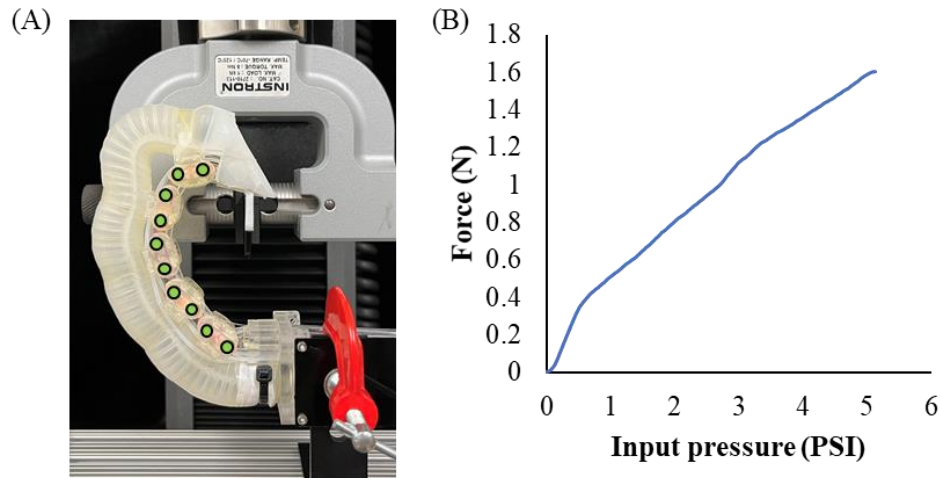


Figure 4.17: Fingertip force test and results: (A) Test setup of the finger on the Instron with all the locking modules in the unlocked state. (B) The pneumatic actuator input pressure and fingertip force output relationship plot.

In the second experiment, we wanted to determine the difference in force output at the fingertips when the two actuators are activated simultaneously versus pneumatic inflation only. We first inflated the pneumatic actuator to 35 Kpa (5.1 Psi) and maintained it throughout the experiment. We then activated the tendon-driven actuator at time 17 seconds and used the maximum tension force (107 N at 6 V) to pull the tendon-driven cable shown in Figure 4.18. From the experiment plot, the maximum fingertip force is 4.13 N, when both the pneumatic actuator and tendon-driven actuator are activated at the same time. Compared with the maximum fingertip force of 1.7 N

when only the pneumatic actuator is used, the fingertip force can be increased by 143%. This also proves that the tendon-driven actuator can provide higher payload capability as we mentioned in the previous section.

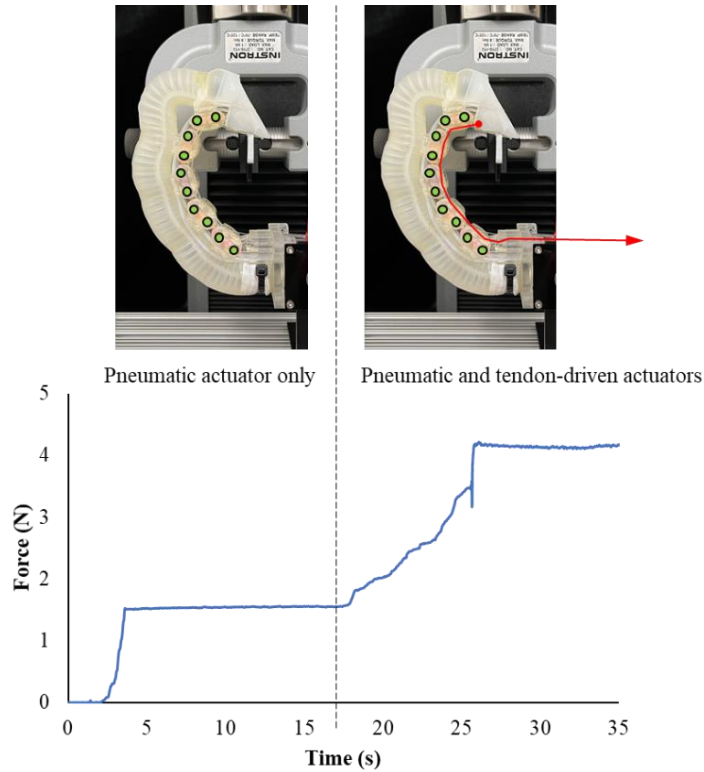


Figure 4.18: Fingertip force experiment results with two actuators. The finger is setup on the Instron with all the locking modules in the unlocked state and the red line indicates the tendon-driven cable. The pneumatic actuator inflated to 35 kPa (5.1 Psi) and maintained it all time during the experiment, then activated the tendon-driven actuator at time 17s.

4.3.3 Locking Mechanism Force Test

This section tests the relationship between the tension required for a single locking module and the bending moment caused by an external force. Figure 4.19 shows the setup of this experiment; we use Instron as the external force and install a locking module horizontally on the test platform. A Bowden cable is connected to a force gauge to apply a constant tensional force to the locking module for testing. Figure 4.20 shows that when the locking tensional force is 500g, the locking gear on Q_1 can withstand a maximum torque of $28\text{N} \cdot 20\text{mm} = 560\text{Nmm}$. When the locking tensional force increases to 700g, the locking gear on Q_1 can withstand a maximum torque of $41\text{N} \cdot 20\text{mm} = 820\text{Nmm}$. However, when the locking tensional force increases to 1000g, the locking module's chain core will break because the torque exceeds the strength of the material that can be loaded. Compared with the equation derived in the previous section, we have concluded from the experimental data that the locking tensional force required at the same bending moment is smaller than the theoretical value. This is due to the increased friction between the surfaces of the mating gears, making it more difficult to separate the gear when it has meshed together.

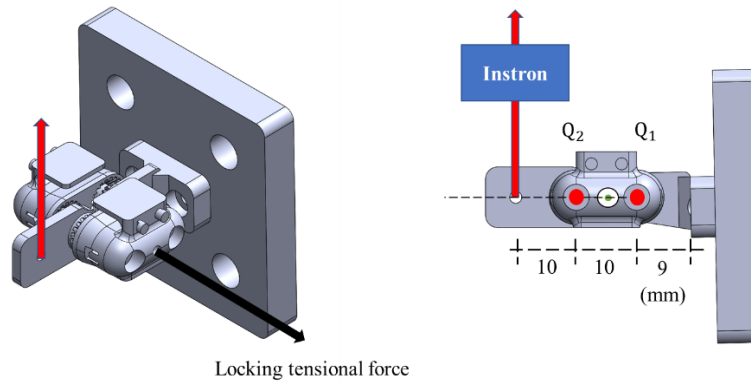


Figure 4.19: Locking mechanism force test setup. One locking module is set up horizontally on the test platform; the red line indicates the Instron force, and the black line indicates locking tensional force by Bowden cable.

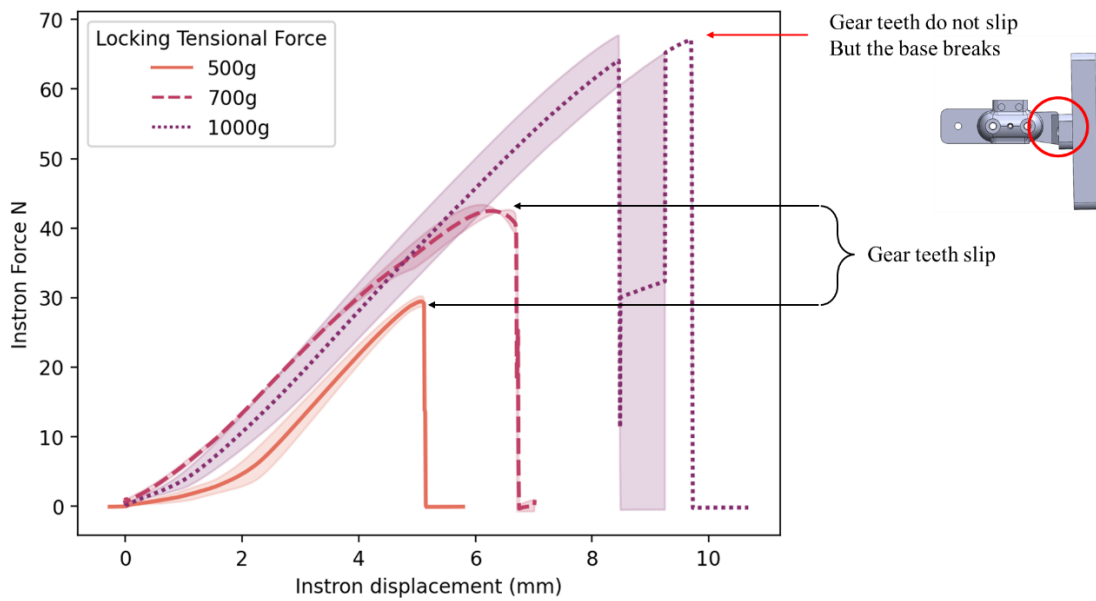


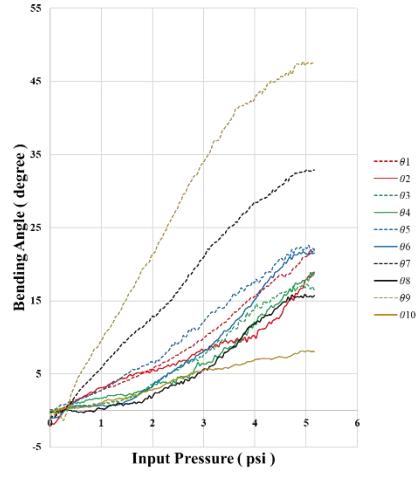
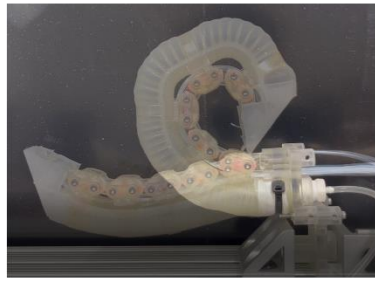
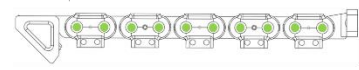
Figure 4.20: Locking mechanism force test and results of the Instron force and locking tensional force relationship.

4.3.4 Multi Curvature Bending Test

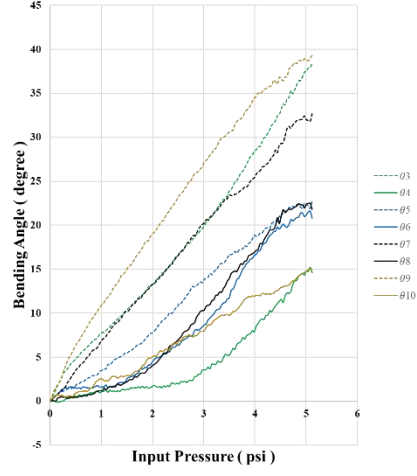
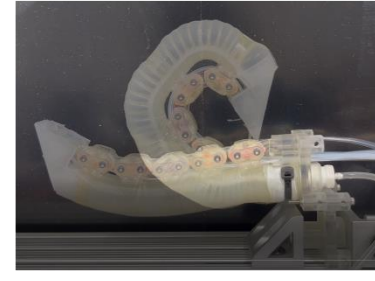
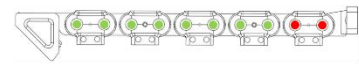
In this section, we measured the difference between the multi-curvature bending by different locking module combinations under the same pressure. Experiments were performed by repeatedly applying 0 to 35 kPa (5.1 Psi) air to the finger. A camera was used to follow each joint for motion tracking. The finger was controlled by five independently controllable locking modules to control 10 rotation joints so that a total of $2^5=32$ different control combinations were generated (0 to 31). In order to express each combination systematically, we use the decimal system to convert the binary system to represent the state of the locking modules. The first digit of the binary system represents the state of the first locking module (LM_1) to the fifth digit of the binary system represents the state of the fifth locking module (LM_5). Here we use the number 0 for unlocked and the number 1 for locked, where the combination of index 31 (decimal) = 11111 (binary) means all locking modules are locked, so we do not discuss it here.

The upper left corner of each figure shows the locking module setting status and index of the finger; the green dots represent unlocked, and the red dots represent locked. The lower-left corner of the figure shows the actual bending trajectory of the finger, and the right side of the figure shows the bending angle of each joint in relation to the input pressure. We use the same color line to represent the control by the same locking module, the dotted line represents the odd angle, and the solid line represents the even angle.

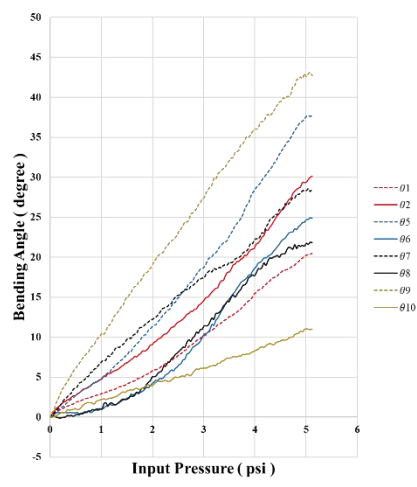
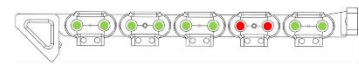
Index	LM_5	LM_4	LM_3	LM_2	LM_1
# 0	0	0	0	0	0



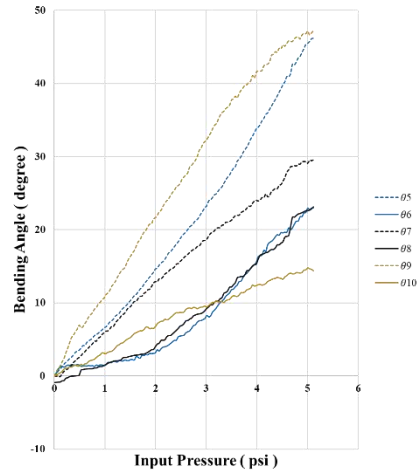
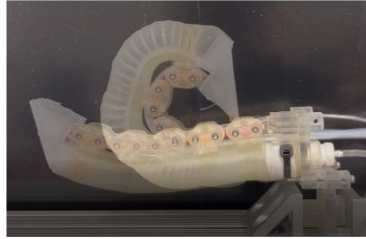
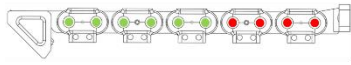
Index	LM_5	LM_4	LM_3	LM_2	LM_1
# 1	0	0	0	0	1



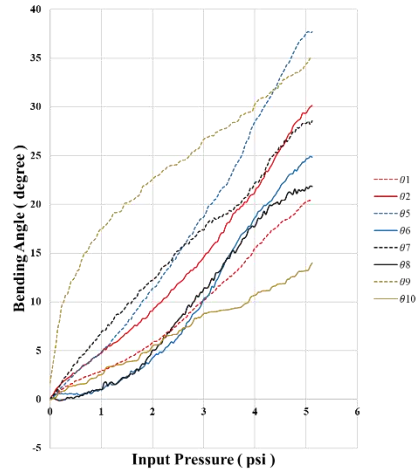
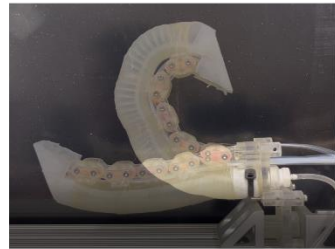
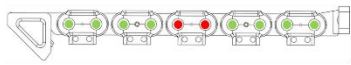
Index	LM_5	LM_4	LM_3	LM_2	LM_1
# 2	0	0	0	1	0



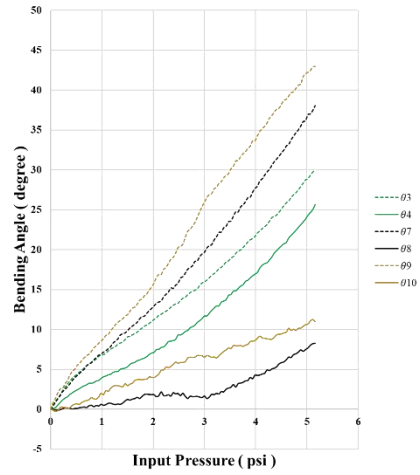
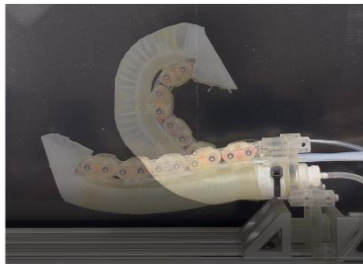
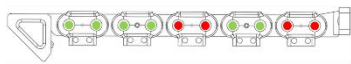
Index	LM_5	LM_4	LM_3	LM_2	LM_1
# 3	0	0	0	1	1
Decimal	Binary				



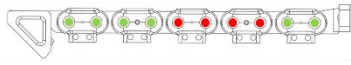
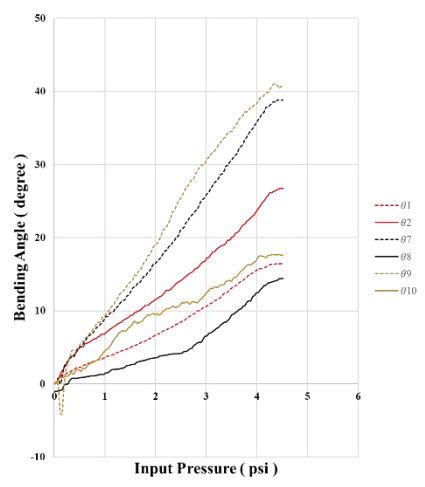
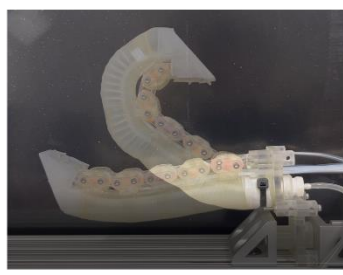
Index	LM_5	LM_4	LM_3	LM_2	LM_1
# 4	0	0	1	0	0
Decimal	Binary				



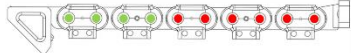
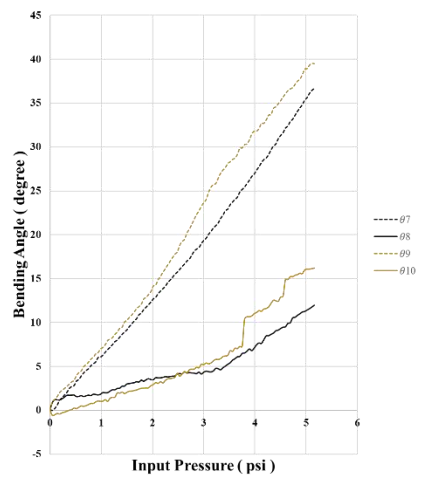
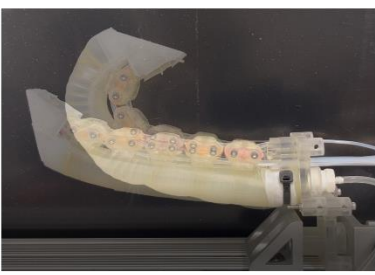
Index	LM_5	LM_4	LM_3	LM_2	LM_1
# 5	0	0	1	0	1
Decimal	Binary				



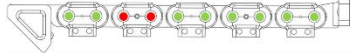
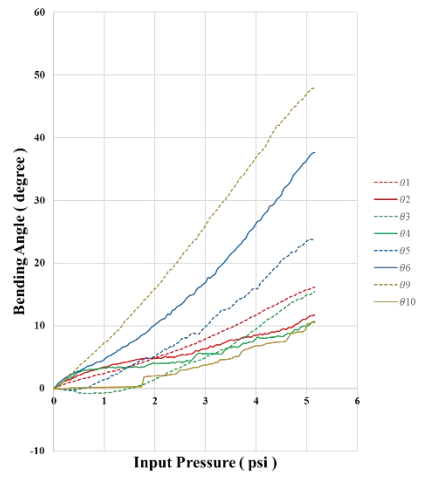
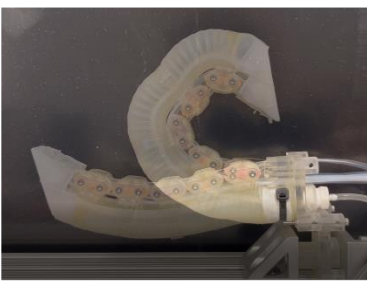
Index	LM_5	LM_4	LM_3	LM_2	LM_1
# 6	0	0	1	1	0
Decimal	Binary				

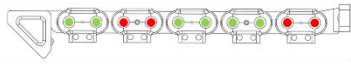
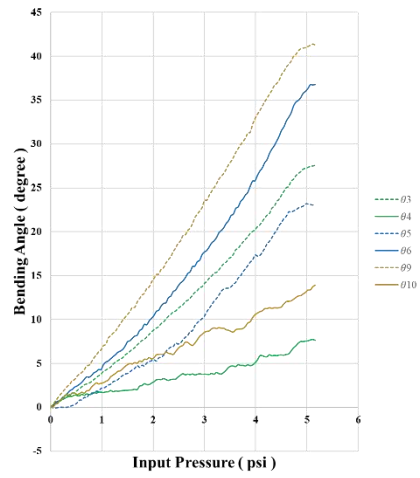
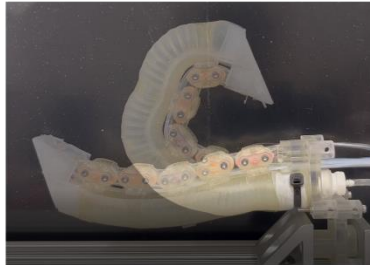
Index	LM_5	LM_4	LM_3	LM_2	LM_1
# 7	0	0	1	1	1
Decimal	Binary				

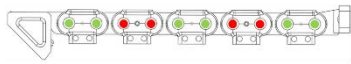
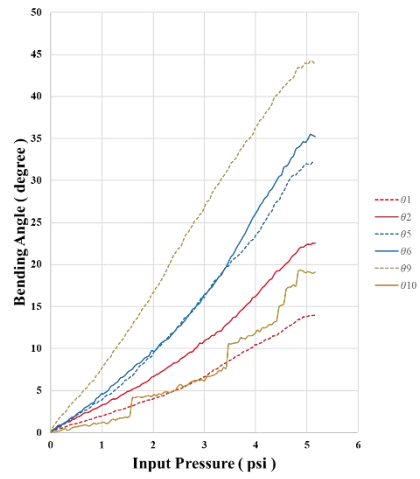
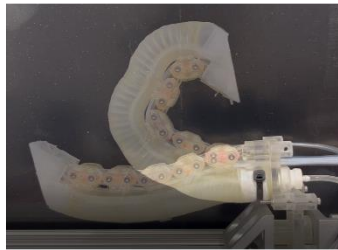
Index	LM_5	LM_4	LM_3	LM_2	LM_1
# 8	0	1	0	0	0
Decimal	Binary				

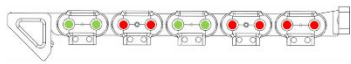
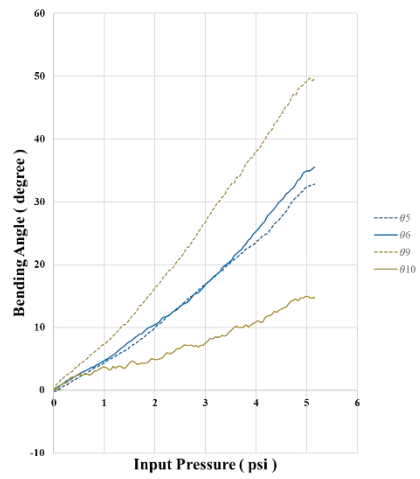
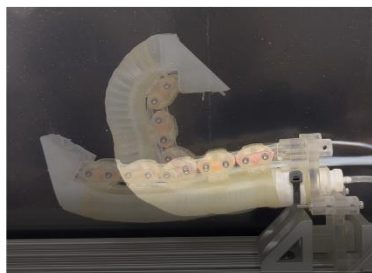
Index	LM_5	LM_4	LM_3	LM_2	LM_1
# 9	0	1	0	0	1
Decimal	Binary				

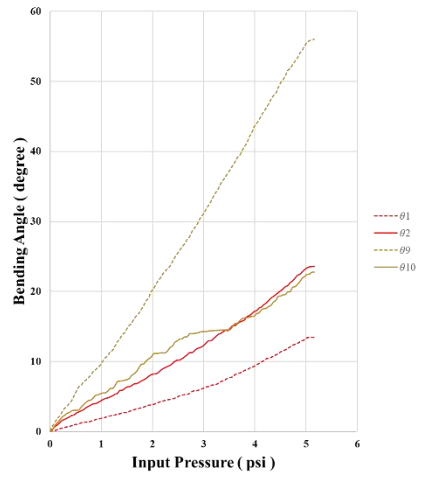
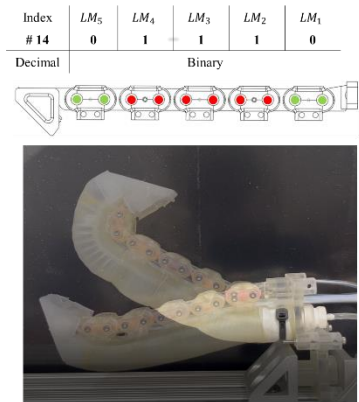
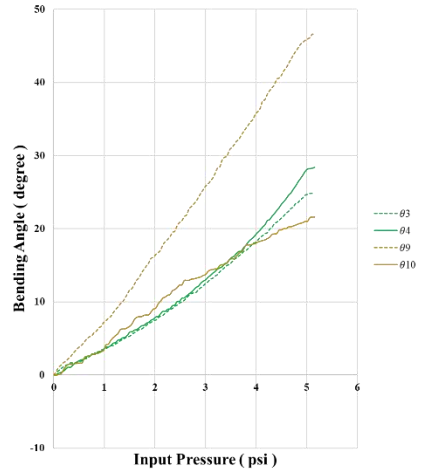
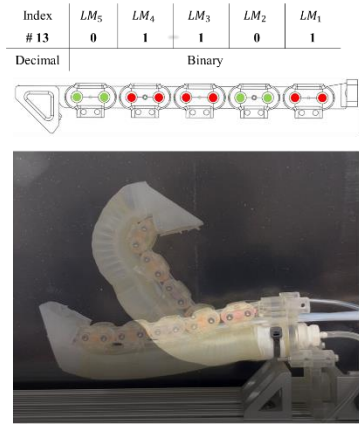
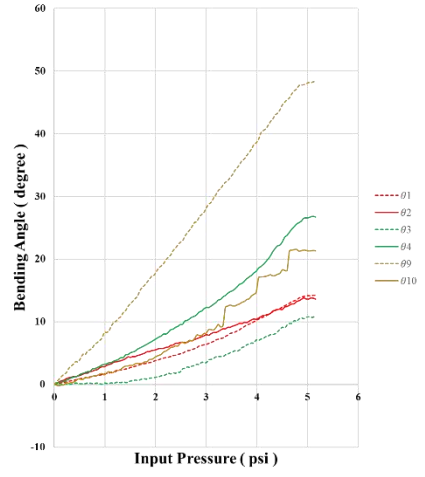
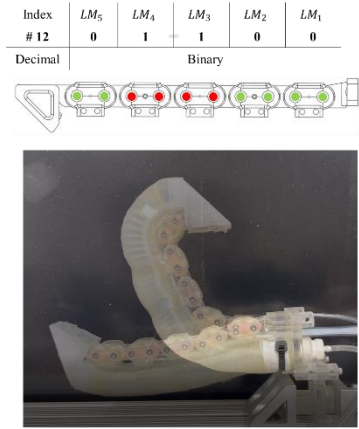



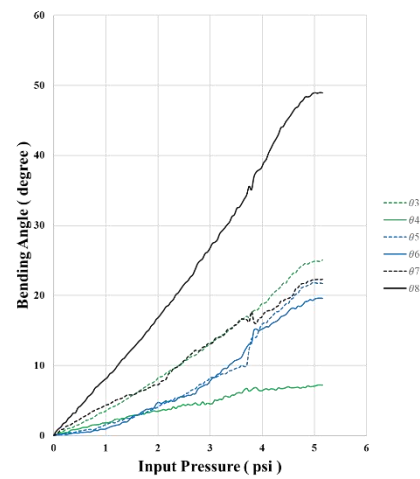
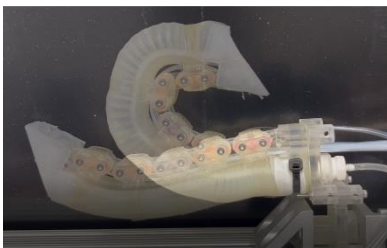
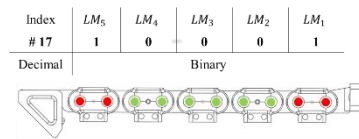
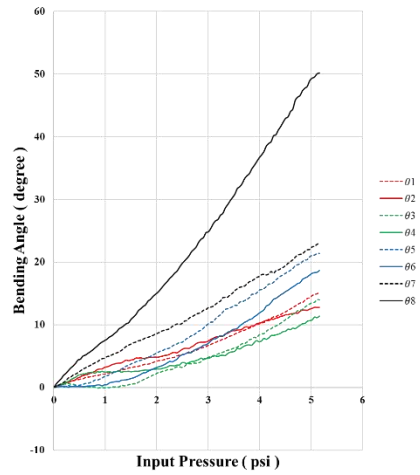
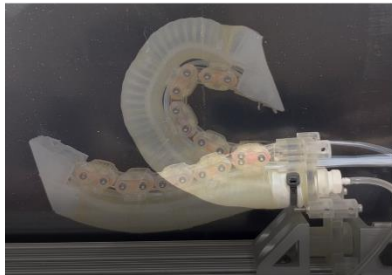
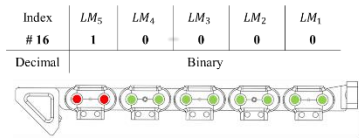
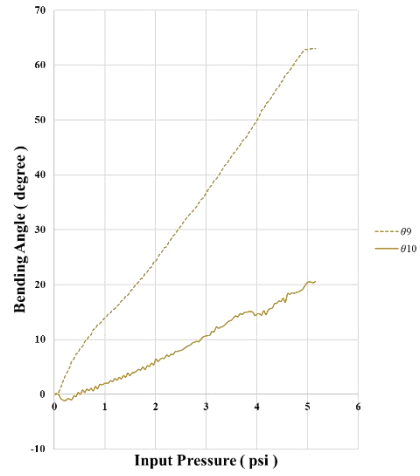
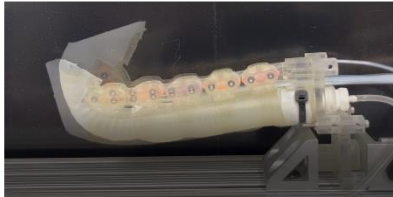
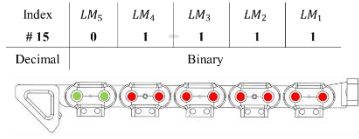
Index	LM_5	LM_4	LM_3	LM_2	LM_1
# 10	0	1	0	1	0
Decimal	Binary				

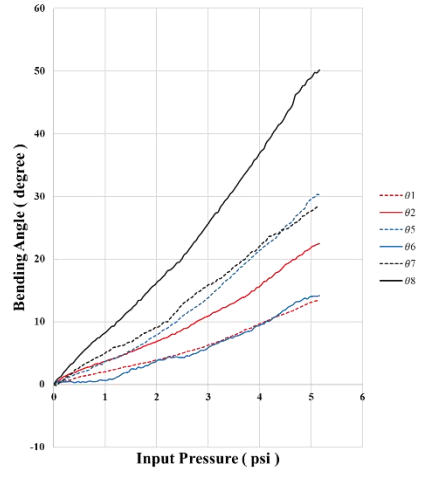
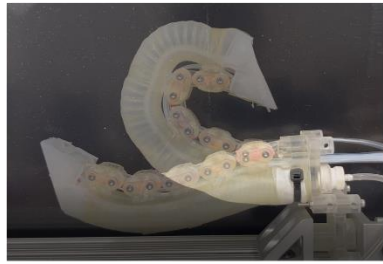
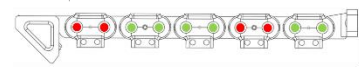
Index	LM_5	LM_4	LM_3	LM_2	LM_1
# 11	0	1	0	1	1
Decimal	Binary				

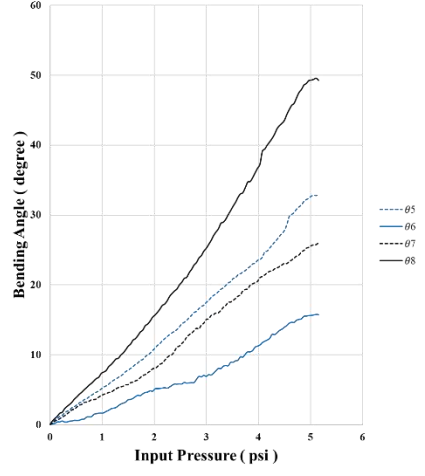
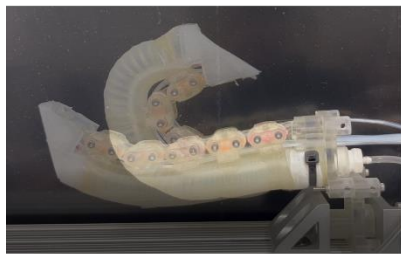
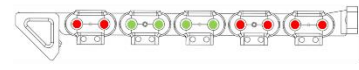




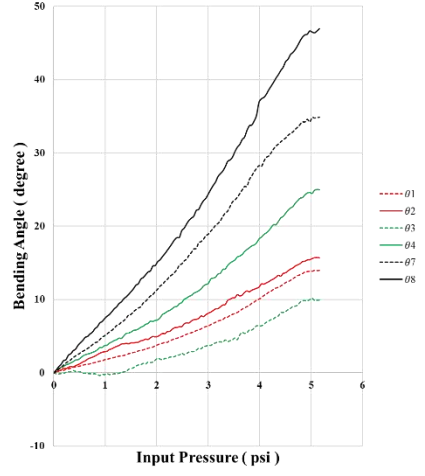
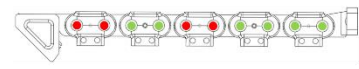
Index	LM_5	LM_4	LM_3	LM_2	LM_1
# 18	1	0	0	1	0



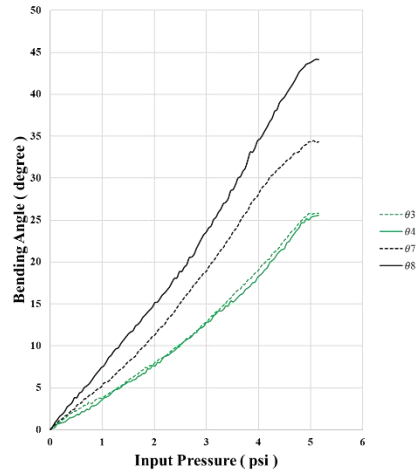
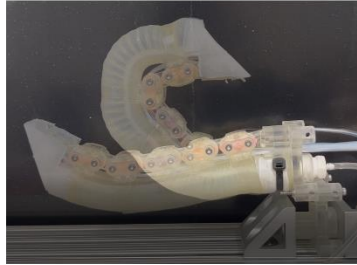
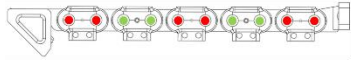
Index	LM_5	LM_4	LM_3	LM_2	LM_1
# 19	1	0	0	1	1



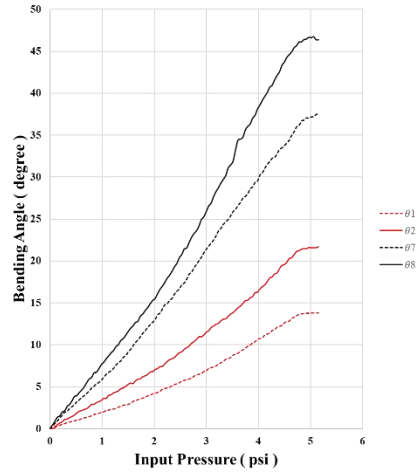
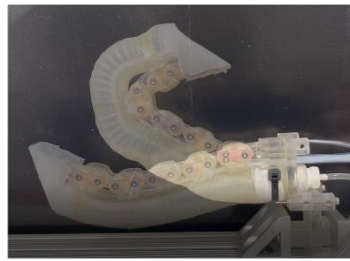
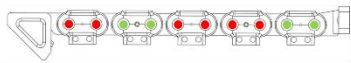
Index	LM_5	LM_4	LM_3	LM_2	LM_1
# 20	1	0	1	0	0



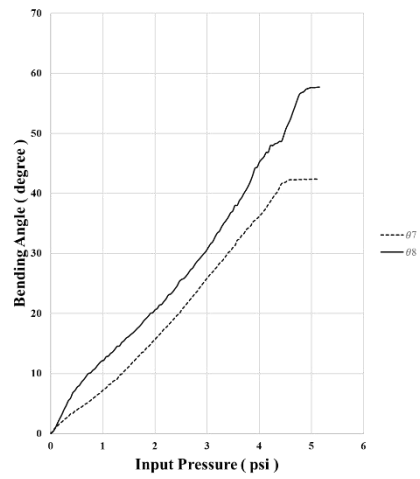
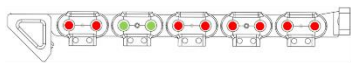
Index	LM_5	LM_4	LM_3	LM_2	LM_1
# 21	1	0	1	0	1
Decimal	Binary				



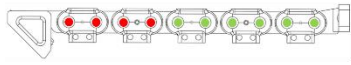
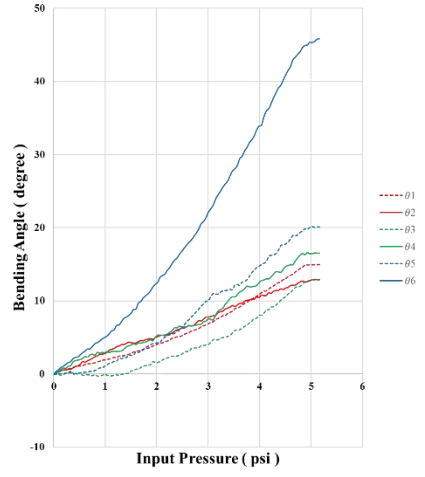
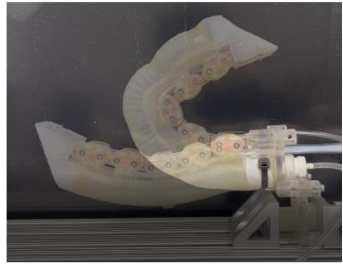
Index	LM_5	LM_4	LM_3	LM_2	LM_1
# 22	1	0	1	1	0
Decimal	Binary				



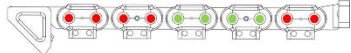
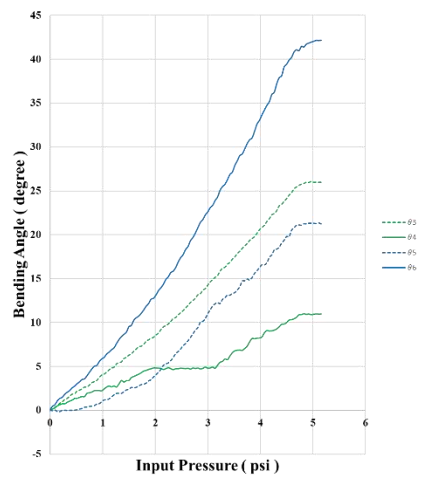
Index	LM_5	LM_4	LM_3	LM_2	LM_1
# 23	1	0	1	1	1
Decimal	Binary				



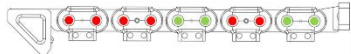
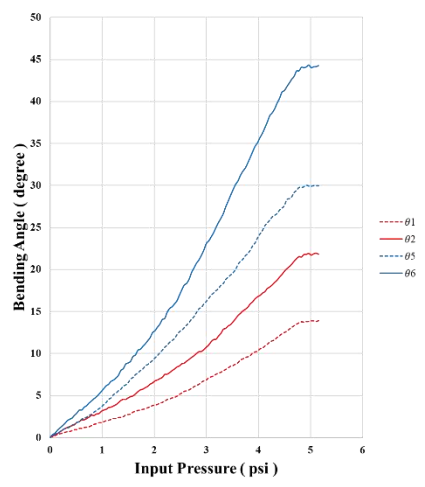
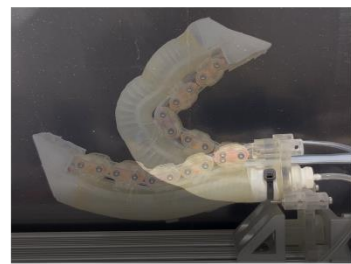
Index	LM_5	LM_4	LM_3	LM_2	LM_1
# 24	1	1	0	0	0
Decimal	Binary				

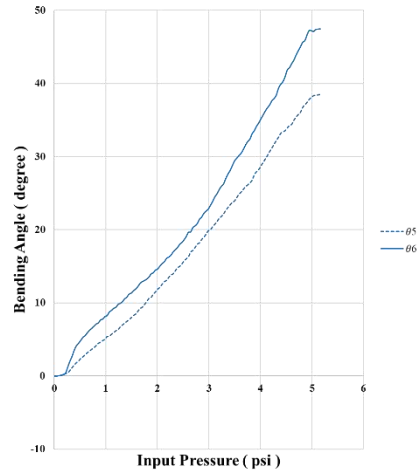
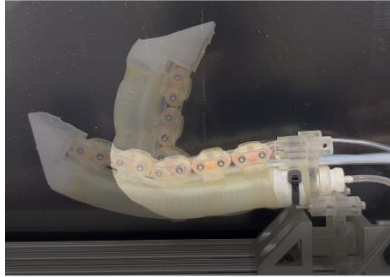
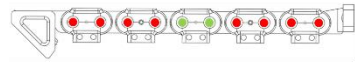
Index	LM_5	LM_4	LM_3	LM_2	LM_1
# 25	1	1	0	0	1
Decimal	Binary				

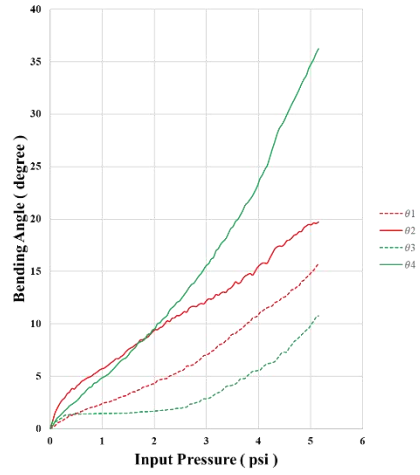
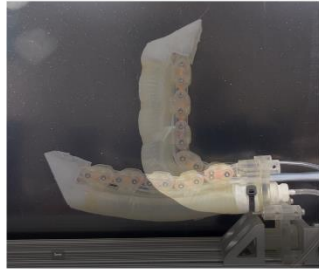
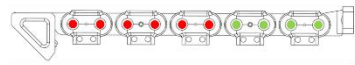
Index	LM_5	LM_4	LM_3	LM_2	LM_1
# 26	1	1	0	1	0
Decimal	Binary				

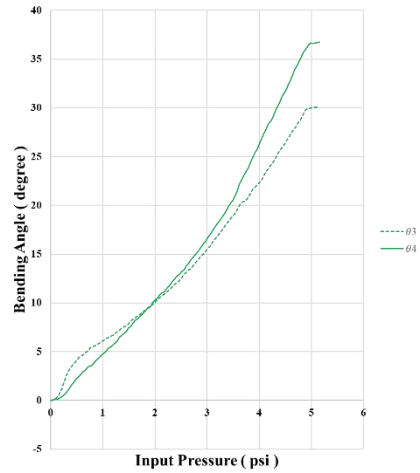
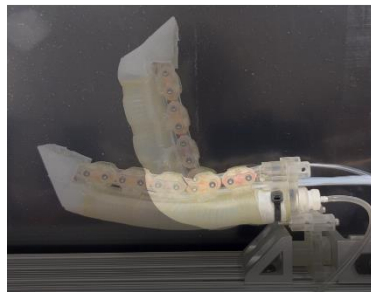
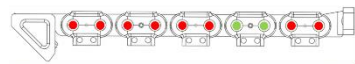
Index	LM_5	LM_4	LM_3	LM_2	LM_1
# 27	1	1	0	1	1
Decimal	Binary				



Index	LM_5	LM_4	LM_3	LM_2	LM_1
# 28	1	1	1	0	0
Decimal	Binary				



Index	LM_5	LM_4	LM_3	LM_2	LM_1
# 29	1	1	1	0	1
Decimal	Binary				



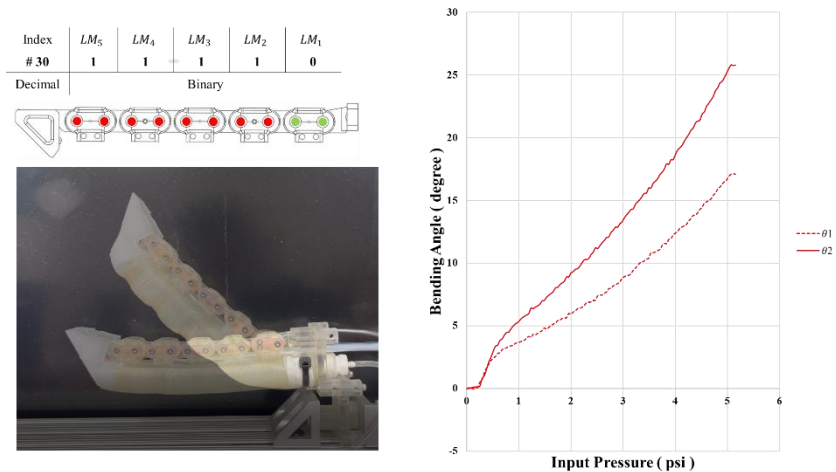


Figure 4.21: Multi curvature bending test results with 0-30 index mode.

4.3.5 Grasping Capability

First, to evaluate the general grasping ability of the fingers, we tested them with a variety of objects. In Figure 4.22, we can see that we tested the grasping ability on a dozen of different objects. The grasping of some of these objects can also be seen in Figure 4.24. During the experiments, each object was placed at a known location and then attempted to be grasped by the fingers mounted on the Sawyer robot as shown in Figure 4.23. In this set of experiments, our goal is to focus on the grasping ability of fingers, so we arbitrarily implement different grasping strategies for different objects. Some objects were grasped by whole finger envelopes, while others were grasped by top grasping, pinching with two or three fingers. Other objects such as flat objects or smaller objects such as student id card, coins, and nuts. We use the nail mechanism at the front of the fingers to help grip, as shown in Figure 4.25. The experimental results

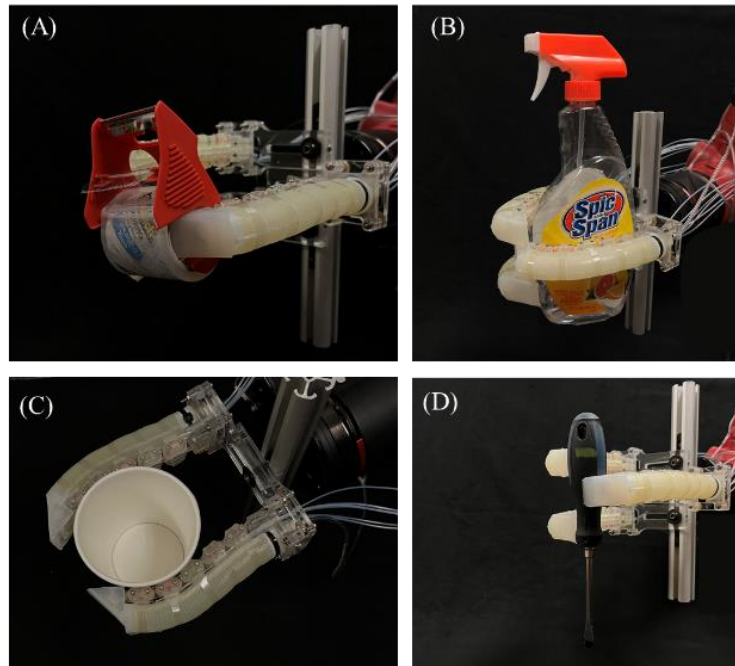


Figure 4.24: Various objects grasped by the fingers. (A) Packaging tape, (B) Spray cleaner, (C) Paper cup, (D) Screwdriver.

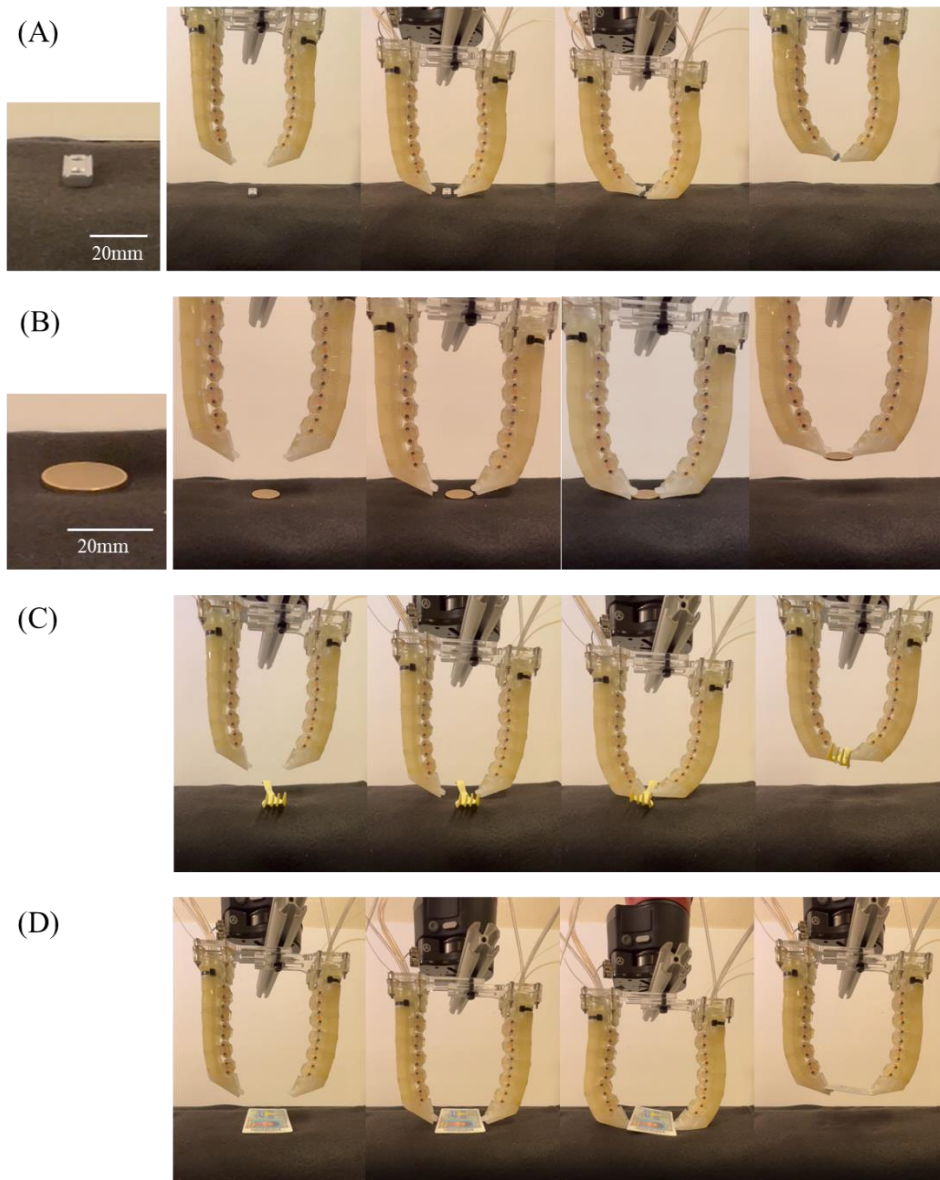


Figure 4.25: Finger in the pre-shaped mode for gripping flat objects and smaller objects. (A) Nut, (B) coin, (C) fork, (D) student id card.

We also tested the gripping ability of the finger in the soft-rigid hybrid mode. Figure 4.25 shows that we used the pre-shaped mode with the nail mechanism on the front of the finger to allow the finger to grip flat objects or smaller objects. The pre-shaped mode allows us to know the bending trajectory of the finger in advance so that

we can better control the gripping distance and then be more precise in small gripping objects. Figure 4.26 shows the use of the pre-shaped mode to grip the sponge and then apply the additional tendon-driven actuator to it for more force to the sponge to bend it.

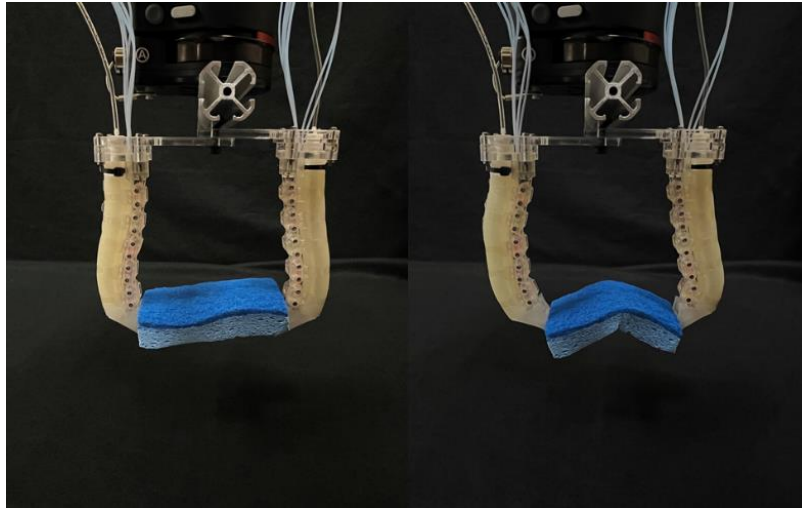


Figure 4.26: The use of the pre-shaped mode to grip the sponge and then apply the additional tendon-driven actuator to it for more force to the sponge to bend it.

We used the paper cup to demonstrate finger grasping in adaptive power mode. During the experiment, the paper cup was placed in a known position and then grasped by Sawyer robots using two fingers. After gripping the paper cup, the finger could quickly adapt to the shape of the paper cup and adjust the curvature of the grip. Then we locked the 2nd to 5th locking modules (LM_{2-5}) so that only joints Q_1 and Q_2 were left for the fingers to rotate. Now apply the tendon-driven actuator to provide additional torque. This allows the fingers to output force in the direction of the center, causing the paper cup to be squashed, as shown in Figure 4.27.

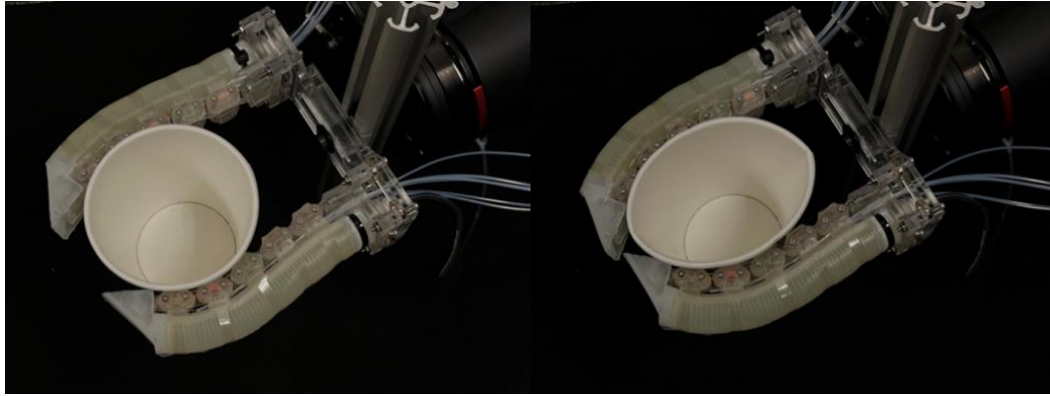


Figure 4.27: Finger grasping in adaptive power mode with applying the tendon-driven actuator to provide additional force to squash paper cup.

4.3.6 Grasping Performance

To further compare the grasping ability of the finger under different actuators, an experiment was conducted to compare the maximum grasping force of pneumatic driven only mode and pneumatic & cable-driven mode. First, a cylindrical rod with a diameter of 20 mm was mounted on the Instron tensile tester, and a finger was fixed on the plane of the Instron to perform a gripping action on the cylindrical rod. To measure the gripping force of the finger on the cylindrical rod during the upward movement, the locking modules of the finger were all in the unlocked state, as shown in Figure 4.28. Then, the cylindrical rod moves upward without interruption. From grasping the rod to disengaging it, the vertical displacement of the cylindrical rod is about 43mm, and the vertical pulling force generated by the finger is shown in Figure 4.28. During the pulling process, it is worth noting that in the two driving modes, the pulling force undergoes a smooth increase process until the vertical displacement of the cylindrical rod exceeds 38mm, and then suddenly drops. The results show that the maximum

grasping forces of pneumatic driven only and pneumatic & cable-driven are 5.5 N and 10.8 N, respectively, corresponding to a ratio of 1.96 times.

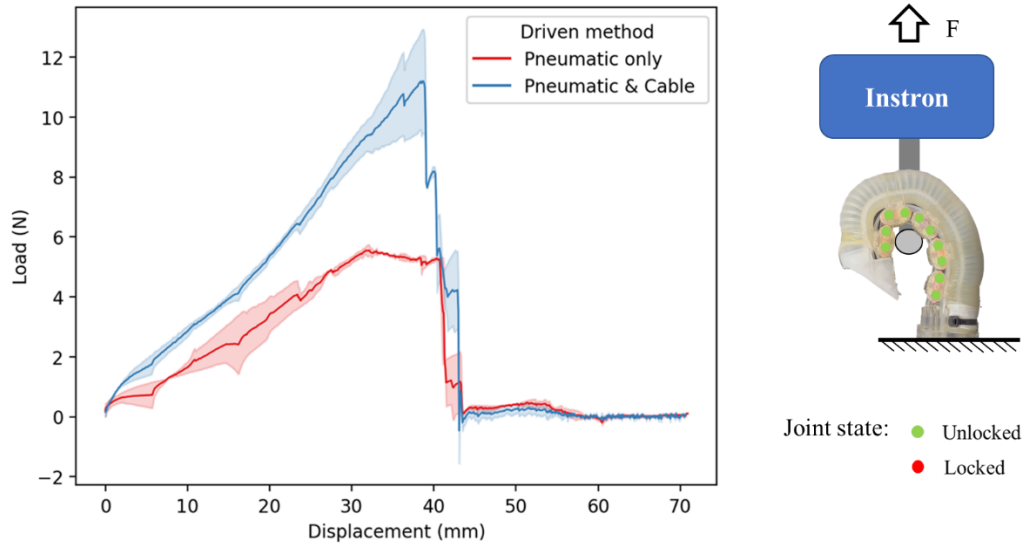


Figure 4.28: Grasping performance. Gripping force of the finger in pneumatic driven only mode and pneumatic & cable-driven mode.

Then we conducted the experiment on the maximum grasping force of the finger when all the locking modules are locked. The same setup as the previous experiment was used here, where a finger was fixed on the plane of the Instron to make the finger grasp the cylindrical rod. The difference is that after the finger grasps the cylindrical rod, all the locking modules are changed from unlocked to locked. Then, the cylindrical rod is moved upward without interruption to measure the gripping force generated by the finger. The vertical pulling force generated is shown in Figure 4.29. During the pulling process, the pulling force experiences a gradual increase process at the beginning until the vertical displacement of the cylindrical rod exceeds 8mm, and

then the pulling force rises sharply. Until the vertical displacement of the cylindrical rod exceeds 16 mm, the chain core in the third locking module (LM_3) of the finger is fractured. The result shows that when all locking modules are locked, the maximum grasping force is 125 N. This result compares with the previous maximum grasping force of pneumatic & cable-driven of 10.8N, and the corresponding ratio is 11.57 times.

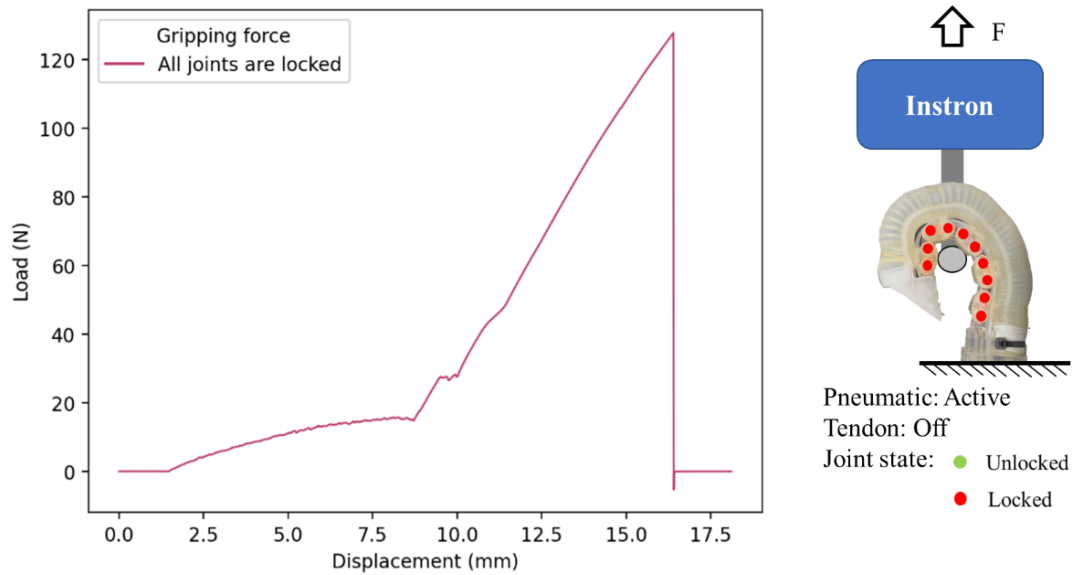


Figure 4.29: Grasping performance. Grasping force of the finger with all the locking modules are locked.

Table 4.9 Compare maximum grasping force in three different modes

Grasping mode	Maximum grasping force (N)
Pneumatic only	5.5
Pneumatic & cable	10.8
Pneumatic & all modules locked	125

4.3.7 Durability Test

We perform a cycle test to study the durability of the finger in this section. We set all locking modules to be unlocked and perform 100 cycles of inflation and deflation on the pneumatic actuator. For the cyclic test, we set the maximum pressure to 35 kPa (5.1 Psi) and the drive frequency to 0.1 Hz. We used a 30 Hz sampling rate vision camera to perform motion tracking on the 10th joint and recorded the complete trajectory (yellow dots in Figure 4.30A). The orange line in Figure 4.30B represents the average trajectory for the 1st to 5th cycles, and the blue line represents the average trajectory for the 95th to 100th cycles. After 100 cycles, the 10th joint has a deviation of $0.57 \pm 0.22\text{mm}$ in the x-direction and $3.15 \pm 0.19\text{mm}$ in the y-direction.

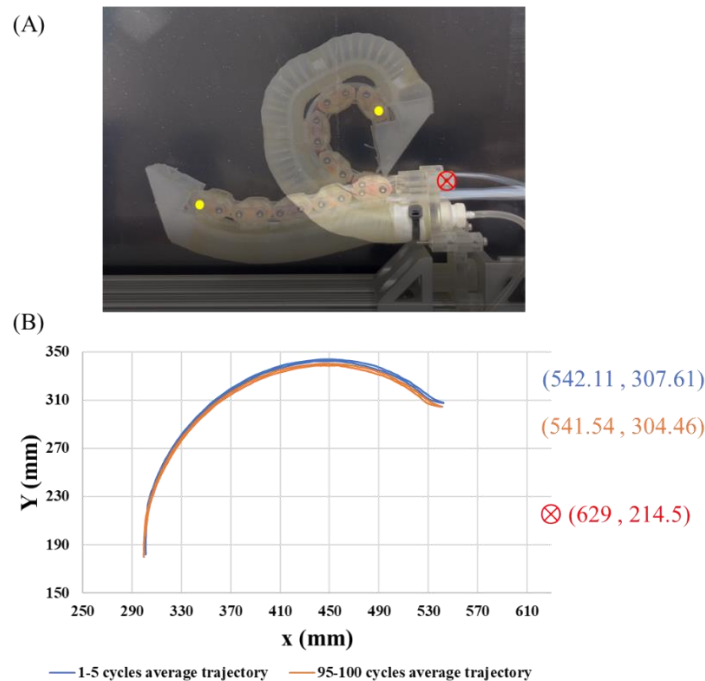


Figure 4.30: Durability test results. The orange line represents the average trajectory for the 1st to 5th cycles, and the blue line represents the average trajectory for the 95th to 100th cycles. The red marked point represents the reference point of Figure A.

4.3.8 Tensile Tests of SLA 3D-printed Material

To create our rigid components in this study, we used Stereolithography (SLA) 3D printing technology. The mechanical properties and characterization of SLA 3D-printed material must be understood. Stereolithography, created in the 1980s and is now one of the most popular technologies among experts, was the world's first 3D printing technique [137]. SLA resin 3D printers employ a laser to cure liquid resin into rigid plastic in photopolymerization. Of all the plastic 3D printing processes, SLA components feature the best resolution and precision, the most accurate details, and the finest surface finish selections available on the 3D printer. Still, the fundamental advantage of SLA is its adaptability. SLA photopolymer resin compositions with a wide variety of optical, mechanical, and thermal qualities that match those of standard, engineering, and industrial thermoplastics have been developed by material makers. Sharp edges, a flawless surface finish, and little visible layer lines characterize SLA products. Because of the highly detailed prototypes that require tight tolerances and smooth surfaces, SLA is a fantastic option for our stiff parts in this project.

In this section, we performed tensile tests on Formlabs Clear V4 resin (Formlabs, Somerville, MA, USA) specimen with an Instron 5943 tensile tester (Instron Co., Norwood, MA, USA), and we compared the results with the manufacturer's datasheet. Tensile tests were carried out according to the sample geometry given in Figure 4.31. Specimens were 3D printed using Clear V4 resin on a

Formlabs Form 3 SLA 3D printer. The layer thickness was set to 50 μ m and used PreForm slicer software with Beta print settings.

To test the hypotheses of isotropy, specimens were printed at different orientations, with β_p varying in 0°, 45°, and 90°, where β_p is defined as the angle between the specimen's axis and the horizontal direction (x-axis), as illustrated in Figure 4.32. Two specimens were printed at each orientation in a single print, totaling six samples. All samples were cleaned in IPA alcohol for 20 minutes before being post-cured under 405 nm UV light with 1.25 mW/cm² in Form Cure for 60 minutes at 60°C, the same as our rigid parts process in this project.

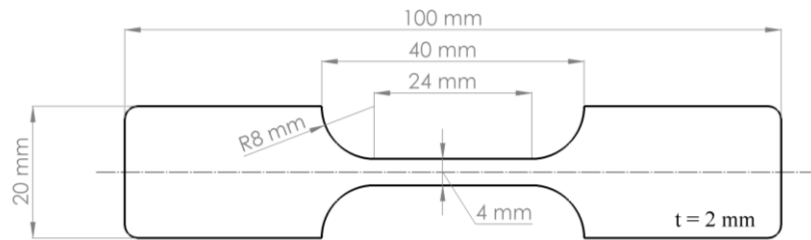


Figure 4.31: The geometry of the tensile test's specimen.

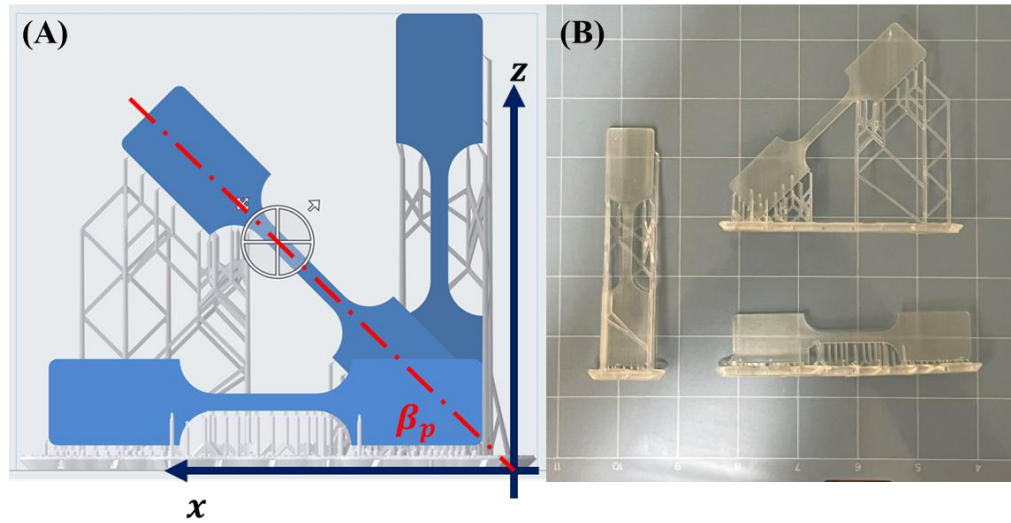


Figure 4.32. (A) CAD file in PreForm slicer software; (B) SLA 3D printed specimens after post-cured.

Stress-Strain Diagram and Results

Each test specimen was placed in the Instron tensile tester, with the two ends secured to the upper and lower grips. The grips were moved apart, elongating the specimen until failure. During this procedure, the gauge section's elongation is measured against the applied force. Using the following equation, we can use force measurement to get the engineering stress σ :

$$\sigma = \frac{P}{A} \quad (4.27)$$

where σ is the engineering stress, P is the applied force, and A is the specimen cross-section area. The elongation measurement can let us get the engineering strain ε :

$$\varepsilon = \frac{\Delta L}{L_0} = \frac{L-L_0}{L_0} \quad (4.28)$$

where ΔL is the change in gauge length, L_0 is the initial gauge length, and L is the final length. Taking ϵ as the abscissa and σ as the ordinate, we can obtain the stress-strain diagram in Figure 4.33. The ultimate tensile strength and the elongation at failure are calculated for each sample and shown in Figure 4.34.

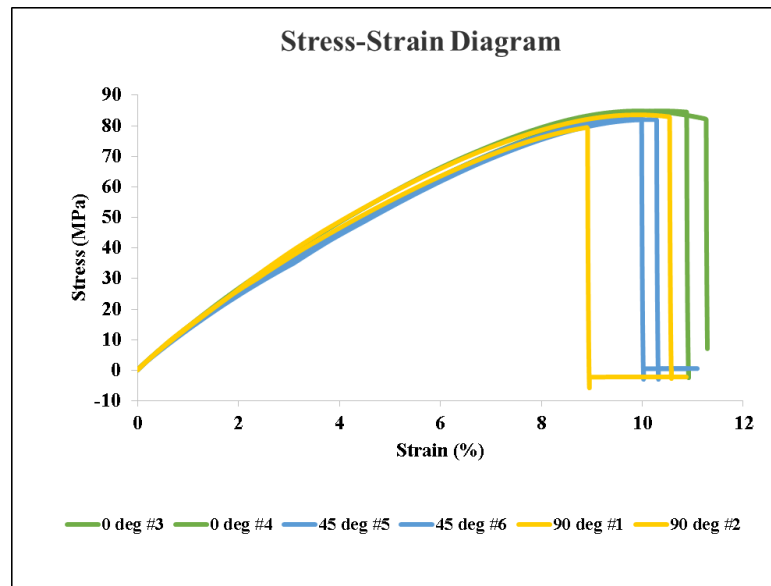


Figure 4.33: Stress-strain diagram for the six tested samples grouped by construction angle in color.

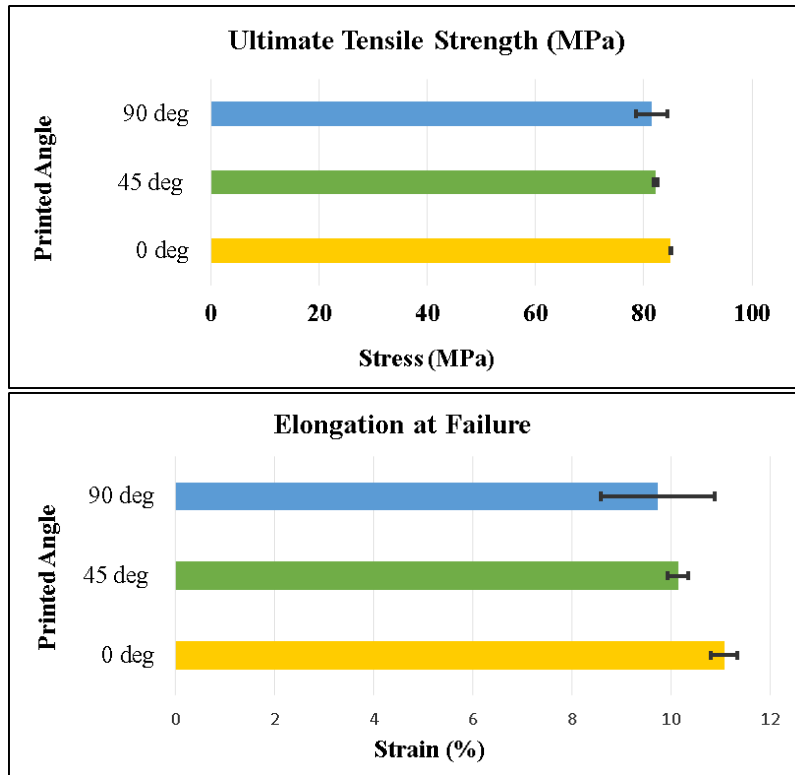


Figure 4.34: Mean characteristics for each printed angle with error bars \pm Std. Dev.

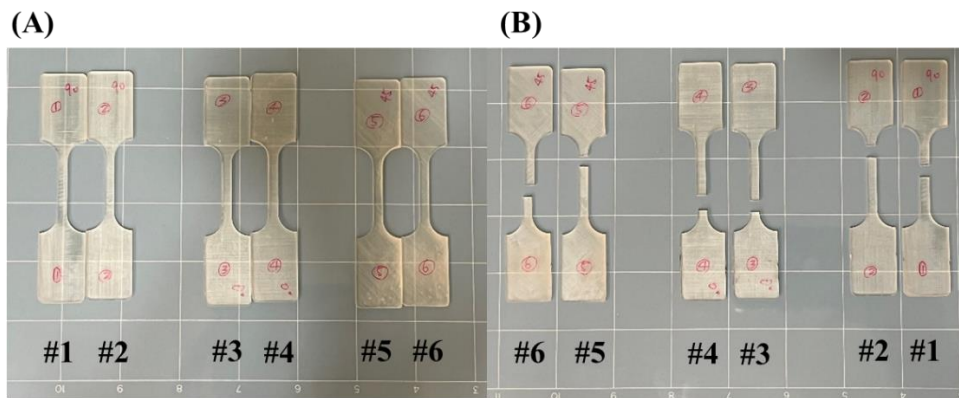


Figure 4.35: The Clean V4 resin tensile specimens; (A) Before testing, (B) after testing.

Table 4.10 Formlab Clear V4 resin datasheet comparison with our experiment.

	Ultimate Tensile Strength (MPa)	Elongation at Failure (%)
Formlabs resin datasheet[138]	65	6
Our experiment data	82.88	10.31

Note: Formlab's data was obtained from parts printed using Form 2, 100 μm , Clear settings, and post-cured with 1.25 mW/cm^2 of 405 nm LED light for 60 minutes at 60 $^\circ\text{C}$. Our experiment is different by using Form 3 and 50 μm .

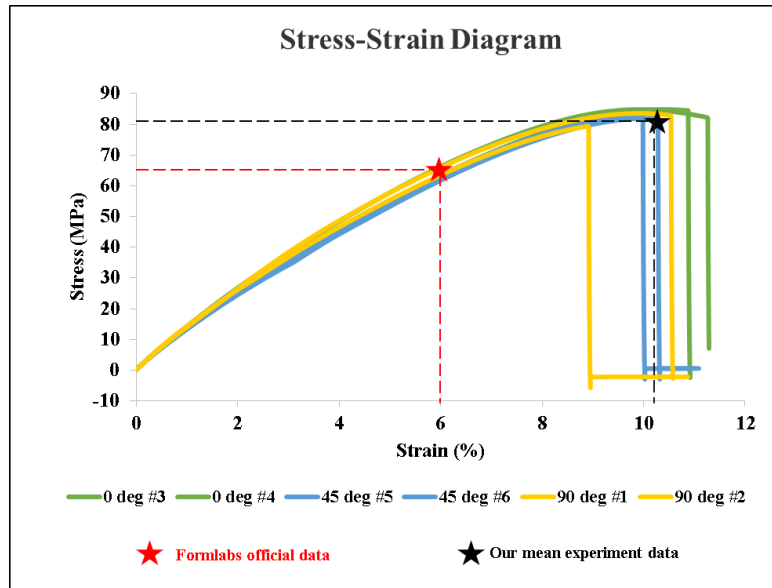


Figure 4.36: Stress-strain diagram for the Formlabs Clear V4 resin mechanical characteristics comparison.

The results obtained in this tensile test are consistent with the Formlabs Materials Library reported datasheet [138]. Table 4.10. and Figure 4.36. summarize the overall data for the material attributes. These are compared to the specifications listed on the manufacturer's datasheet. The total observed average tensile strength is somewhat greater than that claimed by Formlabs (82.88 and 65 MPa, respectively),

although the discrepancy is minor and might be related to differences in the 3D printer model, the layer thickness, and ambient circumstances. Overall, there is no indication that the mechanical qualities assessed are connected to the printing angle; therefore, this work just supports what has already been established in the literature [139], [140].

4.4 Discussion and Conclusion

This work proposes a soft-rigid hybrid structure design method for the interactive use of pneumatic and tendon-driven actuators and analyzes and implements a bioinspired soft finger prototype. The newly developed segmented controllable locked and unlocked module combines the advantages of the soft robotic gripper and the rigid robotic gripper. The bioinspired soft finger contains a locking mechanism underneath. The locking mechanism is composed of 5 independently controllable (locked or unlocked) locking modules in series; each module can provide 2 DOF on bending, so the finger has a total of 10 DOF. The finger can have a multi-curvature gripping mode, which can adapt to the shape of the gripping object. With the pneumatic actuator on top, it can achieve fast actuation and complete the task without complicated sensor and feedback control. These advantages are the same as the soft robotic gripper. We use SLA 3D printing to make rigid locking modules, and a tendon-driven cable is embedded in the locking mechanism to provide more force. When rigid locking modules are locked, it can increase the grasp force of fingers, which has a similar performance to the traditional rigid gripper. By independently controlling the locking modules (locked or unlocked) status and the use of two actuators, it can provide force

in specific directions. In addition, we added a nail mechanism to the front of the finger, and from the results of the experiment, we can see that this mechanism allows the bioinspired soft finger to provide additional assistance when gripping flat or tiny objects.

We analyze the mechanical model of a single locking module to the overall kinematic analysis and also analyze the combination of each locking module used with the actuator. This includes pure soft mode, soft-rigid hybrid mode, and rigid mode to validate our model from experimental data. In the grasping performance test, we verified that this soft-rigid hybrid structure of the bioinspired soft finger could provide a maximum gripping force of 125N with a single finger when all locking modules are locked. We used paper cups and sponges in the experiment to demonstrate that the finger can quickly adapt to the shape of the gripping object, adjust the gripping arc, and deliver force in a specific direction.

From the kinematic analysis to the experimental results, we believe that the method of soft-rigid hybrid structural design interacting with multiple actuators provides a scalable and adaptable design framework for future bioinspired fingers. In this study, we focused on a bioinspired soft finger with in-plane motion and established different grasping modes. In the future, we can generalize the same concept and design to 3D motion and control manipulators and add embedded sensors and appropriate controls for more applications.

Chapter 5

A Normally Open Passive Microfluidic Valve

5.1 Introduction

Microfluidic systems have attracted much interest over the past two decades. Microfluidic chips play an increasingly important role in biology, chemistry, medicine, and other fields due to their small size [141]–[144], strong functions, high efficiency, easy integration, and low price. In the past decade, with the rapid development of the soft robotics field, microfluidic systems have also started to be used in the soft robotics field because of their own characteristics [16], [17], [96], [145]–[147]. Microfluidic chips use Micro-electromechanical systems (MEMS) technology [148] to fabricate various microfluidic functional devices, such as micro-pumps, micro-valves, micro-fluidic channels, micro-actuator, etc., on glass, Polydimethylsiloxane (PDMS), Polymethyl methacrylate (PMMA), etc., to control micro-fluidic motion to achieve certain biochemical analysis functions. Some actions that must be performed in the laboratory can now be done on a microfluidic chip, such as sampling, reaction, separation, etc. Even the detector can be integrated into the microfluidic chip, so it is called "lab-on-a-chip" [149], [150]. The core of microfluidic technology is to drive and control the fluid in the microfluidic channel of the chip so as to complete various liquid

flow operations required for biological and chemical reactions and analyses. Therefore, the driving and control technology of microfluidic chips is the premise and foundation of microfluidic technology, and microvalve control is an important control method of microfluidic technology.

The microfluidic valve includes passive control and active control. An active control valve requires the control of microfluidics under the action of some form of external driving energy such as: pneumatic [151], [152], electrostatic field [153], piezoelectricity [154], magnetism [155], phase change [156], heat [157], etc. The above valve control equipment, except for pneumatic membrane valves and other driving devices, are located on the top of the microfluidic chip, which affects the further integration of the microfluidic chip. The pneumatic membrane valve is small in size, and the control and drive system is located outside the chip, so it has been widely used in the academic field of microfluidic systems since it was proposed. A passive control valve does not require external energy input for microfluidic control. It relies on the fluid's own kinetic energy to open and close, such as the cantilever type [158], [159], membrane type [160]–[162] microvalve, etc. The valves are designed with special flow channels to achieve passive control using material properties of the mechanical structure, which has the advantage of easy fabrication and a simple structure.

In recent years researchers have started to use these microfluidic valves to build three-dimensional microfluidic chips with multiple logic Boolean functions [151], [163], [164]. Due to the small size and the use of soft materials, it can be integrated into soft robotic devices and allow computation and control in these devices without

the need for hard valves or electronics [17]. This is a good solution to the limitation that most soft robotic devices are still driven by hard valves and electronic control devices. Further, it lays the foundation for completely soft autonomous robots and automatic control strategies. Thus, the power source of the soft robot can no longer be limited to rigid components energy sources such as lithium batteries, compressed air, liquid carbon dioxide, etc. The researchers found that if we look at the energy density alone, chemical reactions can provide a higher energy density source than those energy sources with rigid components, as shown in Table 5.1.

Table 5.1 Comparison of rigid components and chemical reaction energy densities

	Fuel	Energy Density
Rigid components	LiPo Battery	360-875 J/g
	LiPo Battery and compressor	30-100 J/g
	Liquid CO ₂	220 J/g
	Compressed air 300 Bar	474 J/g
Chemical reactions	H ₂ O ₂ pure	2.8 kJ/g
	H ₂ O ₂ 50% wt.	1.4 kJ/g
	Butane	49 kJ/g
	Butane + Oxygen	17.8 kJ/g
	Methane	55.5 kJ/g
	Methane + Oxygen	18.5 kJ/g

Note: Data are from Wehner, M., et al. Soft Robotics 2014[165]

Researchers have begun to explore micro-soft internal combustion chambers so that these high-energy-density fuels can be used in soft robots [57], [58], [166], [167]. However, current micro-soft internal combustion chambers need to be connected to external controls to open and close active valves at predetermined times for the intake and exhaust. These auxiliary systems are much larger and heavier than the micro-combustion chamber itself, which minimizes their energy conversion efficiency.

Therefore, it is necessary to develop a small, time-programmable micro-valve to replace the external control of intake and exhaust.

In this study, partially inspired by previous soft robot combustion research [168] and its lack of local controllability, we develop a normally open passive microfluidic valve with reduced-order control for a micro-combustion chamber. This passive microfluidic valve can be installed on a micro-combustion chamber and is responsible for all fluid control, including intake and exhaust. In order to be controlled using a single microfluidic valve, it must meet two criteria: (1) close at high combustion pressures and (2) allow exhaust and intake at low pressures. This passive microfluidic valve has passive components that modulate the flow of liquids and gasses through channels. This valve includes a plurality of channels, a membrane, and openings configured to allow or block flow in one or both directions based on flow properties, such as flow rate and pressure state within the system. In addition, the valve is configured to either allow or block flow in the reverse direction. This novel mode of actuation allows for controlling combustion reactions at a small (e.g., millimeter) scale.

The main contribution of this chapter is the proposal of a new passive microfluidic valve with reduced-order control of intake and exhaust. Our microfluidic valve achieves a flow rate of 1 cc/s at a 1 psi input pressure in forwarding flow. It can also be blocked at 1.5 psi in reverse flow and can withstand 30 psi of reverse pressure. Section 2 presents the methods used, beginning with valve design and starting with the passive microfluidic valve three states and combustion chamber pressure hypothesis followed by fabrication, and experiment setup. Section 3 presents results, divided into

pressure test for state switched, pressure test for changing the chamber heights, flow rate test, and flow rate improvement test. Section 4 presents a discussion on the work and how it relates to the field, concluding remarks, and suggesting the future steps.

5.2 Method

5.2.1 Design

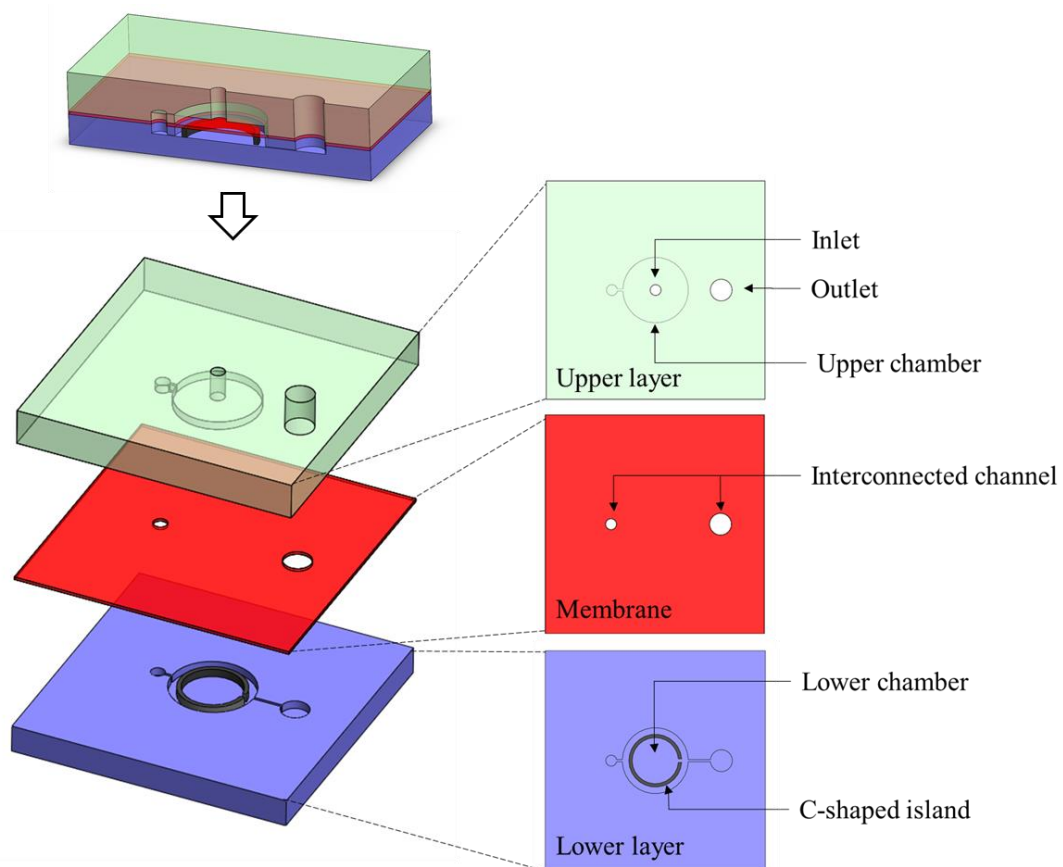


Figure 5.1: Schematic of the passive microfluidic valve design.

Based on the compliance of the PDMS, this passive micro-valve is constructed by combining two PDMS layers and a reciprocating thin PMDS membrane. Regarding

the structure of the passive micro-valve, as shown in Figure 5.1. It is mainly composed of three structural layers from top to bottom: Upper layer, Membrane, and Lower layer.

Upper layer:

The Upper layer includes one inlet, one outlet, an upper chamber, and an interconnected channel that connects the upper and lower chambers. The inlet is fluidly coupled to the upper chamber, which is also interconnected via a channel. But the outlet is fluidly separated from the upper chamber. The outlet here is a structure that extends from the lower layer. The inlet is located in the center of the upper chamber, the channel connecting the upper and lower chambers is located on the left side of the upper chamber, and the PDMS membrane is below the upper chamber. The design parameters of the upper layer are: Upper chamber height (H_{up}), Inlet diameter (ϕ_{in}), Valve diameter (ϕ_v), and Channel width (W_c).

Membrane:

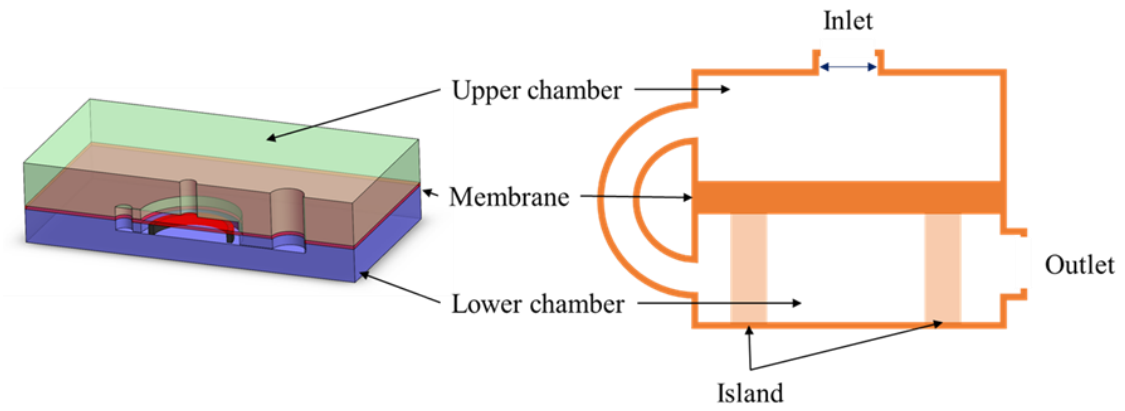
The PDMS membrane layer separates the upper and lower chambers. The upper surface of the PDMS membrane layer is bonded to the edge of the upper chamber, while the lower surface of the membrane is bonded to the inner C-shaped island edge of the lower chamber. The membrane located in the interconnected channel and outlet channel is penetrated, allowing the fluid to pass through. When the pressure of the upper and lower chambers is different, the membrane will be deformed. When the pressure of the upper chamber is greater than the lower chamber, the membrane will be pushed downward. On the contrary, when the pressure of the lower chamber is greater

than the upper chamber, the membrane will be pushed upwards and block the inlet. The design parameter here is membrane thickness (M).

Lower layer:

The lower layer includes one C-shaped island and two interconnected channels which connect the upper chamber, and the other one connects to the outlet and extends to the upper layer. The C-shaped island opening faces the outlet. The diameter of the C-shaped island is smaller than that of the lower chamber, and there are channels on both sides of the C-shaped island for the fluid to flow through. When the fluid flows down from the upper chamber, it will flow through both sides of the C-shaped island. But When the fluid flows from the outlet to the inlet, the fluid will preferentially flow into the center of the C-shaped island and push the membrane up and block the inlet. The design parameters here are: Valve diameter (ϕ_v), Lower chamber height (H_{low}), Channel width (W_c), and Island width (W_i).

The above design parameters can be classified into pressure control variable and flow rate control variable, shown in Figure 5.2.



Pressure control variable

- ϕ_{in} : Inlet diameter
- ϕ_v : Valve diameter
- M : Membrane thickness
- H_{up} : Upper chamber height
- H_{low} : Lower chamber height

Flow rate control variable

- W_c : Channel width
- W_i : Island width
- ϕ_{in} : Intake diameter

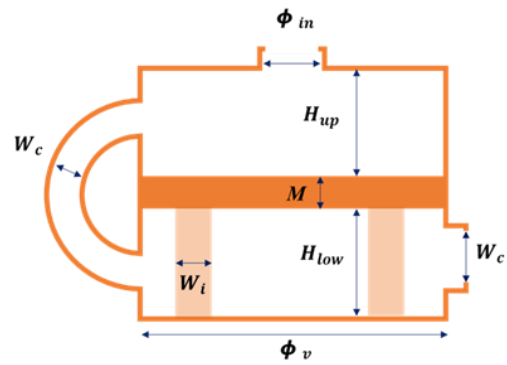


Figure 5.2: Passive valve design space.

5.2.2 Passive Microfluidic Valve Three States

The passive microfluidic valve in this study has three states which are neutral position, always open position, and close position, as shown in Figure 5.3.

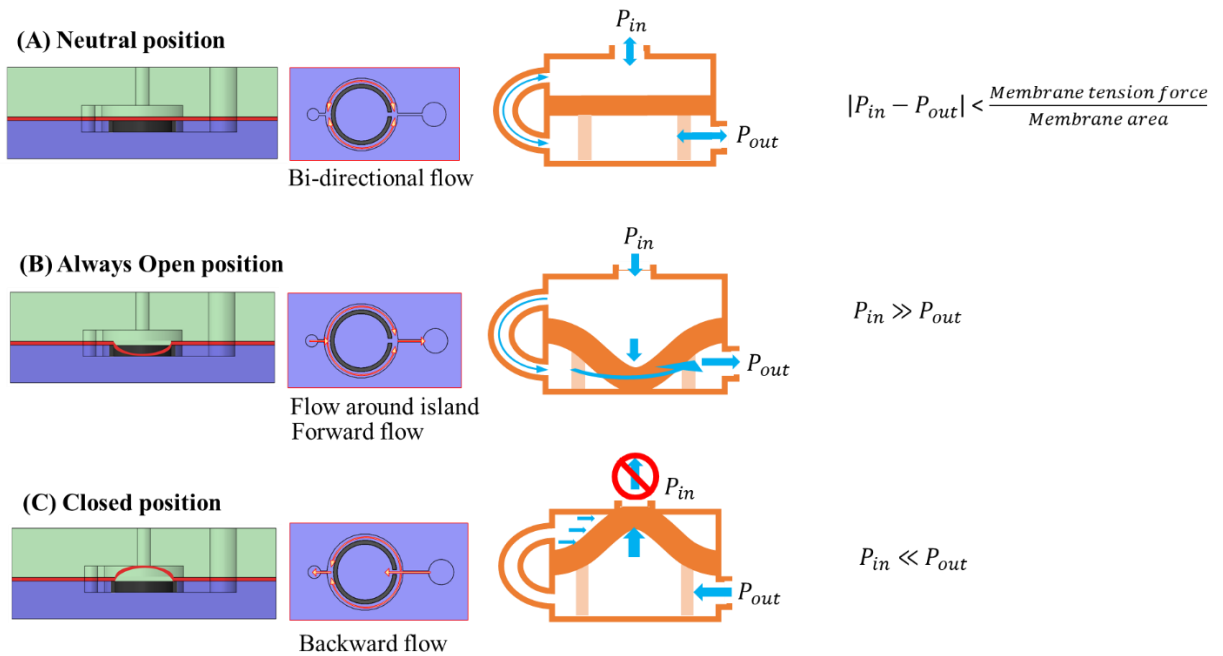


Figure 5.3: Passive microfluidic valve three states.

The first state is the neutral position, as shown in Figure 5.3. When the pressure difference between the upper chamber and the lower chamber of the microfluidic valve is less than the tension of the membrane itself, the membrane will not have any contact with the upper layer or the lower layer. At this moment, the microfluidic valve is bi-directional, and the direction of fluid flow will depend on the pressure of the inlet or outlet; whichever side has higher pressure flows from the side with higher pressure to the side with lower pressure.

The second state is the always open position. When the pressure in the upper chamber of the microfluidic valve is greater than in the lower chamber and the pressure difference between the two is greater than the tension of the membrane itself, the membrane will be pushed to the lower layer. Because of the C-shaped island structure, the fluid can flow along both sides of the island and flow out to the outlet.

The third state is the close position. When the pressure of the lower chamber of the microfluidic valve is greater than the upper chamber, and the pressure difference between the two is greater than the tension of the membrane itself, the fluid flowing from the outlet will first flow into the center of the C-shaped island structure. The membrane will be pushed to the upper layer and block the inlet in the middle. The flow from the outlet to the inlet is blocked.

One thing to mention here is when the always open position and the close position are switched to each other, they must first return to the neutral position, as shown in Figure 5.4.

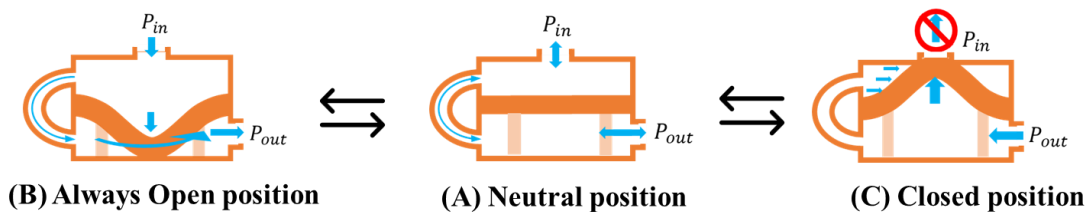


Figure 5.4: Passive microfluidic valve state transition diagram.

5.2.3 Combustion Chamber Pressure Hypothesis

Here we show the hypothesis we make from the four-stroke cylinder pressure. We start to look at the four-stroke engine because it's the most common combustion chamber that we use nowadays. Here we have the cylinder pressure waveforms that match each stroke, as shown in Figure 5.5.

During the compression stroke, the cylinder pressure increases. When ignition occurs, the cylinder pressure reaches its highest point. After the piston is pushed down, the volume increases, the air cools, and the pressure drops. After entering the next stroke, the exhaust valve is opened. The air has been pushed out of the cylinder, and the cylinder pressure will remain at 1 atmosphere until the exhaust valve is closed. During the intake stroke, the intake valve is opened, and there is a negative pressure in the cylinder, and air will flow into the cylinder.

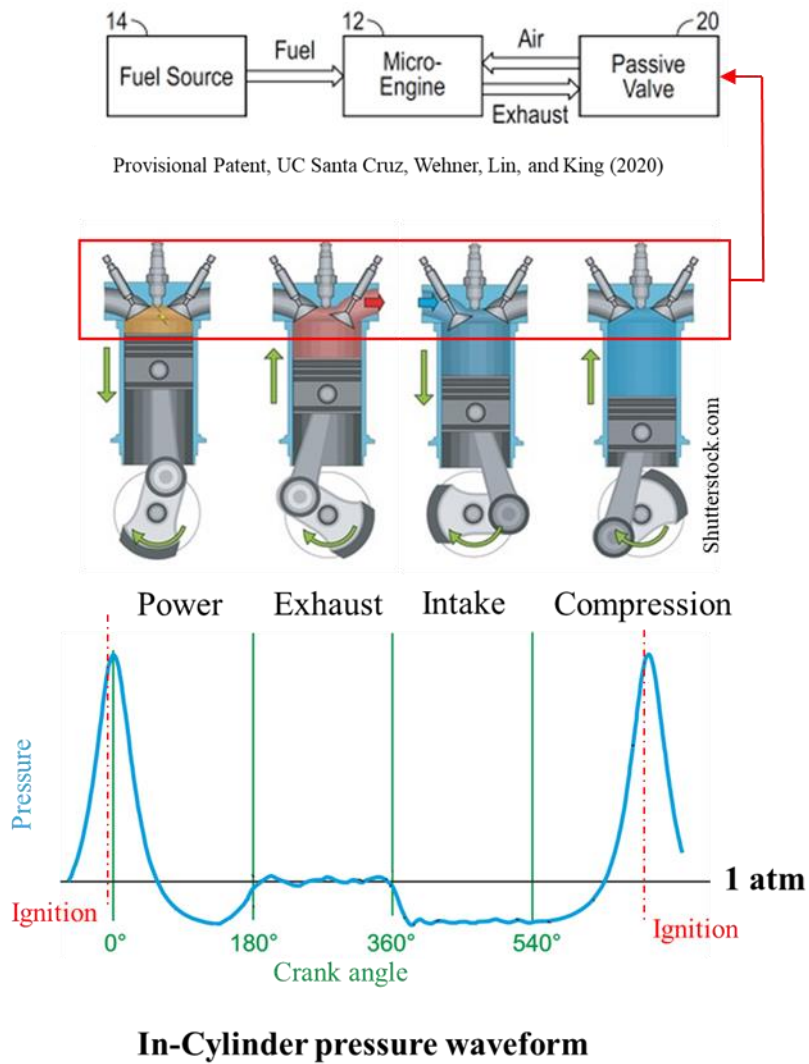


Figure 5.5: The four-stroke cylinder pressure waveforms [169], [170]

Here we show our assumptions derived from four-stroke cylinder pressures. The combustion chamber is made of fleible material, so we assume that the cylinder pressure is conceptually similar to the four-stroke engine. The difference is that there is no compression stroke in the micro combustion chamber. Therefore, here we show the state of the valves at different strokes, as shown in Figure 5.6. When the ignition is

started, the pressure will reach the highest point, the valve will close, the combustion chamber will expand, the volume will increase, the air will cool, and the pressure will drop. When the pressure drops to a certain pressure, the valve will reopen to vent the air. While combustion is a highly exothermic reaction which causes drastic expansion of gas, the number of mols remains constant. Thus the exhaust of gas during combustion leaves fewer mols of gas in the chamber. We anticipate that this will create a negative pressure in the combustion chamber upon cooling. The valve will then allow fresh air to flow into the combustion chamber.

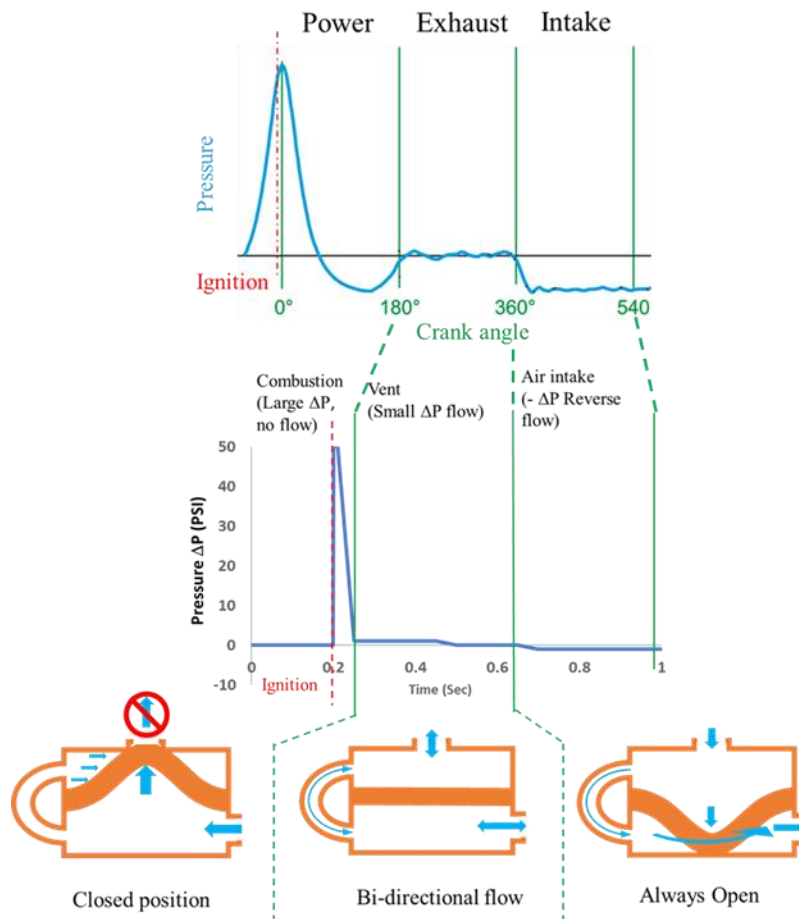


Figure 5.6: The state of the valves at different strokes

5.2.4 Fabrication

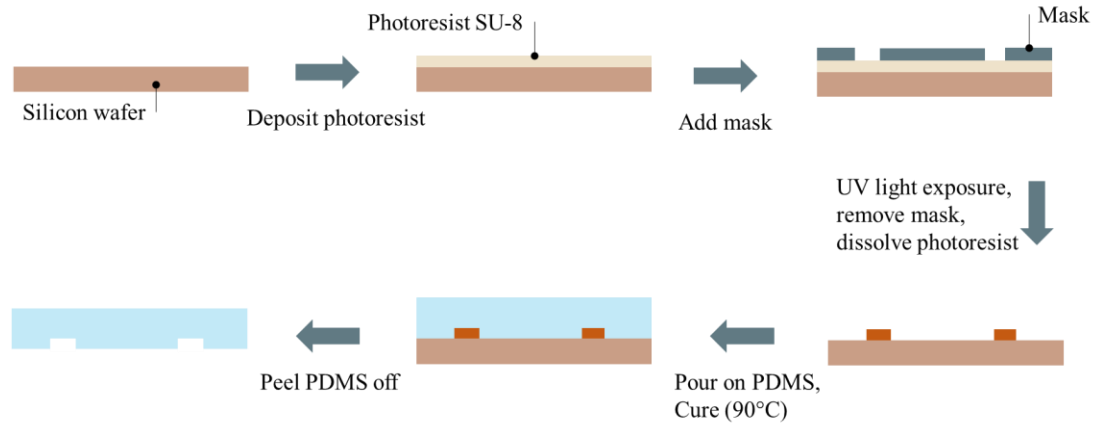


Figure 5.7: Soft lithography fabrication process.

We use soft lithography technology [171] to make the passive microfluidic valve, where the molding master was made from the negative SU-8 photoresist (SU-8 3050, Microchem Corp). To begin with, the main fabrication steps for the upper and lower layers are shown in Figure 5.7. Specifically, the SU-8 3050 negative photoresist is first spin-coated on the silicon wafer at 1000 rpm for 1 minute to obtain a uniform thickness of $100\ \mu\text{m}$. Then, the device goes through the steps of soft bake, exposure, post-exposure bake (PEB), and development [172] to get the SU-8 master mold.

Then a 1:10 weight ratio of curing agent and PDMS prepolymer (Sylgard 184 Silicone Elastomer Kit, Dow Corning) was then mixed and degassed for 10 minutes to remove any remaining air bubbles. To facilitate later release from the SU-8 mold, the mold was vaporized with trimethylchlorosilane (TMCS, Puriss, P99% GC, Sigma Aldrich inc). After that, the PDMS mixture was put into the SU-8 mold and cured for 50 minutes at $90\ ^\circ\text{C}$. The resulting PDMS layer with appropriate microfluidic

characteristics was obtained after peeling it from the mold. Next, holes were punched for the inlet and outlet of the cured PDMS part using a 0.5 mm diameter biopsy punch.

Meanwhile, the curing agent and PDMS prepolymer were mixed at a ratio of 1:10 and spin-coated on a flat wafer at 2500 rpm, and cured at 60 °C for 3 hours, resulting in a PDMS thin membrane with a thickness of about 50 μm . The wafer for spin-coated is also treated with TMCS on its surface.

To bond all the structure layers together, all the PDMS layers and PDMS membrane were treated with low-power oxygen plasma [173], as displayed in Figure 5.8A. The three structural layers were finally bonded together in the bottom-up sequence. A packaged three passive microfluidic valves prototype device is shown in Figure 5.8B.

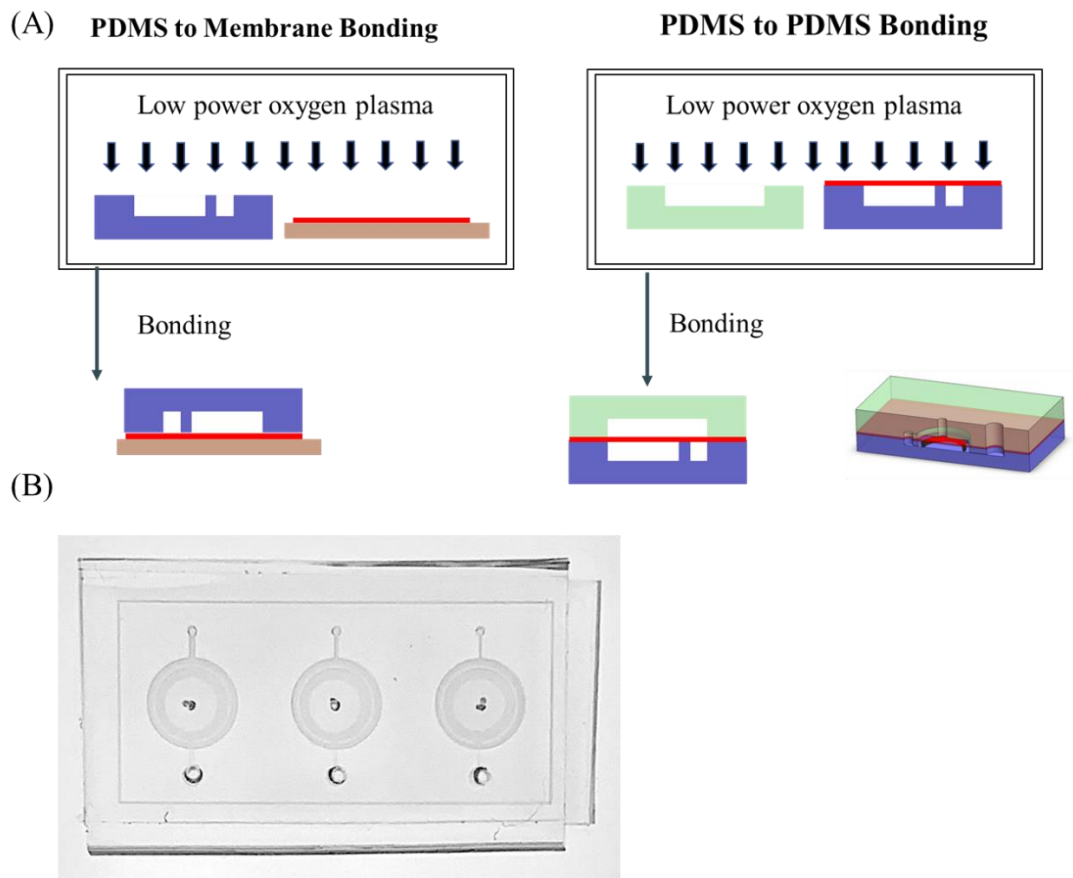


Figure 5.8: (A) Bonding process of PDMS to PDMS using low-power oxygen plasma.
 (B) A packaged three passive microfluidic valves prototype device

5.2.5 Experiment Setup

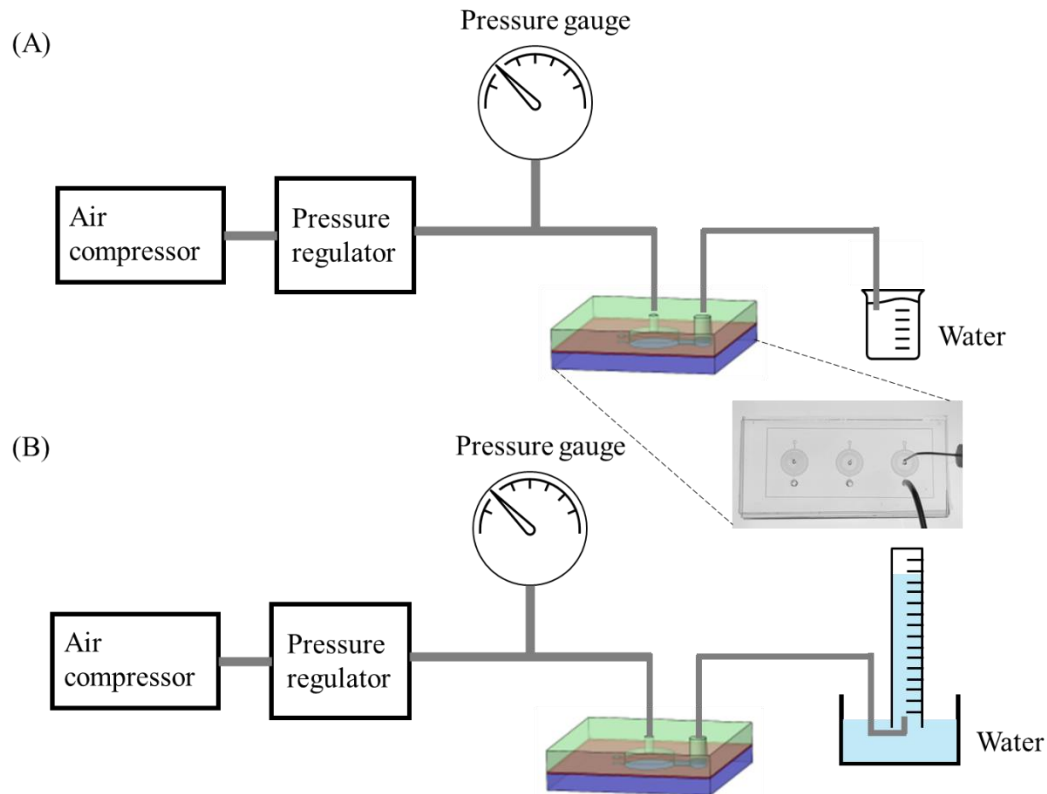


Figure 5.9: Experiment setup (A) is used to test the pressure. (B) is used to test the flow.

We use the setup as shown in Figure 5.9 to test the microfluidic valve where we use air as the test fluid. Figure 5.9A is used to test the pressure, the gas passes through the pressure regulator and connects to the test microfluidic valve, and then connects to the air tube with the needle in the end to the water cup. By observing the bubbles in the water to measure the required pressure. Just a needle in water showed a 0.16 psi pressure before flowing bubbles. Figure 5.9B is used to test the flow. We connect the air tube to the water cup and use a graduated measuring cup to collect the air bubbles and observe the change in the air bubble volume to measure the flow rate of the

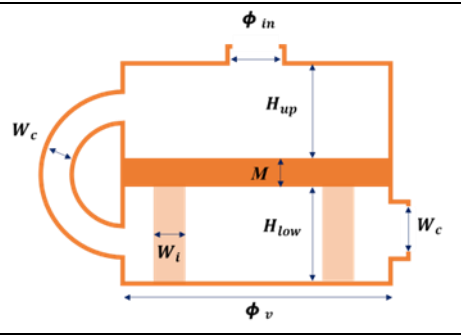
microfluidic valve. During measurement, the inlet and outlet of the microflow valve may be connected to the gas pipe in opposite directions, depending on the required flow direction of the gas.

5.3 Results and Discussion

5.3.1 Pressure Test for State Switched

Table 5.2 Valve parameter for 5.3.1 section and baseline reference

Valve parameter		Value
Inlet diameter	ϕ_{in}	0.5 mm
Valve diameter	ϕ_v	5 mm
Membrane thickness	M	55 μm
Upper chamber height	H_{up}	100 μm
Lower chamber height	H_{low}	100 μm
Channel width	W_c	100 μm
Island width	W_i	100 μm



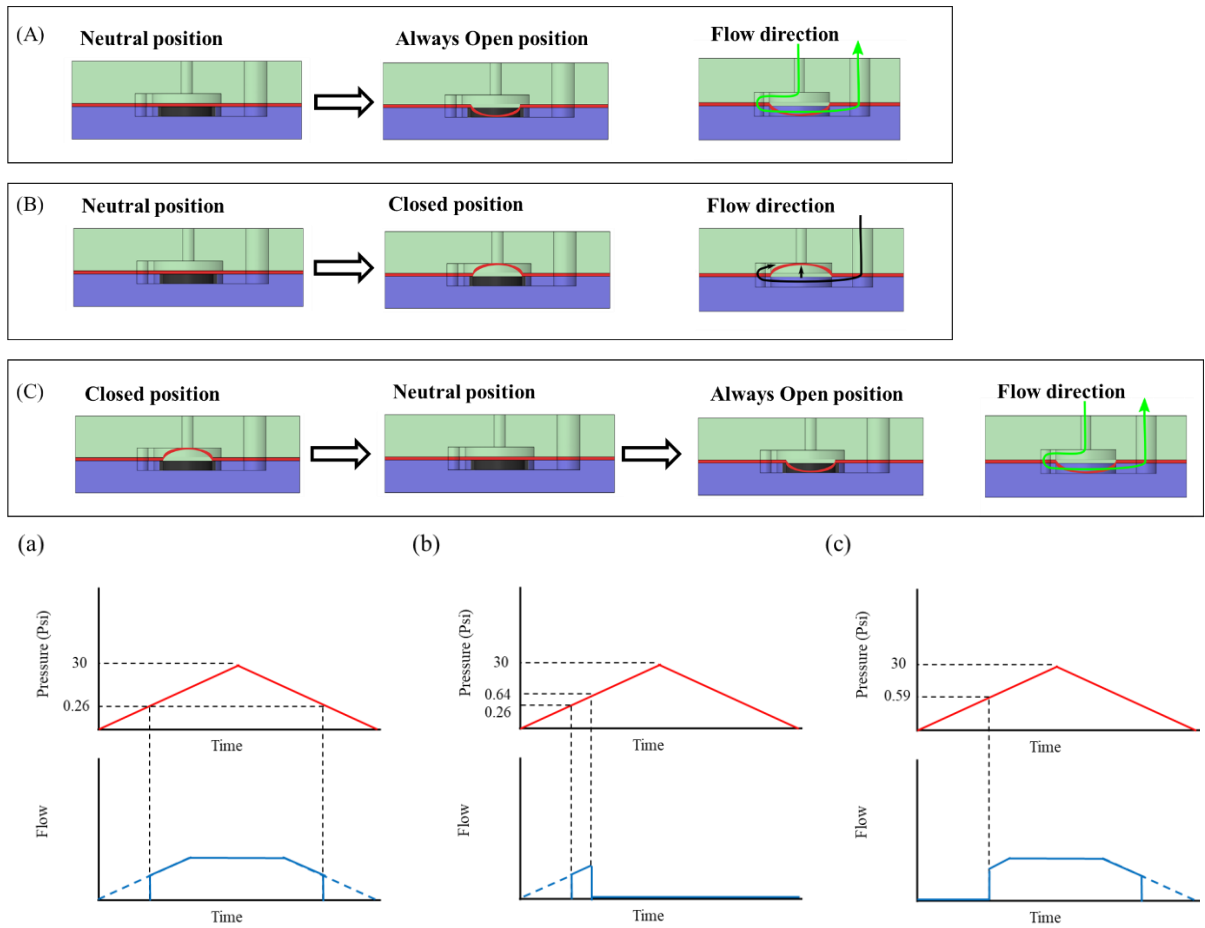


Figure 5.10: Three states transitions and test results.

The parameters of the microfluidic valve used in this experiment can be seen in Table 5.2. In this experiment, we measured the pressure required for the three states transition, as shown in Figure 5.10. We adjusted the pressure from 0 psi to 30 psi to test the microfluidic valve, and the (a), (b), and (c) in the figure are the results of the three states changes of the microfluidic valve, and the (A), (B), and (C) corresponds to the same letter state. The solid line is the actual measured data. We have extrapolated data beyond our measurement limits (dotted line) on the assumption that this always-

open valve will perform similarly at very low differential pressures ($\Delta_p < 1.8 \text{ kPa}$) as it does at higher pressures ($1.8 \text{ kPa} < \Delta_p < 200 \text{ kPa}$).

(a) As the gas flows from the inlet to the outlet, we can see that the microfluidic valve keeps the gas flowing through, the flow increases and then levels off. We see the first bubble appear at a pressure of 0.26 psi.

(b) As the gas flows from the outlet to the inlet, we see that the first bubble appears at a pressure of 0.26 psi. But once the pressure continues to increase to 0.64 psi the bubbles stop appearing, which means that the membrane is blocking the inlet. We continued to increase the pressure to 30 psi without finding any bubbles, which means that the microfluidic valve can withstand at least 30 psi of reverse pressure. We also call this blocking pressure.

(c) When we adjusted the direction of airflow in experiment (B) to flow from the inlet to the outlet again, we saw the first air bubble appear at 0.59 psi. This means that the pressure required to change the close position state to the neutral position state is 0.59 psi, which we can also call the reopen pressure.

From this experiment, we know that the blocking pressure is 0.64 psi, and the reopening pressure is 0.59 psi. We use this data as a reference point for the next experiment.

5.3.2 Pressure Test for Changing the Chamber Heights

Table 5.3 Valve parameter for 5.3.2 section

Valve parameter		Value
Inlet diameter	ϕ_{in}	0.5 mm
Valve diameter	ϕ_v	5 mm
Membrane thickness	M	55 μm
Upper chamber height	H_{up}	50 & 100 μm
Lower chamber height	H_{low}	100 & 50 μm
Channel width	W_c	100 μm
Island width	W_i	100 μm

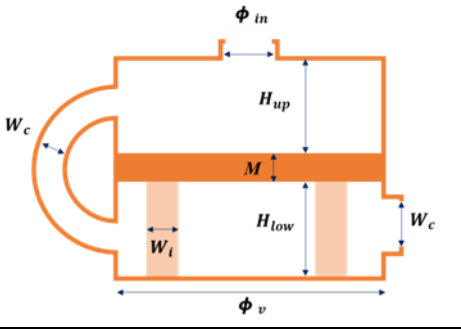
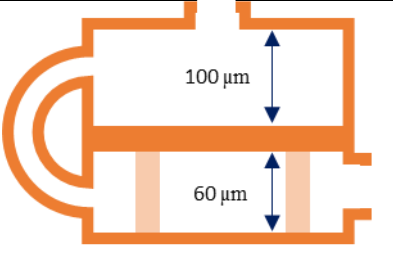
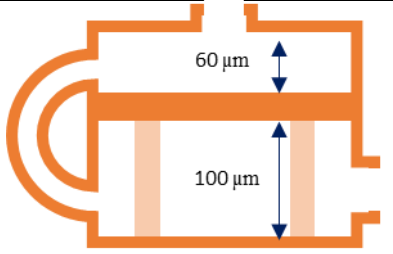


Table 5.4 Pressure test for changing the chamber heights results

Valve parameter		
Blocking pressure	~0.45 - 0.65 psi	~0.20 - 0.40 psi
Reopen pressure	~0.20 - 0.40 psi	~0.45 - 0.65 psi

In this experiment, we built a number of devices, varying the chamber height of the microfluidic valve and kept the rest of the parameters the same as before, as shown in Table 5.3. We adjusted the upper chamber height of one valve to 100 μm and the lower chamber height to 60 μm . The other valve is to reverse the two heights for comparison, as shown in Table 5.4. We found that the thinner the upper chamber height, the lower the blocking pressure. But the reopening pressure will be bigger. So we can say that the blocking pressure is negatively correlated with the reopening pressure.

5.3.3 Flow Rate Test

Table 5.5 Valve parameter for 5.3.3 section

Valve parameter		Value
Inlet diameter	ϕ_{in}	0.5 mm
Valve diameter	ϕ_v	3 – 5 mm
Membrane thickness	M	55 μm
Upper chamber height	H_{up}	100 μm
Lower chamber height	H_{low}	100 μm
Channel width	W_c	100 - 300 μm
Island width	W_i	100 μm

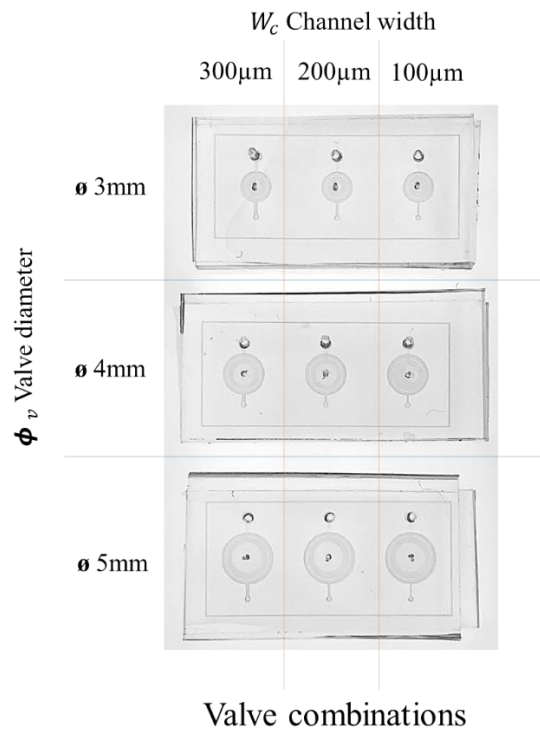
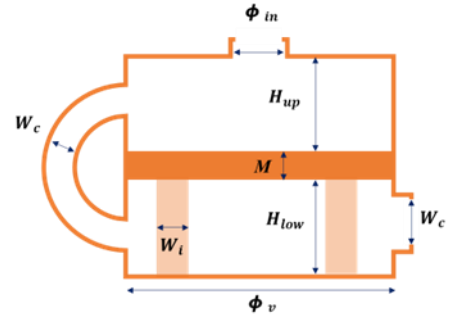


Figure 5.11: Test valves, 9 valves in total.

In this experiment, we built a number of devices, varying the channel width and valve diameter of the microfluidic valve and kept the rest of the parameters the same

as before, as shown in Table 5.5. All the test valves are shown in Figure 5.11. There are 9 valves in total. The experimental results are shown in Figure 5.12.

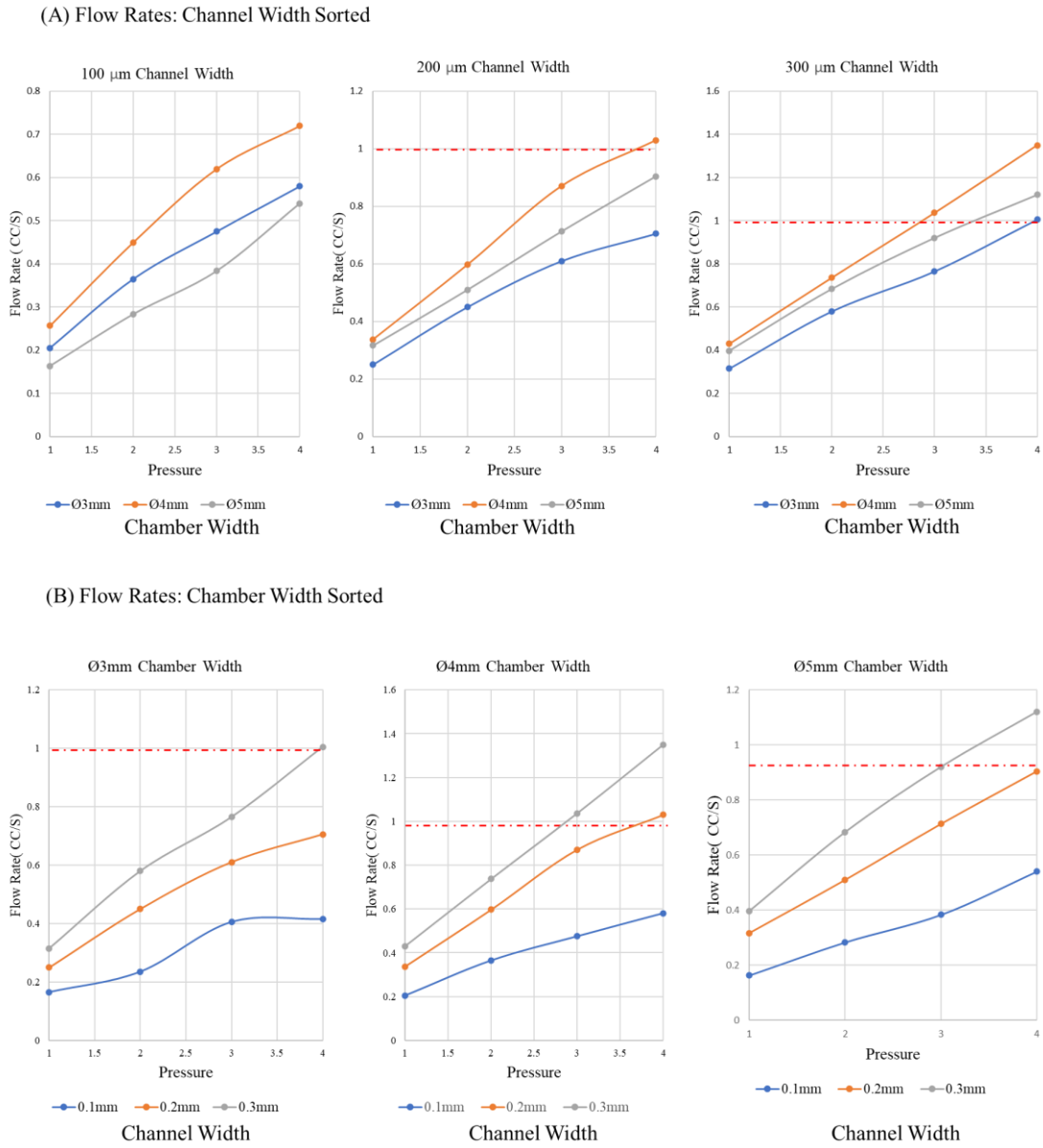


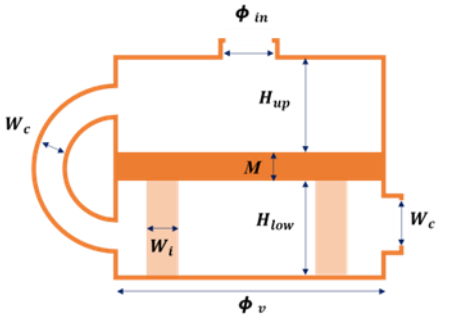
Figure 5.12: Flow rate test results

We have found from this experiment that the highest flow rate can be achieved with a 300 μ m channel and 0.4mm chamber width. And the channel width has a more significant effect on the flow rate than the chamber width.

5.3.4 Flow Rate Improving Test

Table 5.6 Valve parameter for 5.3.4 section

Valve parameter		Value
Inlet diameter	ϕ_{in}	0.5 mm
Valve diameter	ϕ_v	5 mm
Membrane thickness	M	55 μ m
Upper chamber height	H_{up}	100 μ m
Lower chamber height	H_{low}	100 μ m
Channel width	W_c	0.6 - 1.2 mm
Island width	W_i	100 μ m



In this experiment, we adjusted the channel width of the microfluidic valve to further increase the flow rate. We hope that the lower pressure can be used to achieve a flow rate of 1 cc/s. The rest of the parameters remain the same as before, as shown in Table 5.6. The experimental results show that In Figure 5.13. The valve achieves a lower impedance than the previous valve using wider channel widths. We also measured the blocking pressure of these three valves at 1.2~1.5 psi.

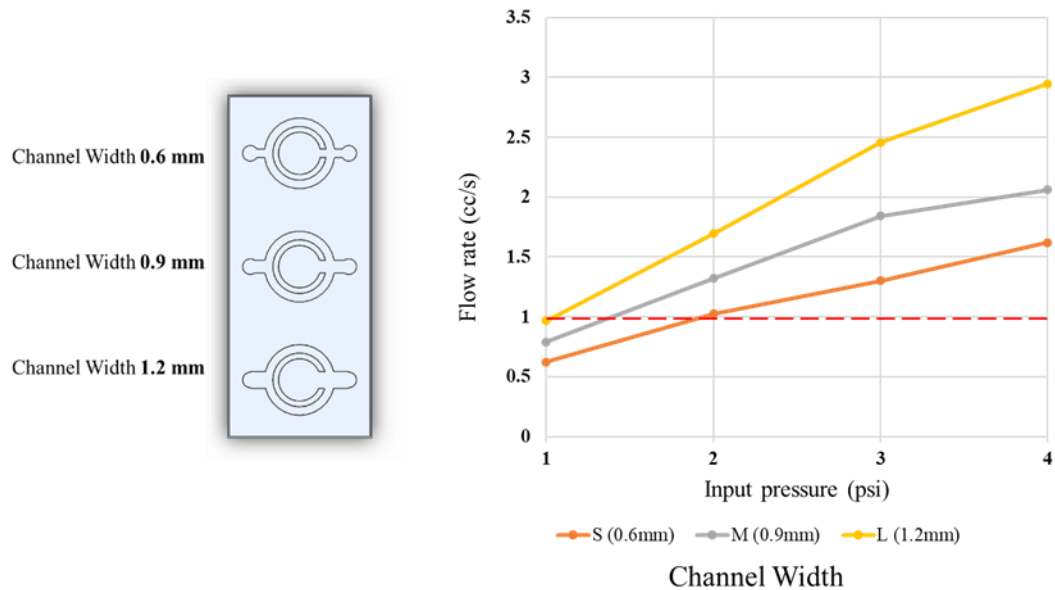


Figure 5.13: Flow rate improving test results. The red dotted line indicates the desired minimum flow rate (goal) of 1 cc/second.

5.4 Conclusion

In this study, we design and produce a lightweight and durable passive microfluidic valve for use in the micro combustion chamber. This passive microfluidic valve can be installed on a micro-combustion chamber and is responsible for all fluid control, including intake and exhaust. And we provide corresponding design space to passively control the flow and valve pressure. Our microfluidic valve achieves a flow rate of 1cc/s at 1 psi input pressure in forwarding flow. It can also be blocked at 1.5 psi in reverse flow and can withstand 30 psi of reverse pressure. Although we did not actually connect to the micro-combustor for the experiment, the experimental data above alone can achieve our hypothetical situation. In the future, we can do more experiments with more design parameters to let us have a clear understanding. This

novel passive microfluidic valve may also be used in other applications in the future, such as sensors for soft robotics.

Chapter 6

Concluding Remarks and Future Work

While the previous chapters contained conclusions each with a specific area of research, this chapter provides some overall remarks on the dissertation as well as directions for future work. As stated in the introduction, we rethought soft systems, and the goal of this thesis was to propose fundamental novel types of sensors and actuators to develop the necessary technologies for the soft robots field to move from intriguing concepts to useful devices. To achieve this goal, we sought to identify and rigorously investigate new frameworks that employ multiple existing actuation methods for the bioinspired soft finger to perform like a human, as well as to develop a novel soft sensing system to improve accuracy while reducing computation and data acquisition needs.

We first rethought sensing, in which traditional rigid robot sensing is very intuitive, using as many sensors as their degrees of freedom (DOF), to describe the state of the robot. But for soft robots sensing becomes much more difficult. We first have to overcome the problem of how the sensor itself is installed on the robot, and then how many sensors are required to provide enough information to the controller to complete the control computation. We know that the more complete we can know the state of the

robot, the more accurately we can control it. Therefore, for a soft robot with infinite DOF, it must have enough sensors to ensure good control. In a conventional robot, fewer than 10 sensors may be needed to determine pose and interaction, but in a soft robot, more than 100 sensors may easily be desirable. For current soft sensors, it is difficult to increase the number of sensors without adding additional components.

In chapter 3 we addressed the problem of how to reduce the burden of the rapid growth of multiple soft sensors used. Our novel soft sensors are primarily intended to be used in groups. A properly configured array of these deformation and pressure sensors, intended to be designed into a soft robot at the system level, can provide state awareness far beyond that of individual sensors. The resistance or capacitance of most soft robot sensors (and many sensors in general) varies in response to a change in a physical parameter such as length, bend angle, or contact pressure. Before the resulting signal is sent to a computer, each sensor requires wiring, electronic circuitry, and a dedicated input to a data acquisition system. Five sensors necessitate a fivefold increase in infrastructure. We present 11 sensors in the display assembly; this number was chosen as it was the number required to characterize the soft finger (nine deformation and two pressure sensors). With our method, any upgrading (to increase sampling frequency or resolution) would be contained to the camera system, while upgrading dozens of electrical sensors would also be a sizeable task. With our method, many fibers could be routed back to one remote display assembly, where a single digital camera could track the motion of all markers in a controlled environment, optimally lit

for contrast and marker tracking. As a result, dozens of markers and fluid channels can almost as easily be monitored as one.

Secondly, we rethink actuation; soft actuators are great for applying a distributed force on fragile objects. But the backdrivability that gives them the advantage also limits their use. When the spray bottle is pressed against the soft gripper, it will back drive out of the way and fail to successfully actuate the spray bottle trigger.

In chapter 4 we addressed the need to develop a structure that enables soft robotic fingers to exhibit softness and rigidity at the corresponding application timing. We propose a new soft-rigid hybrid structure design as well as a method for pneumatic and tendon-driven two actuators to interact. The newly developed segmented controllable soft-rigid module combines the benefits of a soft robotic finger with the ability to provide force in a specific direction. We conducted a modeling analysis of this controlled soft-rigid module, which provides a flexible and scalable design framework for bioinspired robotic fingers. In our case, friction worked to our advantage, providing locking force greater than the theoretical (frictionless) case. Thus, actual locking force was 2-3x higher than the frictionless model predicted. We compare the mechanical model of a single locking module to the overall kinematic analysis, as well as the combination of each locking module used with the actuator. This includes pure soft mode, soft-rigid hybrid mode, and rigid mode to validate our model using experimental data. In the grasping performance test, we demonstrated that this soft-rigid hybrid structure of the soft finger could provide a maximum gripping force of 125N with a single finger when all locking modules were locked. In the experiment,

we used paper cups and sponges to demonstrate how the finger can quickly adapt to the shape of the gripping object, adjust the gripping arc, and deliver force in a specific direction. We believe that the method of soft-rigid hybrid structural design interacting with multiple actuators provides a scalable and adaptable design framework for future bioinspired fingers, based on the kinematic analysis and experimental results. We focused on a bioinspired soft finger with in-plane motion in this study and established different grasping modes.

Lastly, we have also studied the possible power source of soft robots and found that if we look at the energy density alone, chemical reactions can provide a higher energy source than those energy sources with rigid components. However, the challenge of chemical reactions is to control the fluid efficiently. Therefore, in chapter 5 we have studied the use of microfluidic valves for micro combustion chambers.

In chapter 5 we design and fabricate a lightweight and long-lasting passive microfluidic valve for use in a micro combustion chamber. This passive microfluidic valve, which can be installed on a micro-combustion chamber, is in charge of all fluid control, including intake and exhaust. We also provide a design space for passively controlling the flow and valve pressure. In forwarding flow, our microfluidic valve achieves a flow rate of 1cc/s at 1 psi input. It can also be blocked at 1.5 psi in reverse flow and can withstand reverse pressure of 30 psi. Although we did not connect to the micro-combustor for the experiment, the experimental data presented above is sufficient to achieve our hypothetical engine design. In the next step, we can conduct additional experiments with additional design parameters to gain a better understanding.

We believe this novel passive microfluidic valve could be used in other applications, such as sensors for soft robotics.

The ultimate goal would be to have a fully functioning bioinspired soft finger to perform like a human and it is capable of assisting humans within a more efficient way without any safety concerns. In the previous chapters, we developed the individual technologies (sensing and actuation) required to ultimately build the integrated sensorized stiff-soft finger we envision as an end goal as shown in Figure 6.1. There are many possible directions for future work that build upon our results, and we now highlight some of them.

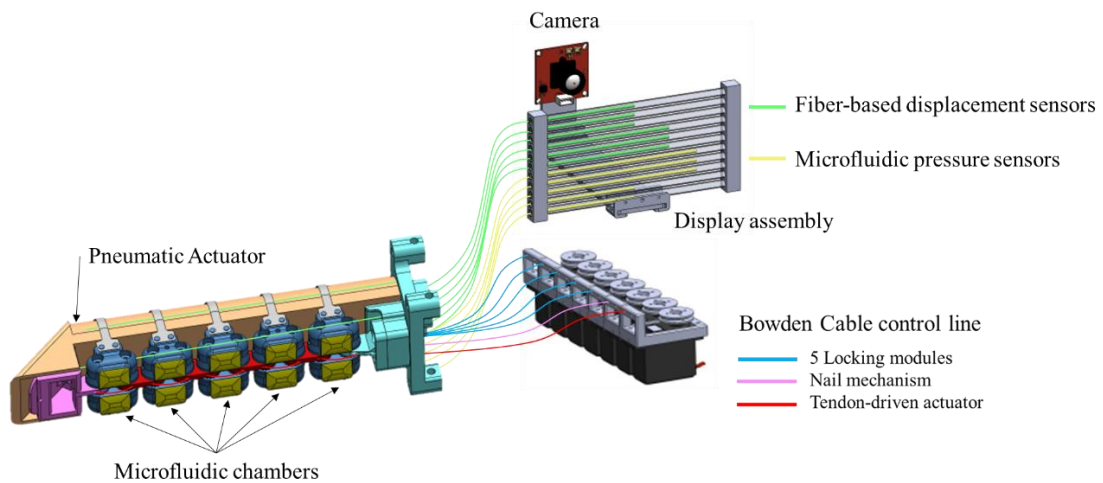


Figure 6.1: Concept of the integrated sensorized stiff-soft finger overview system.

For our newly developed soft sensing system, more sensors can be added in the future to test the performance of the system, as well as to experiment with mixed-mode deformations (combinations of bending and twisting). We will also integrate machine learning algorithms to enhance the accuracy in mixed-mode. The system can be

extended and integrated into more applications such as virtual and augmented reality, human-computer interaction systems, and wearable devices.

For the bioinspired soft finger, we hope to continue to reduce the size and control components to optimize the performance of the finger in the future. We also hope to extend the same concept and design to 3D motion and control manipulators and to add embedded sensors and appropriate controls for more applications.

Lastly, we believe the techniques demonstrated in this dissertation have pushed soft robotics technology forward. Bringing us closer to our vision, we believe soft robotics will act as a bridge between humans and traditional robots. When soft robot technology walks into our home, it helps us do our work in a more efficient way without any safety concerns.

Appendix A

Chapter 3 Euler-Bernoulli Beam Theory and Mechanics of Materials, Brief Overview

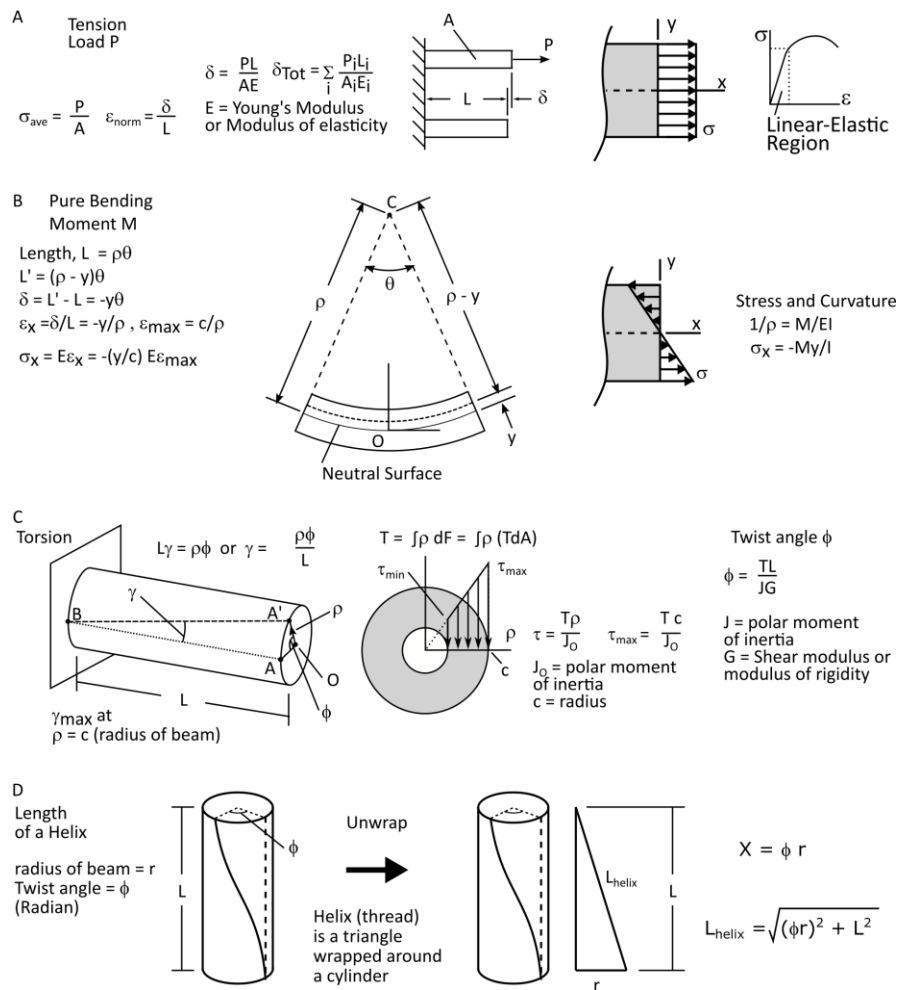


Figure A1: Mechanics of materials. (A). Beam in tension. (B). Beam in bending. (C). Beam in torsion. (D). length of a helix.

Considering first, a beam in tension (Figure A1.A), on a beam of length L with uniform cross section, the beam will lengthen proportionately with the load applied. The equation governing this extension is:

$$\delta = \frac{PL}{AE} \quad (\text{A1})$$

Where δ is total displacement, P is applied load, L is total beam length, A is cross section area, and E is Young's Modulus. Notice, in this loading scenario, the extension depends only on cross section AREA, not the shape of the member. Note, also, Young's modulus is a mechanical property of the material. When we look at the stress-strain curve for many materials, they exhibit a region of linearity (strain is proportional to applied stress, so relationship is a straight line through the origin) and a nonlinear region. A sample stress strain curve representative of many engineering materials (qualitative, no numbers included) is shown in Figure A1.A. The formulae presented here hold in the linear portion of the stress strain curve, governed by the young's modulus. Outside this region, direct quantitative relationships can no longer be applied with certainty, thus we use these as general rules to demonstrate the phenomena, not develop quantitative relationships.

When exposed to a bending moment, a beam forms a circular arc as shown in Figure A1.B. As shown, the center of this circular arc lies above the arc. The portions of the arc closest to the center of curvature experience compression. The portion farthest from the center of curvature experience tension. Somewhere between the region of maximum compression and the region of maximum tension lies a region of neither tension nor compression. We call this the neutral surface. Stress along the cross section of a beam in bending follows the relationship

Within the linear elastic range, stress from bending (Fig. A2.B) follows the equation

$$\sigma_x = -\frac{My}{I} \quad (\text{A2})$$

Where σ_x is tensile or compressive stress, M is applied bending moment, y is distance from neutral surface (positive toward the center of curvature), and I is second moment of inertia. The negative sign indicates compression toward the center of bending. Strain follows the equation

$$\epsilon_x = -\frac{y}{\rho} \quad (\text{A3})$$

Where ϵ_x is strain in the beam axis, y is distance from the neutral surface (positive toward the center of curvature), and ρ is radius of curvature of the bent beam. The negative indicates shortening toward the center of curvature.

Shearing stress due to torsion (Fig. A1.C) follows the equation

$$\tau = \frac{T\rho}{J} \quad (\text{A4})$$

Where τ is shear stress, T is applied torque, ρ is distance from the axis of rotation, and J is polar moment of inertia. Angle of twist follows the equation

$$\phi = \frac{TL}{JG} \quad (\text{A5})$$

where ϕ is total twist of the beam, L is beam length, J is polar moment of inertia, and G is shear modulus. We can find the change in length of a line (linear initially, helical after twist) parallel to the axis of the beam, a distance r from the twist axis. First, consider the shape of a helix (similar to a screw thread). A helix can be thought of as a right triangle or ramp wrapped around a cylinder. The height of this triangle is the length of the cylinder. The width of the triangle is the length of the portion wrapped about the cylinder. Angle of Twist is ϕ as we calculated in (A5). Therefore, width of the triangle X is $(\phi/2\pi) \times (2\pi r) = r\phi$. Thus, the length of the helix is the length of the hypotenuse of a right triangle of sides L and $r\phi$. Initially of length L , after twisting an angle ϕ , the helix (former line, now helix) has a length found from the formula

$$L_{helix} = \sqrt{L^2 + (r\phi)^2} \quad (\text{A6})$$

Where L_{helix} is the length of the helix, ϕ is angle of twist found above, L is beam length, and r is distance from twist axis. Thus, we find change in length of a fiber parallel to the longitudinal axis as

$$\Delta L = L_{helix} - L \quad (\text{A7})$$

Where ΔL is the change in length. With L and ϕ constant for any given beam and loading condition, we see that L_{helix} increases as r increases. Thus, the farther an element is from the axis of rotation, the more it will increase in length when experiencing twist. Thus fibers in the corners of a square cross section will experience more displacement than fibers at the center of the square faces, and a fiber at the center of the square face will not elongate at all.

Appendix B

Chapter 3 Vision Algorithms Detail

A Python script was created to automatically process the videos to extract position data. The first frame of the recorded video is accessed and then saved using the `deepcopy` function to preserve the original state. The frame then goes through a loop where the user moves lines, displayed with the OpenCV line function, vertically and horizontally to create the boundary for each cable's channel, as well as flip the frame along the y axis if the orientation is not correct. Once the user has completed preprocessing the frame, the selected boundaries and orientation are recorded. The saved copy of the first frame is then accessed, and the object tracking algorithm begins. Each pixel of each frame is initially encoded as three individual bytes representing the intensity of red, green, and blue hues. A new frame with cropped dimensions around the selected boundaries is then constructed where the value of each pixel is a single byte value calculated with the following formula:

$$pixel_{gray} = \frac{1.6 (pixel_{red} + pixel_{green} + pixel_{blue})}{3} \quad (B1)$$

The new frame then goes through the Canny algorithm. The Canny algorithm takes the numerical derivative of pixels in the horizontal and vertical directions and creates a gradient two-dimensional array [174]. To reduce noise, each index is compared against its neighbors to check if it is a local maximum. The maximums are set to 1, and all other indices are suppressed to 0. The binary two-dimensional array then goes through the Probabilistic Hough Lines Transform algorithm. The Probabilistic Hough Lines Transform algorithm processes the binary array by converting the position of a sufficiently sized random subset of the indices (x_i, y_i) with the value 1 from Cartesian coordinates to Hough Space lines with the following equation [175]:

$$\rho = x_i \cos \theta + y_i \sin \theta \quad (B2)$$

The algorithm then iterates over θ in the range $[0, 180]$ degrees, and for every intersection between two or more lines (θ_0, ρ_0) , the total number of intersections is recorded. If the number of intersections is larger than a set threshold, then the Hough Space coordinates are converted to Cartesian coordinate line endpoints with the equations [175]:

$$x_{1,2} = (\cos(\theta_0) * \rho_0) \mp 1000 * \sin(\theta_0)$$

$$y_{1,2} = (\sin(\theta_0) * \rho_0) \pm 1000 * \cos(\theta_0) \tag{B3}$$

These equations yield lines that span the entire frame. The algorithm then isolates the subsection of these lines that correspond to continuous high values from the binary array. The script then loops through each user-defined boundary and extracts the subset of fully contained lines. The rightmost end point of each line is recorded in the comma separated value (csv) file and the next frame is then loaded.

Appendix C

Chapter 3 Fabrication Detail

The fabrication of an elastomeric finger assembly consists of three molding steps, several cable routing steps, fastening steps, and final integration/assembly as shown in Figure A2. First, a mold (Mold 1) is assembled; including three 0.8mm diameter, semi-rigid cylinder parts (Bars). These bars will contain the central fiber (Fiber 5) and liquid for the microfluidic pressure sensor. Mold 1 is filled with elastomer (Ecoflex 30) and cured at 60 °C for at least 40 min (Figure A2.A). The elastomeric construct is removed from Mold 1, the two bars for the microfluidic pressure sensor are removed, a short piece of silicone tubing is inserted, connecting the two microfluidic channels, and an end-cap (shown in green) is secured to the distal end of the elastomer (Figure A2.B). The construct is installed into another mold (Mold 2) and instrumented with eight more bars which will contain the other eight fibers (1–4, 6–9). Microfluidic channels are instrumented with temporary PTFE tubing to prevent elastomer ingress. Mold 2 is filled with Ecoflex 30 and cured at 60 °C for at least 40 min (Figure A2.C). The construct is removed from Mold 2, and temporary PTFE tubing is removed. At the proximal end of the device, the two microfluidic channels are instrumented with silicone tubing (shown in gray) which are routed through the base cap (shown in pink) and exit the system. The construct is assembled into a mold (Mold 3), filled with Ecoflex 30, and cured at 60 °C for at least 40 min (Figure A2.D). Mold 3 is removed, nylon fibers are routed through each of the nine fiber holes, and the fibers are fastened with screws to the distal end of the finger (Figure A2.E). Fibers and tubing for the microfluidic channel are routed through a base holder (shown in pink), and the base holder is mounted to the finger assembly. Tubing for the microfluidic channel is routed to the hole available just below Fiber 9 (shown in red). An additional hole is available above Fiber 1 for a surface-mount microfluidic pressure sensor if one is present (Figure A2.F). The display assembly is laid out with components of laser-cut acrylic. A small region of each fiber (~2 cm) is painted black near the entry of the display assembly. All fibers and the microfluidic pressure sensor are routed through the display assembly. Display assembly and base holder are fastened to fiber tubes with button head screws (Figure A2.G).

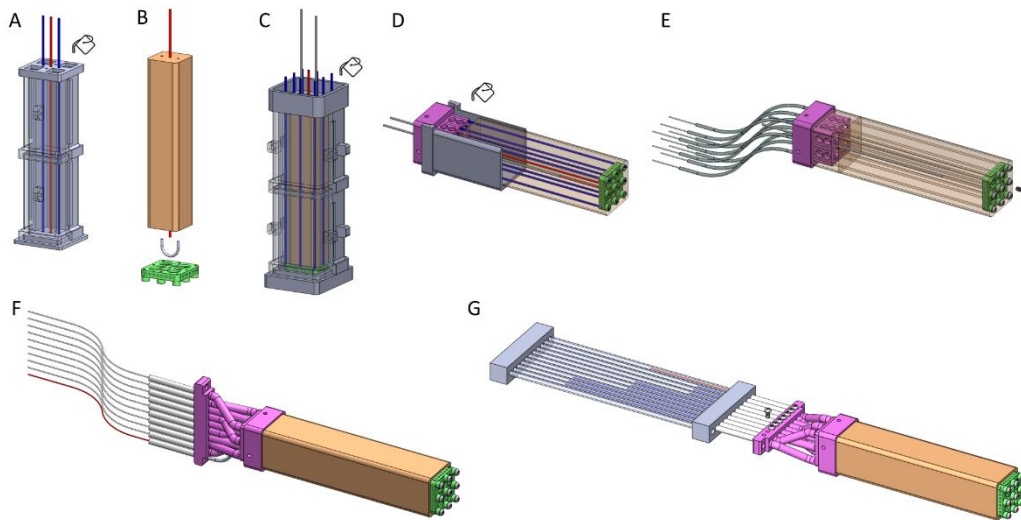


Figure A2: Elastomeric finger fabrication process. (A). Mold 1. (B). Connect vasculature to micro-fluidic pressure sensor. (C). Mold 2. (D). Mold 3. (E). Connect fibers. (F). Routing cables through base holder. (G). Integrate finger with Display Assembly.

Bibliography

- [1] G. M. Whitesides, “Soft Robotics,” *Angew. Chem. Int. Ed.*, vol. 57, no. 16, pp. 4258–4273, Apr. 2018, doi: 10.1002/anie.201800907.
- [2] D. Rus and M. T. Tolley, “Design, fabrication and control of soft robots,” *Nature*, vol. 521, no. 7553, pp. 467–475, May 2015, doi: 10.1038/nature14543.
- [3] C. Majidi, “Soft Robotics: A Perspective—Current Trends and Prospects for the Future,” *Soft Robotics*, vol. 1, no. 1, pp. 5–11, Mar. 2014, doi: 10.1089/soro.2013.0001.
- [4] S. Kim, C. Laschi, and B. Trimmer, “Soft robotics: a bioinspired evolution in robotics,” *Trends in Biotechnology*, vol. 31, no. 5, pp. 287–294, May 2013, doi: 10.1016/j.tibtech.2013.03.002.
- [5] D. Trivedi, C. D. Rahn, W. M. Kier, and I. D. Walker, “Soft robotics: Biological inspiration, state of the art, and future research,” *Applied Bionics and Biomechanics*, vol. 5, no. 3, pp. 99–117, Dec. 2008, doi: 10.1080/11762320802557865.
- [6] P. Polygerinos *et al.*, “Soft Robotics: Review of Fluid-Driven Intrinsically Soft Devices; Manufacturing, Sensing, Control, and Applications in Human-Robot Interaction: Review of Fluid-Driven Intrinsically Soft Robots,” *Adv. Eng. Mater.*, vol. 19, no. 12, p. 1700016, Dec. 2017, doi: 10.1002/adem.201700016.
- [7] N. G. Cheng, A. Gopinath, L. Wang, K. Iagnemma, and A. E. Hosoi, “Thermally Tunable, Self-Healing Composites for Soft Robotic Applications: Thermally Tunable, Self-Healing Composites ...,” *Macromol. Mater. Eng.*, vol. 299, no. 11, pp. 1279–1284, Nov. 2014, doi: 10.1002/mame.201400017.
- [8] G. Sumbre, G. Fiorito, T. Flash, and B. Hochner, “Octopuses Use a Human-like Strategy to Control Precise Point-to-Point Arm Movements,” *Current Biology*, vol. 16, no. 8, pp. 767–772, Apr. 2006, doi: 10.1016/j.cub.2006.02.069.
- [9] B. S. Homberg, R. K. Katzschmann, M. R. Dogar, and D. Rus, “Haptic identification of objects using a modular soft robotic gripper,” in *2015 IEEE/RSJ International Conference on Intelligent Robots and Systems (IROS)*, Hamburg, Germany, Sep. 2015, pp. 1698–1705. doi: 10.1109/IROS.2015.7353596.

- [10] P. Polygerinos *et al.*, “Modeling of Soft Fiber-Reinforced Bending Actuators,” *IEEE Trans. Robot.*, vol. 31, no. 3, pp. 778–789, Jun. 2015, doi: 10.1109/TRO.2015.2428504.
- [11] F. Ilievski, A. D. Mazzeo, R. F. Shepherd, X. Chen, and G. M. Whitesides, “Soft Robotics for Chemists,” *Angew. Chem. Int. Ed.*, vol. 50, no. 8, pp. 1890–1895, Feb. 2011, doi: 10.1002/anie.201006464.
- [12] R. F. Shepherd *et al.*, “Multigait soft robot,” *Proc. Natl. Acad. Sci. U.S.A.*, vol. 108, no. 51, pp. 20400–20403, Dec. 2011, doi: 10.1073/pnas.1116564108.
- [13] M. A. Skylar-Scott, J. Mueller, C. W. Visser, and J. A. Lewis, “Voxelated soft matter via multimaterial multinozzle 3D printing,” *Nature*, vol. 575, no. 7782, pp. 330–335, Nov. 2019, doi: 10.1038/s41586-019-1736-8.
- [14] B. Shih *et al.*, “Design Considerations for 3D Printed, Soft, Multimaterial Resistive Sensors for Soft Robotics,” *Front. Robot. AI*, vol. 6, p. 30, Apr. 2019, doi: 10.3389/frobt.2019.00030.
- [15] S. A. Morin, R. F. Shepherd, S. W. Kwok, A. A. Stokes, A. Nemiroski, and G. M. Whitesides, “Camouflage and Display for Soft Machines,” *Science*, vol. 337, no. 6096, pp. 828–832, Aug. 2012, doi: 10.1126/science.1222149.
- [16] T. Ranzani, S. Russo, N. W. Bartlett, M. Wehner, and R. J. Wood, “Increasing the Dimensionality of Soft Microstructures through Injection-Induced Self-Folding,” *Adv. Mater.*, vol. 30, no. 38, p. 1802739, Sep. 2018, doi: 10.1002/adma.201802739.
- [17] M. Wehner *et al.*, “An integrated design and fabrication strategy for entirely soft, autonomous robots,” *Nature*, vol. 536, no. 7617, pp. 451–455, Aug. 2016, doi: 10.1038/nature19100.
- [18] R. L. Truby *et al.*, “Soft Somatosensitive Actuators via Embedded 3D Printing,” *Adv. Mater.*, vol. 30, no. 15, p. 1706383, Apr. 2018, doi: 10.1002/adma.201706383.
- [19] K. C. Galloway *et al.*, “Soft Robotic Grippers for Biological Sampling on Deep Reefs,” *Soft Robotics*, vol. 3, no. 1, pp. 23–33, Mar. 2016, doi: 10.1089/soro.2015.0019.
- [20] A. M. Dollar and R. D. Howe, “The Highly Adaptive SDM Hand: Design and Performance Evaluation,” *The International Journal of Robotics Research*, vol. 29, no. 5, pp. 585–597, Apr. 2010, doi: 10.1177/0278364909360852.

- [21] R. R. Ma, L. U. Odhner, and A. M. Dollar, “A modular, open-source 3D printed underactuated hand,” in *2013 IEEE International Conference on Robotics and Automation*, Karlsruhe, Germany, May 2013, pp. 2737–2743. doi: 10.1109/ICRA.2013.6630954.
- [22] A. Kanada, F. Giardina, T. Howison, T. Mashimo, and F. Iida, “Reachability Improvement of a Climbing Robot Based on Large Deformations Induced by Tri-Tube Soft Actuators,” *Soft Robotics*, vol. 6, no. 4, pp. 483–494, Aug. 2019, doi: 10.1089/soro.2018.0115.
- [23] S. Kim, E. Hawkes, K. Choy, M. Joldaz, J. Foley, and R. Wood, “Micro artificial muscle fiber using NiTi spring for soft robotics,” in *2009 IEEE/RSJ International Conference on Intelligent Robots and Systems*, St. Louis, MO, USA, Oct. 2009, pp. 2228–2234. doi: 10.1109/IROS.2009.5354178.
- [24] Q. Ze *et al.*, “Magnetic Shape Memory Polymers with Integrated Multifunctional Shape Manipulation,” *Adv. Mater.*, vol. 32, no. 4, p. 1906657, Jan. 2020, doi: 10.1002/adma.201906657.
- [25] R. Pelrine, R. Kornbluh, Q. Pei, and J. Joseph, “High-Speed Electrically Actuated Elastomers with Strain Greater Than 100%,” *Science*, vol. 287, no. 5454, pp. 836–839, Feb. 2000, doi: 10.1126/science.287.5454.836.
- [26] R. D. Kornbluh *et al.*, “Dielectric elastomers: Stretching the capabilities of energy harvesting,” *MRS Bull.*, vol. 37, no. 3, pp. 246–253, Mar. 2012, doi: 10.1557/mrs.2012.41.
- [27] H. Lu, Y. Hong, Y. Yang, Z. Yang, and Y. Shen, “Battery-Less Soft Millirobot That Can Move, Sense, and Communicate Remotely by Coupling the Magnetic and Piezoelectric Effects,” *Adv. Sci.*, vol. 7, no. 13, p. 2000069, Jul. 2020, doi: 10.1002/advs.202000069.
- [28] T. George Thuruthel, Y. Ansari, E. Falotico, and C. Laschi, “Control Strategies for Soft Robotic Manipulators: A Survey,” *Soft Robotics*, vol. 5, no. 2, pp. 149–163, Apr. 2018, doi: 10.1089/soro.2017.0007.
- [29] K.-Y. Lin, A. Gamboa-Gonzalez, and M. Wehner, “Soft Robotic Sensing, Proprioception via Cable and Microfluidic Transmission,” *Electronics*, vol. 10, no. 24, p. 3166, Dec. 2021, doi: 10.3390/electronics10243166.
- [30] M. T. Tolley *et al.*, “A Resilient, Untethered Soft Robot,” *Soft Robotics*, vol. 1, no. 3, pp. 213–223, Sep. 2014, doi: 10.1089/soro.2014.0008.

- [31] E. C. Goldfield *et al.*, “Bio-Inspired Design of Soft Robotic Assistive Devices: The Interface of Physics, Biology, and Behavior,” *Ecological Psychology*, vol. 24, no. 4, pp. 300–327, Oct. 2012, doi: 10.1080/10407413.2012.726179.
- [32] M. Boivin, D. Milutinovic, and M. Wehner, “Movement Error Based Control for a Firm Touch of a Soft Somatosensitive Actuator,” in *2019 American Control Conference (ACC)*, Philadelphia, PA, USA, Jul. 2019, pp. 7–12. doi: 10.23919/ACC.2019.8815142.
- [33] D. Li, V. Dornadula, K. Lin, and M. Wehner, “Position Control for Soft Actuators, Next Steps toward Inherently Safe Interaction,” *Electronics*, vol. 10, no. 9, p. 1116, May 2021, doi: 10.3390/electronics10091116.
- [34] Z. Jiao, C. Zhang, W. Wang, M. Pan, H. Yang, and J. Zou, “Advanced Artificial Muscle for Flexible Material-Based Reconfigurable Soft Robots,” *Adv. Sci.*, vol. 6, no. 21, p. 1901371, Nov. 2019, doi: 10.1002/advs.201901371.
- [35] S. Li, D. M. Vogt, D. Rus, and R. J. Wood, “Fluid-driven origami-inspired artificial muscles,” *Proc. Natl. Acad. Sci. U.S.A.*, vol. 114, no. 50, pp. 13132–13137, Dec. 2017, doi: 10.1073/pnas.1713450114.
- [36] M. Wehner *et al.*, “A lightweight soft exosuit for gait assistance,” in *2013 IEEE International Conference on Robotics and Automation*, Karlsruhe, Germany, May 2013, pp. 3362–3369. doi: 10.1109/ICRA.2013.6631046.
- [37] M. Wehner *et al.*, “Experimental characterization of components for active soft orthotics,” in *2012 4th IEEE RAS & EMBS International Conference on Biomedical Robotics and Biomechanics (BioRob)*, Rome, Italy, Jun. 2012, pp. 1586–1592. doi: 10.1109/BioRob.2012.6290903.
- [38] M. Wehner, D. Rempel, and H. Kazerooni, “Lower Extremity Exoskeleton Reduces Back Forces in Lifting,” in *ASME 2009 Dynamic Systems and Control Conference, Volume 2*, Hollywood, California, USA, Jan. 2009, pp. 49–56. doi: 10.1115/DSCC2009-2644.
- [39] Ching-Ping Chou and B. Hannaford, “Measurement and modeling of McKibben pneumatic artificial muscles,” *IEEE Trans. Robot. Automat.*, vol. 12, no. 1, pp. 90–102, Feb. 1996, doi: 10.1109/70.481753.
- [40] “Modeling and control of McKibben artificial muscle robot actuators,” *IEEE Control Syst.*, vol. 20, no. 2, pp. 15–38, Apr. 2000, doi: 10.1109/37.833638.
- [41] T. Ren, Y. Li, M. Xu, Y. Li, C. Xiong, and Y. Chen, “A Novel Tendon-Driven Soft Actuator with Self-Pumping Property,” *Soft Robotics*, vol. 7, no. 2, pp. 130–139, Apr. 2020, doi: 10.1089/soro.2019.0008.

- [42] I. Hussain *et al.*, “Modeling and Prototyping of an Underactuated Gripper Exploiting Joint Compliance and Modularity,” *IEEE Robot. Autom. Lett.*, vol. 3, no. 4, pp. 2854–2861, Oct. 2018, doi: 10.1109/LRA.2018.2845906.
- [43] A. K. Mishra, E. Del Dottore, A. Sadeghi, A. Mondini, and B. Mazzolai, “SIMBA: Tendon-Driven Modular Continuum Arm with Soft Reconfigurable Gripper,” *Front. Robot. AI*, vol. 4, Feb. 2017, doi: 10.3389/frobt.2017.00004.
- [44] F. Chen *et al.*, “Topology Optimized Design, Fabrication, and Characterization of a Soft Cable-Driven Gripper,” *IEEE Robot. Autom. Lett.*, vol. 3, no. 3, pp. 2463–2470, Jul. 2018, doi: 10.1109/LRA.2018.2800115.
- [45] E. Deng and Y. Tadesse, “A Soft 3D-Printed Robotic Hand Actuated by Coiled SMA,” *Actuators*, vol. 10, no. 1, p. 6, Dec. 2020, doi: 10.3390/act10010006.
- [46] H. Rodrigue, W. Wei, B. Bhandari, and S.-H. Ahn, “Fabrication of wrist-like SMA-based actuator by double smart soft composite casting,” *Smart Mater. Struct.*, vol. 24, no. 12, p. 125003, Dec. 2015, doi: 10.1088/0964-1726/24/12/125003.
- [47] J.-H. Lee, Y. S. Chung, and H. Rodrigue, “Long Shape Memory Alloy Tendon-based Soft Robotic Actuators and Implementation as a Soft Gripper,” *Sci Rep*, vol. 9, no. 1, p. 11251, Dec. 2019, doi: 10.1038/s41598-019-47794-1.
- [48] W. Wang and S.-H. Ahn, “Shape Memory Alloy-Based Soft Gripper with Variable Stiffness for Compliant and Effective Grasping,” *Soft Robotics*, vol. 4, no. 4, pp. 379–389, Dec. 2017, doi: 10.1089/soro.2016.0081.
- [49] H.-I. Kim, M.-W. Han, S.-H. Song, and S.-H. Ahn, “Soft morphing hand driven by SMA tendon wire,” *Composites Part B: Engineering*, vol. 105, pp. 138–148, Nov. 2016, doi: 10.1016/j.compositesb.2016.09.004.
- [50] R. Mutlu, G. Alici, and Weihua Li, “Electroactive polymers as soft robotic actuators: Electromechanical modeling and identification,” in *2013 IEEE/ASME International Conference on Advanced Intelligent Mechatronics*, Wollongong, NSW, Jul. 2013, pp. 1096–1101. doi: 10.1109/AIM.2013.6584240.
- [51] J. Shintake, S. Rosset, B. Schubert, D. Floreano, and H. Shea, “Versatile Soft Grippers with Intrinsic Electroadhesion Based on Multifunctional Polymer Actuators,” *Adv. Mater.*, vol. 28, no. 2, pp. 231–238, Jan. 2016, doi: 10.1002/adma.201504264.
- [52] R. Pelrine *et al.*, “Dielectric elastomer artificial muscle actuators: toward biomimetic motion,” San Diego, CA, Jul. 2002, pp. 126–137. doi: 10.1117/12.475157.

- [53] R. D. Kornbluh *et al.*, “Electroelastomers: applications of dielectric elastomer transducers for actuation, generation, and smart structures,” San Diego, CA, Jul. 2002, pp. 254–270. doi: 10.1117/12.475072.
- [54] X. Ji *et al.*, “An autonomous untethered fast soft robotic insect driven by low-voltage dielectric elastomer actuators,” *Sci. Robot.*, vol. 4, no. 37, p. eaaz6451, Dec. 2019, doi: 10.1126/scirobotics.aaz6451.
- [55] Y. Chen *et al.*, “Controlled flight of a microrobot powered by soft artificial muscles,” *Nature*, vol. 575, no. 7782, pp. 324–329, Nov. 2019, doi: 10.1038/s41586-019-1737-7.
- [56] I. A. Anderson, T. A. Gisby, T. G. McKay, B. M. O’Brien, and E. P. Calius, “Multi-functional dielectric elastomer artificial muscles for soft and smart machines,” *Journal of Applied Physics*, vol. 112, no. 4, p. 041101, Aug. 2012, doi: 10.1063/1.4740023.
- [57] C. Stergiopoulos *et al.*, “A Soft Combustion-Driven Pump for Soft Robots,” in *Volume 2: Mechanics and Behavior of Active Materials; Integrated System Design and Implementation; Bioinspired Smart Materials and Systems; Energy Harvesting*, Newport, Rhode Island, USA, Sep. 2014, p. V002T04A011. doi: 10.1115/SMASIS2014-7536.
- [58] N. W. Bartlett *et al.*, “A 3D-printed, functionally graded soft robot powered by combustion,” *Science*, vol. 349, no. 6244, pp. 161–165, Jul. 2015, doi: 10.1126/science.aab0129.
- [59] “Tekscan | Pressure Mapping, Force Measurement, & Tactile Sensors,” *Tekscan*. <https://tekscan.com/> (accessed May 05, 2022).
- [60] “Flexpoint Sensor Systems, Inc. | Thin Film Sensing Technology Supplier,” *Flexpoint Sensor Systems, Inc.* <https://flexpoint.com/> (accessed May 05, 2022).
- [61] D. M. Vogt, Y.-L. Park, and R. J. Wood, “Design and Characterization of a Soft Multi-Axis Force Sensor Using Embedded Microfluidic Channels,” *IEEE Sensors J.*, vol. 13, no. 10, pp. 4056–4064, Oct. 2013, doi: 10.1109/JSEN.2013.2272320.
- [62] Yong-Lae Park, Bor-Rong Chen, and R. J. Wood, “Design and Fabrication of Soft Artificial Skin Using Embedded Microchannels and Liquid Conductors,” *IEEE Sensors J.*, vol. 12, no. 8, pp. 2711–2718, Aug. 2012, doi: 10.1109/JSEN.2012.2200790.
- [63] J. T. Muth *et al.*, “Embedded 3D Printing of Strain Sensors within Highly Stretchable Elastomers,” *Adv. Mater.*, vol. 26, no. 36, pp. 6307–6312, Sep. 2014, doi: 10.1002/adma.201400334.

- [64] Y.-L. Park, B. Chen, and R. J. Wood, “Soft artificial skin with multi-modal sensing capability using embedded liquid conductors,” in *2011 IEEE SENSORS Proceedings*, Limerick, Oct. 2011, pp. 81–84. doi: 10.1109/ICSENS.2011.6127228.
- [65] Y. Menguc *et al.*, “Soft wearable motion sensing suit for lower limb biomechanics measurements,” in *2013 IEEE International Conference on Robotics and Automation*, Karlsruhe, Germany, May 2013, pp. 5309–5316. doi: 10.1109/ICRA.2013.6631337.
- [66] A. Tairysh and I. A. Anderson, “Capacitive Stretch Sensing for Robotic Skins,” *Soft Robotics*, vol. 6, no. 3, pp. 389–398, Jun. 2019, doi: 10.1089/soro.2018.0055.
- [67] W. Felt, K. Y. Chin, and C. D. Remy, “Contraction Sensing With Smart Braid McKibben Muscles,” *IEEE/ASME Trans. Mechatron.*, vol. 21, no. 3, pp. 1201–1209, Jun. 2016, doi: 10.1109/TMECH.2015.2493782.
- [68] T. Kim, S. Lee, T. Hong, G. Shin, T. Kim, and Y.-L. Park, “Heterogeneous sensing in a multifunctional soft sensor for human-robot interfaces,” *Sci. Robot.*, vol. 5, no. 49, p. eabc6878, Dec. 2020, doi: 10.1126/scirobotics.abc6878.
- [69] P. A. Xu, A. K. Mishra, H. Bai, C. A. Aubin, L. Zullo, and R. F. Shepherd, “Optical lace for synthetic afferent neural networks,” *Sci. Robot.*, vol. 4, no. 34, p. eaaw6304, Sep. 2019, doi: 10.1126/scirobotics.aaw6304.
- [70] H. Zhao, K. O’Brien, S. Li, and R. F. Shepherd, “Optoelectronically innervated soft prosthetic hand via stretchable optical waveguides,” *Sci. Robot.*, vol. 1, no. 1, p. eaai7529, Dec. 2016, doi: 10.1126/scirobotics.aai7529.
- [71] H. Bai, S. Li, J. Barreiros, Y. Tu, C. R. Pollock, and R. F. Shepherd, “Stretchable distributed fiber-optic sensors,” *Science*, vol. 370, no. 6518, pp. 848–852, Nov. 2020, doi: 10.1126/science.aba5504.
- [72] Y. Zhang *et al.*, “Fast-Response, Stiffness-Tunable Soft Actuator by Hybrid Multimaterial 3D Printing,” *Adv. Funct. Mater.*, vol. 29, no. 15, p. 1806698, Apr. 2019, doi: 10.1002/adfm.201806698.
- [73] B. Yuan, C. Zhao, X. Sun, and J. Liu, “Liquid-Metal-Enhanced Wire Mesh as a Stiffness Variable Material for Making Soft Robotics,” *Adv. Eng. Mater.*, vol. 21, no. 10, p. 1900530, Oct. 2019, doi: 10.1002/adem.201900530.
- [74] Y. S. Narang, J. J. Vlassak, and R. D. Howe, “Mechanically Versatile Soft Machines through Laminar Jamming,” *Adv. Funct. Mater.*, vol. 28, no. 17, p. 1707136, Apr. 2018, doi: 10.1002/adfm.201707136.

- [75] M. Brancadoro, M. Manti, S. Tognarelli, and M. Cianchetti, “Preliminary experimental study on variable stiffness structures based on fiber jamming for soft robots,” in *2018 IEEE International Conference on Soft Robotics (RoboSoft)*, Livorno, Apr. 2018, pp. 258–263. doi: 10.1109/ROBOSOFT.2018.8404929.
- [76] E. Brown *et al.*, “Universal robotic gripper based on the jamming of granular material,” *Proc. Natl. Acad. Sci. U.S.A.*, vol. 107, no. 44, pp. 18809–18814, Nov. 2010, doi: 10.1073/pnas.1003250107.
- [77] Y. Wei *et al.*, “A Novel, Variable Stiffness Robotic Gripper Based on Integrated Soft Actuating and Particle Jamming,” *Soft Robotics*, vol. 3, no. 3, pp. 134–143, Sep. 2016, doi: 10.1089/soro.2016.0027.
- [78] J. R. Amend, E. Brown, N. Rodenberg, H. M. Jaeger, and H. Lipson, “A Positive Pressure Universal Gripper Based on the Jamming of Granular Material,” *IEEE Trans. Robot.*, vol. 28, no. 2, pp. 341–350, Apr. 2012, doi: 10.1109/TRO.2011.2171093.
- [79] M. Brancadoro, M. Manti, F. Grani, S. Tognarelli, A. Menciassi, and M. Cianchetti, “Toward a Variable Stiffness Surgical Manipulator Based on Fiber Jamming Transition,” *Front. Robot. AI*, vol. 6, p. 12, Mar. 2019, doi: 10.3389/frobt.2019.00012.
- [80] B. Aktas and R. D. Howe, “Tunable Anisotropic Stiffness with Square Fiber Jamming,” in *2020 3rd IEEE International Conference on Soft Robotics (RoboSoft)*, New Haven, CT, USA, May 2020, pp. 879–884. doi: 10.1109/RoboSoft48309.2020.9116030.
- [81] S. Jadhav, M. R. A. Majit, B. Shih, J. P. Schulze, and M. T. Tolley, “Variable Stiffness Devices Using Fiber Jamming for Application in Soft Robotics and Wearable Haptics,” *Soft Robotics*, vol. 9, no. 1, pp. 173–186, Feb. 2022, doi: 10.1089/soro.2019.0203.
- [82] I. Choi, N. Corson, L. Peiros, E. W. Hawkes, S. Keller, and S. Follmer, “A Soft, Controllable, High Force Density Linear Brake Utilizing Layer Jamming,” *IEEE Robot. Autom. Lett.*, vol. 3, no. 1, pp. 450–457, Jan. 2018, doi: 10.1109/LRA.2017.2761938.
- [83] Y. Yang, Y. Zhang, Z. Kan, J. Zeng, and M. Y. Wang, “Hybrid Jamming for Bioinspired Soft Robotic Fingers,” *Soft Robotics*, vol. 7, no. 3, pp. 292–308, Jun. 2020, doi: 10.1089/soro.2019.0093.
- [84] L. Gerez, G. Gao, and M. Liarokapis, “Laminar Jamming Flexure Joints for the Development of Variable Stiffness Robot Grippers and Hands,” in *2020 IEEE/RSJ International Conference on Intelligent Robots and Systems (IROS)*,

Las Vegas, NV, USA, Oct. 2020, pp. 8709–8715. doi: 10.1109/IROS45743.2020.9340752.

- [85] W. H. Choi, S. Kim, D. Lee, and D. Shin, “Soft, Multi-DoF, Variable Stiffness Mechanism Using Layer Jamming for Wearable Robots,” *IEEE Robot. Autom. Lett.*, vol. 4, no. 3, pp. 2539–2546, Jul. 2019, doi: 10.1109/LRA.2019.2908493.
- [86] K.-Y. Lin and S. K. Gupta, “Soft Fingers with Controllable Compliance to Enable Realization of Low Cost Grippers,” in *Biomimetic and Biohybrid Systems*, vol. 10384, M. Mangan, M. Cutkosky, A. Mura, P. F. M. J. Verschure, T. Prescott, and N. Lepora, Eds. Cham: Springer International Publishing, 2017, pp. 544–550. doi: 10.1007/978-3-319-63537-8_48.
- [87] K. M. Lynch and F. C. Park, *Modern robotics: mechanics, planning, and control*. Cambridge, UK: Cambridge University Press, 2017.
- [88] R. M. Murray, Z. Li, and S. S. Sastry, *A Mathematical Introduction to Robotic Manipulation*, 1st ed. CRC Press, 2017. doi: 10.1201/9781315136370.
- [89] B. S. Homberg, R. K. Katzschmann, M. R. Dogar, and D. Rus, “Robust proprioceptive grasping with a soft robot hand,” *Auton Robot*, vol. 43, no. 3, pp. 681–696, Mar. 2019, doi: 10.1007/s10514-018-9754-1.
- [90] Q. Wu *et al.*, “A novel underwater bipedal walking soft robot bio-inspired by the coconut octopus,” *Bioinspir. Biomim.*, vol. 16, no. 4, p. 046007, Jul. 2021, doi: 10.1088/1748-3190/abf6b9.
- [91] P. Roberts, D. D. Damian, W. Shan, T. Lu, and C. Majidi, “Soft-matter capacitive sensor for measuring shear and pressure deformation,” in *2013 IEEE International Conference on Robotics and Automation*, Karlsruhe, Germany, May 2013, pp. 3529–3534. doi: 10.1109/ICRA.2013.6631071.
- [92] G.-S. Cho and Y.-J. Park, “Soft Gripper with EGaIn Soft Sensor for Detecting Grasp Status,” *Applied Sciences*, vol. 11, no. 15, p. 6957, Jul. 2021, doi: 10.3390/app11156957.
- [93] F. L. Hammond, Y. Menguc, and R. J. Wood, “Toward a modular soft sensor-embedded glove for human hand motion and tactile pressure measurement,” in *2014 IEEE/RSJ International Conference on Intelligent Robots and Systems*, Chicago, IL, USA, Sep. 2014, pp. 4000–4007. doi: 10.1109/IROS.2014.6943125.
- [94] J.-B. Chossat, Y.-L. Park, R. J. Wood, and V. Duchaine, “A Soft Strain Sensor Based on Ionic and Metal Liquids,” *IEEE Sensors J.*, vol. 13, no. 9, pp. 3405–3414, Sep. 2013, doi: 10.1109/JSEN.2013.2263797.

- [95] U. Daalkhaijav, O. D. Yirmibesoglu, S. Walker, and Y. Mengüç, “Rheological Modification of Liquid Metal for Additive Manufacturing of Stretchable Electronics,” *Adv. Mater. Technol.*, vol. 3, no. 4, p. 1700351, Apr. 2018, doi: 10.1002/admt.201700351.
- [96] Vogt, D., Yigit Menguc, Yong-Lae Park, Michael Wehner, R. K. Kramer, Carmel Majidi, L. P. Jentoft, Yaroslav Tenzer, R. D. Howe, and Robert J. Wood. "Progress in soft, flexible, and stretchable sensing systems." In Proceedings of the International Workshop on Research Frontiers in Electronics Skin Technology at ICRA, vol. 13. 2013.
- [97] R. L. Truby, “Designing Soft Robots as Robotic Materials,” *Acc. Mater. Res.*, vol. 2, no. 10, pp. 854–857, Oct. 2021, doi: 10.1021/accountsmr.1c00071.
- [98] G. Gerboni, A. Diodato, G. Ciuti, M. Cianchetti, and A. Menciassi, “Feedback Control of Soft Robot Actuators via Commercial Flex Bend Sensors,” *IEEE/ASME Trans. Mechatron.*, vol. 22, no. 4, pp. 1881–1888, Aug. 2017, doi: 10.1109/TMECH.2017.2699677.
- [99] M. D. Mitchell, F. E. Hurley, and C. D. Onal, “Fast Probabilistic 3-D Curvature Proprioception with a Magnetic Soft Sensor,” in *2021 IEEE 17th International Conference on Automation Science and Engineering (CASE)*, Lyon, France, Aug. 2021, pp. 215–220. doi: 10.1109/CASE49439.2021.9551572.
- [100] B. W. McInroe, C. L. Chen, K. Y. Goldberg, K. Y. Goldberg, R. Bajcsy, and R. S. Fearing, “Towards a Soft Fingertip with Integrated Sensing and Actuation,” in *2018 IEEE/RSJ International Conference on Intelligent Robots and Systems (IROS)*, Madrid, Oct. 2018, pp. 6437–6444. doi: 10.1109/IROS.2018.8594032.
- [101] J. Tapia, E. Knoop, M. Mutný, M. A. Otaduy, and M. Bächer, “MakeSense: Automated Sensor Design for Proprioceptive Soft Robots,” *Soft Robotics*, vol. 7, no. 3, pp. 332–345, Jun. 2020, doi: 10.1089/soro.2018.0162.
- [102] T. F. Otero, “Towards artificial proprioception from artificial muscles constituted by self-sensing multi-step electrochemical macromolecular motors,” *Electrochimica Acta*, vol. 368, p. 137576, Feb. 2021, doi: 10.1016/j.electacta.2020.137576.
- [103] B. Shih *et al.*, “Electronic skins and machine learning for intelligent soft robots,” *Sci. Robot.*, vol. 5, no. 41, p. eaaz9239, Apr. 2020, doi: 10.1126/scirobotics.aaz9239.
- [104] P. Holmes, R. J. Full, D. Koditschek, and J. Guckenheimer, “The Dynamics of Legged Locomotion: Models, Analyses, and Challenges,” *SIAM Rev.*, vol. 48, no. 2, pp. 207–304, Jan. 2006, doi: 10.1137/S0036144504445133.

- [105] R. S. Dahiya, P. Mittendorfer, M. Valle, G. Cheng, and V. J. Lumelsky, "Directions Toward Effective Utilization of Tactile Skin: A Review," *IEEE Sensors J.*, vol. 13, no. 11, pp. 4121–4138, Nov. 2013, doi: 10.1109/JSEN.2013.2279056.
- [106] E. Florey, "Ultrastructure and Function of Cephalopod Chromatophores," *Am Zool*, vol. 9, no. 2, pp. 429–442, May 1969, doi: 10.1093/icb/9.2.429.
- [107] R. A. Cloney and S. L. Brocco, "Chromatophore Organs, Reflector Cells, Iridocytes and Leucophores in Cephalopods," *Am Zool*, vol. 23, no. 3, pp. 581–592, Aug. 1983, doi: 10.1093/icb/23.3.581.
- [108] T. L. Williams *et al.*, "Dynamic pigmentary and structural coloration within cephalopod chromatophore organs," *Nat Commun*, vol. 10, no. 1, p. 1004, Dec. 2019, doi: 10.1038/s41467-019-08891-x.
- [109] G. Giordano, M. Carlotti, and B. Mazzolai, "A Perspective on Cephalopods Mimicry and Bioinspired Technologies toward Proprioceptive Autonomous Soft Robots," *Adv Materials Technologies*, vol. 6, no. 12, p. 2100437, Dec. 2021, doi: 10.1002/admt.202100437.
- [110] S. Zeng *et al.*, "Bio-inspired sensitive and reversible mechanochromisms via strain-dependent cracks and folds," *Nat Commun*, vol. 7, no. 1, p. 11802, Sep. 2016, doi: 10.1038/ncomms11802.
- [111] J. Rossiter, B. Yap, and A. Conn, "Biomimetic chromatophores for camouflage and soft active surfaces," *Bioinspir. Biomim.*, vol. 7, no. 3, p. 036009, Sep. 2012, doi: 10.1088/1748-3182/7/3/036009.
- [112] F. P. Beer, Ed., *Mechanics of materials*, 6th ed. New York: McGraw-Hill, 2011.
- [113] S. Timoshenko, *History of strength of materials: with a brief account of the history of theory of elasticity and theory of structures*. New York: Dover Publications, 1983.
- [114] R. J. Roark, W. C. Young, R. G. Budynas, and A. M. Sadegh, *Roark's formulas for stress and strain*. 2012. Accessed: Feb. 23, 2022. [Online]. Available: <http://accessengineeringlibrary.com/browse/roarks-formulas-for-stress-and-strain-eighth-edition>
- [115] A. P. Boresi and R. J. Schmidt, *Advanced mechanics of materials*, 6th ed. New York: John Wiley & Sons, 2003.

- [116] M. S. Aziz and A. Y. El sherif, “Biomimicry as an approach for bio-inspired structure with the aid of computation,” *Alexandria Engineering Journal*, vol. 55, no. 1, pp. 707–714, Mar. 2016, doi: 10.1016/j.aej.2015.10.015.
- [117] G. Soter, M. Garrad, A. T. Conn, H. Hauser, and J. Rossiter, “Skinflow: A soft robotic skin based on fluidic transmission,” in *2019 2nd IEEE International Conference on Soft Robotics (RoboSoft)*, Seoul, Korea (South), Apr. 2019, pp. 355–360. doi: 10.1109/ROBOSOFT.2019.8722744.
- [118] A. Moniz and B.-J. Krings, “Robots Working with Humans or Humans Working with Robots? Searching for Social Dimensions in New Human-Robot Interaction in Industry,” *Societies*, vol. 6, no. 3, p. 23, Aug. 2016, doi: 10.3390/soc6030023.
- [119] T. B. Sheridan, “Human–Robot Interaction: Status and Challenges,” *Hum Factors*, vol. 58, no. 4, pp. 525–532, Jun. 2016, doi: 10.1177/0018720816644364.
- [120] J. Wang, D. Gao, and P. S. Lee, “Recent Progress in Artificial Muscles for Interactive Soft Robotics,” *Adv. Mater.*, vol. 33, no. 19, p. 2003088, May 2021, doi: 10.1002/adma.202003088.
- [121] Y. She, C. Li, J. Cleary, and H.-J. Su, “Design and Fabrication of a Soft Robotic Hand With Embedded Actuators and Sensors,” *Journal of Mechanisms and Robotics*, vol. 7, no. 2, p. 021007, May 2015, doi: 10.1115/1.4029497.
- [122] J. Jeong, I. B. Yasir, J. Han, C. H. Park, S.-K. Bok, and K.-U. Kyung, “Design of Shape Memory Alloy-Based Soft Wearable Robot for Assisting Wrist Motion,” *Applied Sciences*, vol. 9, no. 19, p. 4025, Sep. 2019, doi: 10.3390/app9194025.
- [123] D. I. Labs, “Soft Robotics - Food Automation Solutions For Single and Bulk Picking,” *Soft Robotics*. <https://www.softroboticsinc.com/> (accessed Mar. 18, 2022).
- [124] J. Wang and A. Chortos, “Control Strategies for Soft Robot Systems,” *Advanced Intelligent Systems*, vol. 4, no. 5, p. 2100165, May 2022, doi: 10.1002/aisy.202100165.
- [125] R. K. Katschmann *et al.*, “Dynamically Closed-Loop Controlled Soft Robotic Arm using a Reduced Order Finite Element Model with State Observer,” in *2019 2nd IEEE International Conference on Soft Robotics (RoboSoft)*, Seoul, Korea (South), Apr. 2019, pp. 717–724. doi: 10.1109/ROBOSOFT.2019.8722804.
- [126] Z. Shahid, A. L. Glatman, and S. C. Ryu, “Design of a Soft Composite Finger with Adjustable Joint Stiffness,” *Soft Robotics*, vol. 6, no. 6, pp. 722–732, Dec. 2019, doi: 10.1089/soro.2018.0148.

- [127] W. Wang, C. Y. Yu, P. A. Abrego Serrano, and S.-H. Ahn, “Shape Memory Alloy-Based Soft Finger with Changeable Bending Length Using Targeted Variable Stiffness,” *Soft Robotics*, vol. 7, no. 3, pp. 283–291, Jun. 2020, doi: 10.1089/soro.2018.0166.
- [128] W. Park, S. Seo, and J. Bae, “A Hybrid Gripper With Soft Material and Rigid Structures,” *IEEE Robot. Autom. Lett.*, vol. 4, no. 1, pp. 65–72, Jan. 2019, doi: 10.1109/LRA.2018.2878972.
- [129] H. Yufei *et al.*, “A variable stiffness soft robotic gripper with low-melting-point alloy,” in *2017 36th Chinese Control Conference (CCC)*, Dalian, China, Jul. 2017, pp. 6781–6786. doi: 10.23919/ChiCC.2017.8028427.
- [130] T. Sun, Y. Chen, T. Han, C. Jiao, B. Lian, and Y. Song, “A soft gripper with variable stiffness inspired by pangolin scales, toothed pneumatic actuator and autonomous controller,” *Robotics and Computer-Integrated Manufacturing*, vol. 61, p. 101848, Feb. 2020, doi: 10.1016/j.rcim.2019.101848.
- [131] F. Connolly, C. J. Walsh, and K. Bertoldi, “Automatic design of fiber-reinforced soft actuators for trajectory matching,” *Proc. Natl. Acad. Sci. U.S.A.*, vol. 114, no. 1, pp. 51–56, Jan. 2017, doi: 10.1073/pnas.1615140114.
- [132] B. Gorissen, D. Reynaerts, S. Konishi, K. Yoshida, J.-W. Kim, and M. De Volder, “Elastic Inflatable Actuators for Soft Robotic Applications,” *Adv. Mater.*, vol. 29, no. 43, p. 1604977, Nov. 2017, doi: 10.1002/adma.201604977.
- [133] M. S. Xavier, A. J. Fleming, and Y. K. Yong, “Finite Element Modeling of Soft Fluidic Actuators: Overview and Recent Developments,” *Advanced Intelligent Systems*, vol. 3, no. 2, p. 2000187, Feb. 2021, doi: 10.1002/aisy.202000187.
- [134] N. El-Atab *et al.*, “Soft Actuators for Soft Robotic Applications: A Review,” *Advanced Intelligent Systems*, vol. 2, no. 10, p. 2000128, Oct. 2020, doi: 10.1002/aisy.202000128.
- [135] M. W. Spong and M. Vidyasagar, *Robot dynamics and control*. New York: Wiley, 1989.
- [136] B. Mosadegh *et al.*, “Pneumatic Networks for Soft Robotics that Actuate Rapidly,” *Adv. Funct. Mater.*, vol. 24, no. 15, pp. 2163–2170, Apr. 2014, doi: 10.1002/adfm.201303288.
- [137] C. W. Hull, “Apparatus for production of three-dimensional objects by stereolithography,” US4575330A, Mar. 11, 1986 Accessed: Feb. 28, 2022. [Online]. Available: <https://patents.google.com/patent/US4575330A/en>

- [138] “formlabs-materials-library.pdf.” Accessed: Feb. 28, 2022. [Online]. Available: https://formlabs-media.formlabs.com/filer_public/ac/89/ac8963db-f54a-4cac-8fe9-fb740a7b06f1/formlabs-materials-library.pdf
- [139] J. R. C. Dizon, A. H. Espera, Q. Chen, and R. C. Advincula, “Mechanical characterization of 3D-printed polymers,” *Additive Manufacturing*, vol. 20, pp. 44–67, Mar. 2018, doi: 10.1016/j.addma.2017.12.002.
- [140] J. Saini, L. Dowling, J. Kennedy, and D. Trimble, “Investigations of the mechanical properties on different print orientations in SLA 3D printed resin,” *Proceedings of the Institution of Mechanical Engineers, Part C: Journal of Mechanical Engineering Science*, vol. 234, no. 11, pp. 2279–2293, Jun. 2020, doi: 10.1177/0954406220904106.
- [141] J. Wu, Z. He, Q. Chen, and J.-M. Lin, “Biochemical analysis on microfluidic chips,” *TrAC Trends in Analytical Chemistry*, vol. 80, pp. 213–231, Jun. 2016, doi: 10.1016/j.trac.2016.03.013.
- [142] D.-E. Li and C.-H. Lin, “Microfluidic chip for droplet-based AuNP synthesis with dielectric barrier discharge plasma and on-chip mercury ion detection,” *RSC Adv.*, vol. 8, no. 29, pp. 16139–16145, 2018, doi: 10.1039/C8RA02468E.
- [143] S. N. Bhatia and D. E. Ingber, “Microfluidic organs-on-chips,” *Nat Biotechnol.*, vol. 32, no. 8, pp. 760–772, Aug. 2014, doi: 10.1038/nbt.2989.
- [144] D. Huh, B. D. Matthews, A. Mammoto, M. Montoya-Zavala, H. Y. Hsin, and D. E. Ingber, “Reconstituting Organ-Level Lung Functions on a Chip,” *Science*, vol. 328, no. 5986, pp. 1662–1668, Jun. 2010, doi: 10.1126/science.1188302.
- [145] J. M. Taylor, K. Perez-Toralla, R. Aispuro, and S. A. Morin, “Covalent Bonding of Thermoplastics to Rubbers for Printable, Reel-to-Reel Processing in Soft Robotics and Microfluidics,” *Adv. Mater.*, vol. 30, no. 7, p. 1705333, Feb. 2018, doi: 10.1002/adma.201705333.
- [146] A. Konda, D. Lee, T. You, X. Wang, S. Ryu, and S. A. Morin, “Reversible Mechanical Deformations of Soft Microchannel Networks for Sensing in Soft Robotic Systems,” *Advanced Intelligent Systems*, vol. 1, no. 4, p. 1900027, Aug. 2019, doi: 10.1002/aisy.201900027.
- [147] M. Garrad, G. Soter, A. T. Conn, H. Hauser, and J. Rossiter, “A soft matter computer for soft robots,” *Sci. Robot.*, vol. 4, no. 33, p. eaaw6060, Aug. 2019, doi: 10.1126/scirobotics.aaw6060.
- [148] A. Manz, N. Graber, and H. M. Widmer, “Miniaturized total chemical analysis systems: A novel concept for chemical sensing,” *Sensors and Actuators B:*

Chemical, vol. 1, no. 1–6, pp. 244–248, Jan. 1990, doi: 10.1016/0925-4005(90)80209-I.

- [149] J. B. Angell, S. C. Terry, and P. W. Barth, “Silicon Micromechanical Devices,” *Sci Am*, vol. 248, no. 4, pp. 44–55, Apr. 1983, doi: 10.1038/scientificamerican0483-44.
- [150] S. C. Terry, J. H. Jerman, and J. B. Angell, “A gas chromatographic air analyzer fabricated on a silicon wafer,” *IEEE Trans. Electron Devices*, vol. 26, no. 12, pp. 1880–1886, Dec. 1979, doi: 10.1109/T-ED.1979.19791.
- [151] M. Rhee and M. A. Burns, “Microfluidic pneumatic logic circuits and digital pneumatic microprocessors for integrated microfluidic systems,” *Lab Chip*, vol. 9, no. 21, p. 3131, 2009, doi: 10.1039/b904354c.
- [152] J. Y. Baek, J. Y. Park, J. I. Ju, T. S. Lee, and S. H. Lee, “A pneumatically controllable flexible and polymeric microfluidic valve fabricated via *in situ* development,” *J. Micromech. Microeng.*, vol. 15, no. 5, pp. 1015–1020, May 2005, doi: 10.1088/0960-1317/15/5/017.
- [153] J. Xie, J. Shih, Q. Lin, B. Yang, and Y.-C. Tai, “Surface micromachined electrostatically actuated micro peristaltic pump,” *Lab Chip*, vol. 4, no. 5, p. 495, 2004, doi: 10.1039/b403906h.
- [154] T.-Q. Truong and N.-T. Nguyen, “A polymeric piezoelectric micropump based on lamination technology,” *J. Micromech. Microeng.*, vol. 14, no. 4, pp. 632–638, Apr. 2004, doi: 10.1088/0960-1317/14/4/026.
- [155] M. Khoo and C. Liu, “A novel micromachined magnetic membrane microfluid pump,” in *Proceedings of the 22nd Annual International Conference of the IEEE Engineering in Medicine and Biology Society (Cat. No.00CH37143)*, Chicago, IL, USA, 2000, vol. 3, pp. 2394–2397. doi: 10.1109/IEMBS.2000.900628.
- [156] E. Makino, T. Mitsuya, and T. Shibata, “Fabrication of TiNi shape memory micropump,” *Sensors and Actuators A: Physical*, vol. 88, no. 3, pp. 256–262, Jan. 2001, doi: 10.1016/S0924-4247(00)00522-7.
- [157] S.-M. Ha, W. Cho, and Y. Ahn, “Disposable thermo-pneumatic micropump for bio lab-on-a-chip application,” *Microelectronic Engineering*, vol. 86, no. 4–6, pp. 1337–1339, Apr. 2009, doi: 10.1016/j.mee.2008.12.046.
- [158] Q. Gong, Z. Zhou, Y. Yang, and X. Wang, “Design, optimization and simulation on microelectromagnetic pump,” *Sensors and Actuators A: Physical*, vol. 83, no. 1–3, pp. 200–207, May 2000, doi: 10.1016/S0924-4247(99)00384-2.

- [159] M. Koch, A. G. R. Evans, and A. Brunnschweiler, “Simulation and fabrication of micromachined cantilever valves,” *Sensors and Actuators A: Physical*, vol. 62, no. 1–3, pp. 756–759, Jul. 1997, doi: 10.1016/S0924-4247(97)01577-X.
- [160] B. Mosadegh *et al.*, “Integrated elastomeric components for autonomous regulation of sequential and oscillatory flow switching in microfluidic devices,” *Nature Phys*, vol. 6, no. 6, pp. 433–437, Jun. 2010, doi: 10.1038/nphys1637.
- [161] S.-J. Kim, R. Yokokawa, and S. Takayama, “Analyzing threshold pressure limitations in microfluidic transistors for self-regulated microfluidic circuits,” *Appl. Phys. Lett.*, vol. 101, no. 23, p. 234107, Dec. 2012, doi: 10.1063/1.4769985.
- [162] J. Shin, H. Park, V. B. Dang, C.-W. Kim, and S.-J. Kim, “Elastomeric microfluidic valve with low, constant opening threshold pressure,” *RSC Adv.*, vol. 5, no. 30, pp. 23239–23245, 2015, doi: 10.1039/C4RA16696E.
- [163] W. H. Grover, R. H. C. Ivester, E. C. Jensen, and R. A. Mathies, “Development and multiplexed control of latching pneumatic valves using microfluidic logical structures,” *Lab Chip*, vol. 6, no. 5, p. 623, 2006, doi: 10.1039/b518362f.
- [164] N. El-Atab, J. C. Canas, and M. M. Hussain, “Pressure-Driven Two-Input 3D Microfluidic Logic Gates,” *Adv. Sci.*, vol. 7, no. 2, p. 1903027, Jan. 2020, doi: 10.1002/advs.201903027.
- [165] M. Wehner *et al.*, “Pneumatic Energy Sources for Autonomous and Wearable Soft Robotics,” *Soft Robotics*, vol. 1, no. 4, pp. 263–274, Dec. 2014, doi: 10.1089/soro.2014.0018.
- [166] M. Loepfe, C. M. Schumacher, and W. J. Stark, “Design, Performance and Reinforcement of Bearing-Free Soft Silicone Combustion-Driven Pumps,” *Ind. Eng. Chem. Res.*, vol. 53, no. 31, pp. 12519–12526, Aug. 2014, doi: 10.1021/ie501991d.
- [167] Y. Yang, B. Hou, J. Chen, H. Wang, P. Jiao, and Z. He, “High-speed soft actuators based on combustion-enabled transient driving method (TDM),” *Extreme Mechanics Letters*, vol. 37, p. 100731, May 2020, doi: 10.1016/j.eml.2020.100731.
- [168] Shepherd, R. F., Stokes, A. A., Freake, J., Barber, J., Snyder, P. W., Mazzeo, A. D., & Whitesides, G. M. (2013). Using explosions to power a soft robot. *Angewandte Chemie International Edition*, 52(10), 2892-2896.
- [169] “Introduction to In-Cylinder Pressure Diagnostics.” <https://autoditex.com/page/cylinder-pressure-sensor-64-1.html> (accessed Apr. 29, 2022).

- [170] “Visual Demonstration Operation Fourspeed Internal Combustion Stock Vector (Royalty Free) 1675903867,” *Shutterstock*. <https://www.shutterstock.com/image-vector/visual-demonstration-operation-fourspeed-internal-combustion-1675903867> (accessed Apr. 29, 2022).
- [171] D. B. Weibel, W. R. DiLuzio, and G. M. Whitesides, “Microfabrication meets microbiology,” *Nat Rev Microbiol*, vol. 5, no. 3, pp. 209–218, Mar. 2007, doi: 10.1038/nrmicro1616.
- [172] “SU-8-3000-Data-Sheet.pdf.” Accessed: Apr. 28, 2022. [Online]. Available: <https://kayakuam.com/wp-content/uploads/2019/09/SU-8-3000-Data-Sheet.pdf>
- [173] M. A. Eddings, M. A. Johnson, and B. K. Gale, “Determining the optimal PDMS–PDMS bonding technique for microfluidic devices,” *J. Micromech. Microeng.*, vol. 18, no. 6, p. 067001, Jun. 2008, doi: 10.1088/0960-1317/18/6/067001.
- [174] “OpenCV: Canny Edge Detection.” https://docs.opencv.org/3.4/da/d22/tutorial_py_canny.html (accessed Feb. 23, 2022).
- [175] S. Lee, “Lines Detection with Hough Transform,” *Medium*, Jan. 30, 2022. <https://towardsdatascience.com/lines-detection-with-hough-transform-84020b3b1549> (accessed Feb. 23, 2022).